

# Atmospheric Modeling for Modern Wind Energy and Fire Applications

by

**Stephanie Redfern**

B.S., University of Texas at Austin, 2009

M.A., University of Texas at Austin, 2014

M.S., Stanford University, 2015

M.S., University of Colorado Boulder 2018

A thesis submitted to the  
Faculty of the Graduate School of the  
University of Colorado in partial fulfillment  
of the requirements for the degree of  
Doctor of Philosophy

Department of Atmospheric and Oceanic Sciences

2021

## ***Committee Members:***

*Prof. Julie K. Lundquist*

*Dr. Joseph B. Olson*

*Dr. Mark Handschy*

*Dr. Branko Kosović*

*Prof. Katja Freidrich*

Redfern, Stephanie (Ph.D., Atmospheric Science)

Atmospheric Modeling for Modern Wind Energy and Fire Applications

Thesis directed by Prof. Julie K. Lundquist

### **Abstract**

Climate change is rapidly becoming an increasingly dangerous threat. As average global temperatures have risen, extreme weather events have increased in frequency and expanded in intensity. More violent forest fires and more powerful storms have begun to take place. In this dissertation, we explore several ways that models can assist with climate change mitigation and adaptation efforts.

First, we explore the prospective benefit of changing the physics of the wind farm parameterization in the Weather Research and Forecasting Model (WRF). As the world shifts to renewable energy sources to try and reduce and offset carbon emissions, it has become all the more important to accurately forecast wind power production, to maintain grid stability and ensure accurate day-ahead scheduling for utilities. We find that using the rotor-equivalent wind speed (REWS) in lieu of the hub height wind speed for making wind power forecasts can be beneficial in some situations.

The next study changes focus from wind energy forecasting to fire modeling. As fires have become more intense in recent years, their potential for upper tropospheric and lower stratospheric (UTLS) smoke injection has increased. More frequent UTLS aerosol anomalies could have widespread climatic impacts that must be understood. Additionally, with the renewed threat of nuclear war, it has become all the more important to best quantify smoke lofting from fires ignited by weapons detonation. Here, we conduct a sensitivity study focused on plume rise response to local atmospheric conditions. We find that relative humidity plays a crucial role in enhancing lofting, while higher wind speeds have the opposite effect by dampening smoke ascent.

The final section focuses on the challenges of accurately forecasting pyrocumulus (pyroCu) and pyrocumulonimbus (pyroCb) in fire models. PyroCb can generate deep convection, thereby injecting fire combustion aerosols into the UTLS. PyroCb can also produce lightning, which can then

spark further ignitions. It is therefore important that these events are correctly represented in models. We compare simulations of a 2014 California fire that use different microphysics schema—one without any aerosol coupling, and two with different coupling mechanisms. We find that including aerosol-cloud interactions changes the nature of cloud and precipitation formation and requires further research for us to develop a better understanding of its implications for fire forecasting.

## Dedication

To the spirited Beth Redfern, and to the brilliant Francis Redfern

We all got to do our part

Lend a hand and open up your heart

It's all up to me and you

- *Earth, Wind, & Fire*

## Contents

### Chapter

<b>1</b>	<b>Introduction</b>	<b>1</b>
1.1	Scope of the Study . . . . .	3
1.1.1	Wind Energy Forecasting . . . . .	4
1.1.2	Fire Applications . . . . .	6
1.2	Arrangement of the thesis . . . . .	7
<b>2</b>	<b>Incorporation of the Rotor-Equivalent Wind Speed into the Weather Research and Forecasting Model's Wind Farm Parameterization</b>	<b>8</b>
2.1	Preface . . . . .	8
2.2	Abstract . . . . .	9
2.3	Introduction . . . . .	9
2.4	Wind Farm Parameterization . . . . .	12
2.4.1	Current Distribution of WFP . . . . .	12
2.4.2	Rotor-Equivalent Wind Speed (REWS) . . . . .	15
2.4.3	REWS, Considering Veer . . . . .	16
2.4.4	Modeling Approach . . . . .	17
2.4.5	Domain Setup . . . . .	17
2.4.6	Dynamics . . . . .	19
2.4.7	Initial Conditions . . . . .	19

2.5	Simulation Overviews . . . . .	21
2.5.1	Neutral Profiles (Cases NF, NR, NV, NB) . . . . .	21
2.5.2	Stable Profiles with Linear Wind Shear (Cases SF, SR, SV, SB) . . . . .	21
2.5.3	Non-linear Wind Shear (Cases MF, MR, MV, MB) . . . . .	22
2.6	Results . . . . .	23
2.6.1	Comparison with F2012 . . . . .	23
2.6.2	New Physics Options in F2012 Setup (Cases NBASE, NF, NR, NV, NB) . . . . .	24
2.6.3	Comparing Stable Cases, Constant Wind Shear with New Physics (Cases SF, SR, SV, SB) . . . . .	25
2.6.4	Comparing Stable Cases, Non-linear Wind Shear with New Physics (Cases MF, MR, MV, MB) . . . . .	26
2.7	Discussion and Conclusions . . . . .	27
2.8	Acknowledgements . . . . .	28
<b>3</b>	<b>Upper Atmosphere Smoke Injection from Large Areal Fires</b>	<b>36</b>
3.1	Preface . . . . .	36
3.2	Abstract . . . . .	37
3.3	Introduction . . . . .	37
3.4	Model Environment . . . . .	40
3.4.1	Model Setup . . . . .	41
3.4.2	Simulations Overview . . . . .	42
3.4.3	Fuel Source . . . . .	43
3.4.4	Model Uncertainty . . . . .	46
3.5	Results . . . . .	46
3.5.1	Oxygen Starvation in the Model . . . . .	47
3.5.2	Smoke Lofting . . . . .	50
3.5.3	Relative Importance of Moisture and Winds . . . . .	57

3.6	Discussion . . . . .	62
3.7	Acknowledgments . . . . .	66
<b>4</b>	<b>The addition of aerosol-atmosphere interactions to address pyrocumulonimbus formation in the Weather Research and Forecasting Model</b>	<b>71</b>
4.1	Preface . . . . .	71
4.2	Abstract . . . . .	72
4.3	Introduction . . . . .	73
4.4	Case Selection and Scope of Study . . . . .	76
4.5	Methods . . . . .	76
4.5.1	Model Setup . . . . .	76
4.5.2	Water-friendly aerosol and combustion coupling . . . . .	80
4.6	Results . . . . .	81
4.6.1	Fire Spread and Heat Flux Differences . . . . .	82
4.6.2	Differences in Cloud Condensation Nuclei . . . . .	87
4.7	Conclusions . . . . .	91
4.8	Acknowledgements . . . . .	93
<b>5</b>	<b>Conclusions</b>	<b>96</b>
5.1	Summary of Findings . . . . .	96
5.1.1	Inclusion of the Rotor-Equivalent Wind Speed in the WRF WFP . . . . .	96
5.1.2	Smoke Lofting Sensitivity to Local Weather Conditions . . . . .	97
5.1.3	PyroCu and PyroCb Development in WRF with and without WFA . . . . .	98
	<b>References</b>	<b>100</b>

<b>Bibliography</b>	<b>100</b>
---------------------	------------

## **Appendix**

<b>A</b>	<b>Supplementary Information for Chapter 2</b>	<b>119</b>
A.1	Neutral Case . . . . .	119
A.2	Stable, Linear Wind Shear Case . . . . .	119
A.3	Stable, Nonlinear Wind Shear Case . . . . .	120



## Tables

### Table

2.1	Overview of idealized simulations. . . . .	29
2.2	Comparison between F2012 and Redfern et al., 2019 . . . . .	31
3.1	WRF Configuration . . . . .	68
3.2	Simulation Overviews. When referenced elsewhere, each label is followed by an underscore and the fire radius. For example, the base case for the 2-km radius fire will be referred to as Base_2. Note: "Moist," as used in describing the simulations, refers specifically to the addition of atmospheric humidity. Once the fire is lit, all simulations see some release of moisture from the fuel source. . . . .	69
3.3	Smoke generation, upper atmosphere and stratospheric smoke lofting, with the 2-km radius ignition area. Negative error values indicate an overestimation of total smoke in the atmosphere, compared with actual smoke generation at the surface, while positive values indicate an underestimation. . . . .	69
3.4	Smoke generation, upper atmosphere and stratospheric smoke lofting, with the 4-km radius ignition area. Negative error values indicate an overestimation of total smoke in the atmosphere, compared with actual smoke generation at the surface, while positive values indicate an underestimation. . . . .	70
4.1	WRF Model Setup . . . . .	94
4.2	Simulation reference names and microphysics used in each. . . . .	95

## Figures

### Figure

1.1	Average global temperatures and atmospheric carbon dioxide concentrations, 1880-2014. Figure from Melillo, Richmond, and Yohe (2014). . . . .	2
1.2	Cumulative global wind installations, 1980-2016. Figure from Veers et al. (2019). . .	5
2.1	Eta levels used for this study, as well as their corresponding heights. . . . .	18
2.2	Power curve for the PSU Generic 1.5MW Wind Turbine (Schmitz 2011). . . . .	20
2.3	Post-spin-up wind direction and wind speeds for the neutral (a - b), stable (c - d), and mix-out (e - f) simulations. . . . .	30
2.4	Horizontal cross-section of simulation domain taken at hub height showing the wake (a) and TKE generation (b). The black dashed outline indicates the wind farm. Vertical cross-section taken through the center of the wind farm, along the wind direction vector, showing the wake (c) and TKE generation (d). The black dashed outline indicates the wind farm, the gray lines show potential temperature, and the thick black dashed line is the top of the boundary layer. . . . .	32
2.5	Fractional power output in each grid cell of the wind farm, defined as the temporal average of power output in the grid cell divided by the maximum power output of any grid cell over the simulation period (a). Percent difference in power output between the NF and NR simulations (b). . . . .	33

2.6	Difference between the waking (a) and TKE generation (b) in the NR and NF simulations. Negative values in (a) indicate a stronger wake, and positive values in (b) indicate greater TKE. . . . .	33
2.7	Waking and acceleration of winds in the MF_60 simulation (a). Differences between the waking in MR_60 (b), MV_60 (c), MB_60 (d) and MF_60. Positive values in (b, c, d) indicate a weakening of the wake. Negative values along the flanks indicate a weakening of the acceleration on either side of the wake. . . . .	34
2.8	Power output for the MF_60 simulation, in kW (a). Percent change in power output between MR_60 (b), MV_60 (c), MB_60 (d) and MF_60. . . . .	35
3.1	Domain-averaged winds in the nest after spin-up for the winds subset (a), moisture subset (c), and stability subset (e). Thermal profiles after spin-up for the winds subset (b), moisture subset (d), and stability subset (f). . . . .	44
3.2	Post-spinup soundings for the four moist cases: M50 (a), MR25 (b), MR50 (c), and MR75 (d). Green indicates the dew point temperature profiles, while red indicates the environmental temperature profiles. . . . .	45
3.3	<b>Top:</b> Average oxygen depletion in the lowest 200 m of the model across burned area, assuming no air replenishment (left axis, solid), and heat release rate ( $\text{kW m}^{-2}$ ), right axis, dotted) for the 2-km ignition radius fires, grouped by simulation subset (a: Winds, b: Moisture, c: ABL Stability). <b>Bottom:</b> Average oxygen depletion in the lowest 200 m of the model across burned area, assuming no air replenishment (left axis, solid), and heat release rate ( $\text{kW m}^{-2}$ ), right axis, dotted) for the 4-km ignition radius fires, grouped by simulation subset (d: Winds, e: Moisture, f: ABL Stability). The heat release rates for each of Penner, Haselman, and Edwards (1986)'s three fire simulations are marked in each plot by horizontal dotted lines ( $\text{HRR} = 2.2 \text{ kW m}^{-2}$ , $14 \text{ kW m}^{-2}$ , $89 \text{ kW m}^{-2}$ ). The 16% depletion threshold is depicted via a thick horizontal line on each plot. . . . .	49

3.4	Left: Planar view of vertical velocities for Base_2 at Right: Average oxygen depletion per grid cell across burned area (solid), assuming no air replenishment, and heat release rate ( $\text{W m}^{-2}$ , right axis, dotted) for the 4-km ignition radius fires, grouped by simulation subset (Top: Winds, Middle: Moisture, Bottom: ABL Stability). . . .	49
3.5	Final profiles of vertical smoke distribution (in $\text{Mg km}^{-1}$ ) for the wind simulations after 1.5 hours of burning. Linear plots (a,c) and logarithmic plots (b,d), for the 2km radius (a,b) and 4km radius (c,d) ignitions are shown. . . . .	51
3.6	Cross-sectional winds taken from a W-E transect through the domain center, with integrated smoke (colored contours), for HiWi_2 (a) and CalmWi_2 (b). Stronger horizontal winds in HiWi_2 dampen the convective lofting of smoke. . . . .	52
3.7	Final profiles of vertical smoke distribution (in $\text{Mg km}^{-1}$ ) for the moist simulations after 1.5 hours of burning. Linear plots (a,c) and logarithmic plots (b,d), for the 2km radius (a,b) and 4km radius (c,d) ignitions are shown. . . . .	55
3.8	Time series of total smoke above 9 km (solid) and precipitation in the domain (dashed) for M50_2 and MR50_2 (a), Base_2 and MR25_2 (b), M50_4 and MR50_4 (c), and Base_4 and MR25_4 (d). . . . .	56
3.9	Final profiles of vertical smoke distribution (in $\text{Mg km}^{-1}$ ) for the stability simulations after 1.5 hours of burning. Linear plots (a,c) and logarithmic plots (b,d), for the 2km radius (a,b) and 4km radius (c,d) ignitions are shown. . . . .	58
3.10	Percent of smoke reaching the upper troposphere (a,c) and stratosphere (b,d) compared with wind speeds (red) and maximum vertical velocity in the domain compared with wind speeds (blue), for the 2-km radius ignition (a,b) and the 4-km radius ignition (c,d). . . . .	59

3.11	Maximum vertical velocity (a,b) and maximum CAPE within the fire area (c,d) compared with % smoke rise above 9 km (a,c) and total smoke rise above 9 km in Mg (b,d), for all 20 simulations. The unfilled markers indicate values from the 2-km radius ignition, while the solid markers correspond to the 4-km radius fire. Each plot has regressions plotted over their 2-km (dotted) and 4-km (dashed) subsets of data points. . . . .	61
3.12	Height above which half of the smoke is lofted, based on the final vertical profiles, for each simulation (circles). Smaller markers indicate the 2-km radius fire; larger markers indicate the 4-km radius fire. Markers are colored according to the amount of smoke generated by that simulation. Additionally, the heights above which 25% and 75% of the smoke is lofted are indicated by triangles (upward facing for 25%, downward for 75%), with smaller, hollow markers signifying the 2-km radius ignition, and larger, filled markers signifying the 4-km radius ignition. . . . .	64
3.13	Final vertical smoke distributions of fires simulated in Penner et al. (1986) (dotted), Reisner et al. (2018) (dash-dotted), and this study (HiWi_2 and MR75_2 only, solid). 9 km height is marked by the horizontal dashed line. . . . .	65
4.1	Domain extents. The Pacific Ocean is indicated by blue on the western side of the outer domain, while parts of California, Nevada, Oregon and Idaho are all captured by the green area. The fire is indicated by the black marker in d03. . . . .	78
4.2	W-E cross sections of integrated cloud mass in the N-S direction. Ice, snow, and graupel are considered "cold," while rain and cloud water are "warm." The time stamps of each plot are for August 2 PDT. Plots a, d, and g show the rapid cold cloud progression for noWFA; b, e, and h show the same for WFA; and c, f, and i show the same for SMK. . . . .	81

4.3	Model sounding at the leading (west) side of LES nest, centered in the N-S direction. The green line indicates the dew point temperature profile. The red line shows the atmospheric temperature profile. Moisture at around 350 mb is advected into the region. . . . .	82
4.4	Total area burned and change in area burned over time, shown at 1 hr intervals starting with ignitions (a, b) and at 5 min. intervals for the last four hours of the simulation (c, d). The change in burn area is plotted as a rolling 15-minute average.	83
4.5	Total heat flux from the fire over time, for each simulation, output at 5 min. intervals and shown with a 15 min. moving average. . . . .	84
4.6	Maximum winds at each height in the domain for each hour of the simulations, beginning at 00:00 on August 1. Plots a, b, and c depict maximum horizontal wind speeds. Plots d, e, and f show maximum updraft speeds. Plots g, h, and i present maximum downdraft speeds. The left hand column (a, d, g) show results for noWFA. The center column (b, e, h) show results for WFA. The right hand column (c, f, i) show results for SMK. . . . .	85
4.7	Maximum winds at each height in the domain for the last four hours of the simu- lations, beginning at 12:00 on August 2 and plotted at 5 minute intervals. Plots a, b, and c depict maximum horizontal wind speeds. Plots d, e, and f show maximum updraft speeds. Plots g, h, and i present maximum downdraft speeds. The left hand column (a, d, g) shows results for noWFA. The center column (b, e, h) shows results for WFA. The right hand column (c, f, i) shows results for SMK. . . . .	86
4.8	Differences in maximum winds at each height in the domain for the last four hours of the simulations, beginning at 11:00 on August 2 and plotted at 5 minute intervals. Plots a and b depict maximum horizontal wind speeds. Plots d and e show maximum updraft speeds. Plots g and h present maximum downdraft speeds. The left hand column (a, c, e) shows results for noWFA minus WFA. The right hand column (b, d, f) shows results for WFA minus SMK. . . . .	87

4.9	Time series of cloud top temperature for all three simulations, from ignition to termination (a), and for the last four hours of the simulation (b). CTTs are plotted with a rolling 15-minute average. . . . .	88
4.10	Time series of total liquid and solid water mass in the domain, for the last four hours of the simulation, broken out into cloud water (a), ice (b), snow(c), graupel (d), rain (e), and all summed together (f). The time series are plotted with a rolling 15-minute average. . . . .	89
4.11	Time series of (a) rain and (b) ice particles in the domain, for the last four hours of the simulation. The time series are plotted with a rolling 15-minute average. . . . .	90
4.12	Time series of (a) total smoke, (b) smoke lofted above 3km (estimated average boundary layer height), and (c) smoke lofted about 6km, for the last four hours of the simulation. The time series are plotted with a rolling 15-minute average. . . . .	91
A.1	Hub height wind (80 m) speed differences between the RWFP (REWS only) and the WFP in a stable environment. The plots on the left hand side depict the wakes seen with the WFP in SR_06 (a) and SR_10 (c). The right hand side plots show the differences in waking between the REWS RWFP and the WFP in SR_06 (b) and SR_10 (d). . . . .	121
A.2	Percentage differences in average power output between the WFP and the RWFP (REWS only) in a stable environment for SR_06 (a), SR_08 (b), and SR_10 (c). . . . .	121
A.3	The left plot (a) depicts the wakes that develop at hub height (80 m) when the WFP is activated for the cold pool mix-out simulation with the inversion level at 80 m (M_80). The wind speed at hub height is below the cut-in speed for the turbines, so they do not produce power. The right plot (b) depicts the difference in waking between the REWS and WFP simulations with the 80 m inversion level. The REWS enables the turbines to see a wind speed above the cut-in velocity, and the turbines produce power and generate wakes. . . . .	122

## Chapter 1

### Introduction

The world is at a critical point right now. We face a host of existential global security risks—the largest of which is climate change. Anthropogenic climate change, brought on by our use of and reliance on fossil fuels, presents the world with grave new challenges and environmental threats. A transition away from carbon-based fuel sources is necessary, but it is fraught with physical, political, financial, and cultural obstacles—which has made it an arduous and slow process. However, the more time that passes without successful mitigation and adaptation efforts, the more severe the dangers presented by climate change become.

Humans have relied on fossil fuels to accommodate steadily rising energy demand worldwide since the Industrial Revolution (Zhou et al., 2012). While fossil fuels offer many benefits—high energy density and self-contained storage, making them particularly ideal for transportation applications—they release a great deal of carbon dioxide ( $\text{CO}_2$ ) into the atmosphere: up to 228.6 pounds per Btu (coal) (EIA, 2020b, 2020b). Carbon dioxide has been shown to interact with incoming solar radiation in a phenomenon known as the greenhouse effect, causing it and the surrounding air to warm.  $\text{CO}_2$ , combined with other gases having similar radiative interactions, are known as “greenhouse gases.” The Keeling Curve, combined with historical temperature and ice core data, demonstrates the strength of the  $\text{CO}_2$ -temperature correlation here on earth (Fig. 1.1). Average surface temperatures were 1.15°C above the pre-industrial average in 2019, and they are expected to continue to rise (R. Lindsey & Dahlman, n.d.). Consequently, we face a significantly warmer world in years to come if we do not shift away from carbon-based fuel sources to zero-emissions en-



ergy. The International Panel on Climate Change (IPCC) has released a series of reports outlining Representative Concentration Pathways (RCPs), which are projections of warming by the end of the century based on future atmospheric greenhouse gas concentrations. The worst case scenario, RCP8.5, predicts a temperature rise of up to nearly  $5^{\circ}\text{C}$  above the 1850-1900 global average temperature, which coincides with a situation wherein no mitigation efforts are carried out (Pachauri, R. K., Mayer, L. and Intergovernmental Panel on Climate Change, 2015).

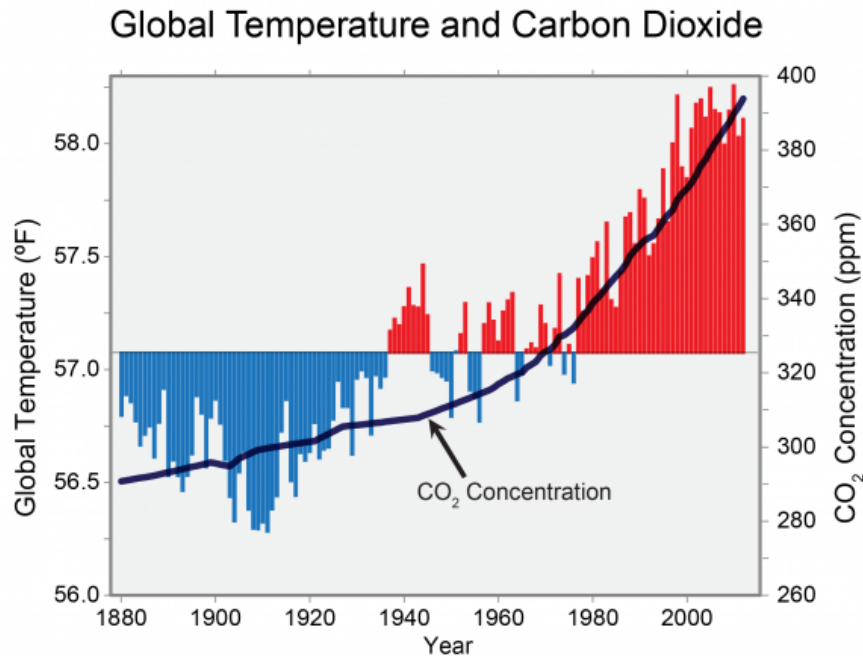


Figure 1.1: Average global temperatures and atmospheric carbon dioxide concentrations, 1880-2014. Figure from Melillo et al. (2014).

Widespread, global warming will not only fundamentally change ecosystems and lead to extinctions, it will also have complex consequences for the human population. More frequent and intense extreme weather such as hurricanes, floods, drought, severe heat, and wildfire have already begun to claim lives, destroy livelihoods, and generate huge financial costs (Stott, 2016; Mann et al., 2017; Abatzoglou, Williams, & Barbero, 2019; Frame et al., 2020). Mass migrations are anticipated as communities will be forced to move away from areas that are flooded by sea level rise or destroyed by fire, have become too dry to sustain subsistence agriculture, no longer have

reliable fresh water available, or are simply too hot (Adger et al., 2014; Berlemann & Steinhardt, 2017). Additionally, worldwide food security is threatened as ocean warming and acidification endangers ocean life, and staple agricultural regions are jeopardized by shortened growing seasons, temperatures too high to sustain certain crop growth, and strain on freshwater systems (Pörtner et al., 2019; Porter et al., 2014). Specific vector-borne diseases spread by insects and certain chronic health conditions related to heat stress stand to become more prevalent and widespread (K. Smith et al., 2014). And, with complicated and sometimes strained relationships among peoples, societal clashes and escalating international tensions are expected (Adger et al., 2014). These are all global security issues.

There are ways we can address these problems. While it is too late to avoid the entirety of climate change fallout, adaptation and mitigation efforts, if combined, have the potential to protect both people and ecosystems from the full impact of a several-degree rise in temperature. Fortunately, numerical weather prediction models (NWP) have demonstrated effectiveness in forecasting severe weather dangers and atmospheric behavior. For this reason, they can assist with both mitigation and adaptation. NWP can improve wind power forecasting, paving the way for more efficient wind farm operations and smarter planning of new farm development. NWP can also provide real-time forecasting of fire behavior, which informs communities and decision makers of where evacuations need to occur and how best to tackle fire containment. Models can also be used in research applications to help us better understand hypothetical future situations and develop a better awareness of wind or fire dynamics.

## **1.1 Scope of the Study**

For the purpose of this thesis, one mitigation measure and one adaptation topic have been selected for further assessment with the Weather Research and Forecasting model (WRF)—an open-source, community numerical weather prediction system that allows for both mesoscale and large-eddy resolution simulations (C. Skamarock et al., 2019). First, an adjustment to the WRF wind farm parameterization and its significance for wind power forecasting is explored in Chapter

2. Then, the dissertation focus shifts to fire impacts—specifically, smoke lofting and deep cloud development above large wildland fires in Chapters 3 and 4.

### 1.1.1 Wind Energy Forecasting

Since the start of the 21st century, wind energy installations have been expanding rapidly, with both domestic and international wind power capacity growing each year. By the beginning of 2020, 650.8 GW of wind energy capacity had been installed worldwide (Fig. 1.2) (World Wind Energy Association, 2020). At the termination of Q2 2020, nearly 110 GW of capacity was operating in the U.S., which provided 7.3% of the nation’s primary energy production (EIA, 2020a; Services, 2020). Wind’s growing share in the energy market makes accurate wind-power forecasts more important. Optimized forecast-based grid schedules reduce the use of ancillary services, which boosts wind’s market value and increases the incentive for further investment (Ayodele, Jimoh, Munda, & Agee, 2012). Wind energy is inherently variable, as its electricity generation changes with the wind. Therefore, to properly prepare for sudden dips and increases in production and to adjust grid operations accordingly, we must have accurate wind and power production forecasting capabilities in place.

Wind energy forecasting has historically been done with mesoscale modeling, where horizontal grid cell resolution is on the order of 1 to 10 km, as scaling down to finer resolutions becomes quite computationally expensive (Churchfield et al., 2012; Vanderwende, Kosović, Lundquist, & Mirocha, 2016). However, most mesoscale models have been developed to resolve local weather events and general patterns; they lack precision closer to the earth’s surface, where a refined resolution is needed to accurately depict the forces driving wind turbine energy production. Near-surface errors increase in regions of complex terrain, where flow patterns can be disrupted by orography, making accurate wind predictions very challenging. These areas are also prone to more extreme wind shear lower in the boundary layer, which further complicates assessments of turbine rotation speed (Redfern, Olson, Lundquist, & Clack, 2019; Olson et al., 2019). Studies have been done to improve our understanding of wind behavior in mountainous areas—for example, the 2015 WFIP2 study

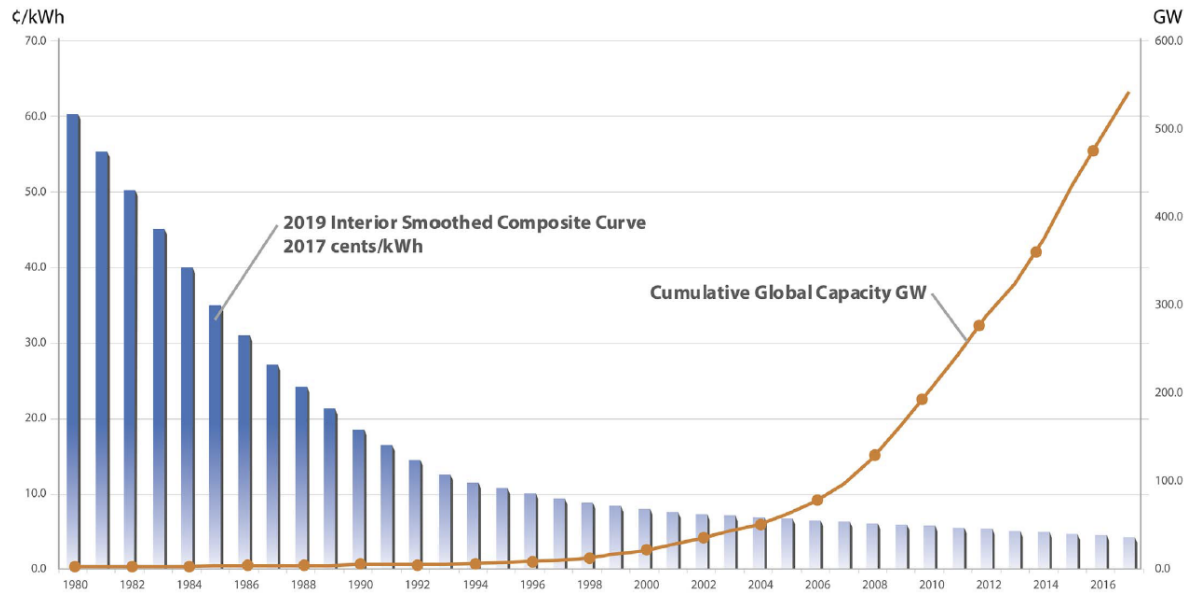


Figure 1.2: Cumulative global wind installations, 1980-2016. Figure from Veers et al. (2019).

in Oregon (Wilczak et al., 2019; Shaw et al., 2019), and the 2017 Perdigueo campaign in Portugal (Vasiljević et al., 2017; Barthelmie, Pryor, Wildmann, & Menke, 2018; Fernando et al., 2019), but development of the findings in models is ongoing.

Mesoscale-microscale coupling is currently being explored, as it would allow larger, regional models to obtain and use the refined wind profiling of large-eddy simulation (LES, on the order of 1-100 m resolution) grids for wind resource assessment (Muñoz Esparza, Kosović, Mirocha, & van Beeck, 2014; Haupt et al., 2019; Veers et al., 2019). However, this area comes with its own sets of challenges, in particular when downscaling through resolutions on the order of around 100 m to 1000 m—a region known as the “terra incognita”. Grid cells of this size fall in a challenging range of length scales, in general larger than inertial range and only partially resolving energy containing range of scales (Wyngaard, 2004). Because of this, ensuring that mesoscale wind farm parameterizations (WFPs) are as accurate as possible and addressing the findings of the aforementioned field campaigns is currently one of the more efficient ways to curtail errors in wind power forecasting. This will lead to improvements in wind-grid integration and ideally promote a more resolute transition towards this clean energy source.

### 1.1.2 Fire Applications

Climate change has increased both the frequency and severity of wildland fires. As heat and water stress have risen and invasive insect outbreaks occur in woodland areas, tree mortality has increased, raising the risk of wildfire (Allen et al., 2010). This phenomenon has been made apparent in more recent years, when wildfires have burned unprecedented amounts of land in Australia, the Pacific Northwest, Colorado, and California, among many other places around the world (Boer, Resco de Dios, & Bradstock, 2020; Kablick, Allen, Fromm, & Nedoluha, 2020; Peterson et al., 2018b; A. P. Williams et al., 2019; Yu et al., 2019). Such fires have destroyed homes, devastated ecosystems, claimed lives, and racked up enormous costs. The intensity of these fires is remarkable; they have burned with such great heat release and generated such strong convection that they have seeded thunderstorms, also known as pyrocumulonimbus (pyroCb)—some strong enough to generate hail, tornadoes, and even inject combustion byproducts into the stratosphere (M. Fromm, Tupper, Rosenfeld, Servranckx, & McRae, 2006; Cunningham & Reeder, 2009). The 2017 Pacific Northwest fires lofted enough smoke into the stratosphere to parallel what would be seen following a volcanic eruption (Peterson et al., 2018b). In the case of the 2019 Australian wildfires, enough smoke and gaseous emissions were injected above the tropopause that stratospheric wind patterns were affected (Kablick et al., 2020).

High smoke lofting has been a concern in the past, but in a different context. When the U.S. and Russia were both engaged in nuclear proliferation during the Cold War, researchers were troubled by the potential fire-driven fallout of a nuclear arms exchange. Cities would provide dense fuel loads with the potential to burn for days, injecting teragrams of smoke into the upper atmosphere and resulting in what was come to be known as a "nuclear winter" (Turco, Toon, Ackerman, Pollack, & Sagan, 1983b). In this situation, increased stratospheric aerosol loading would block incoming solar radiation, significantly cooling and darkening the earth for years before eventually falling out. The impact on most all life forms would be catastrophic. Now that some nuclear states are beginning to turn away from denuclearization and back towards weapons development, nuclear

winter risk has once again become a global security concern (Robock, Oman, & Stenchikov, 2007; Robock & Toon, 2012b; Mills, Toon, Lee-Taylor, & Robock, 2014; Robock, Toon, Bardeen, Xia, et al., 2019; Coupe, Bardeen, Robock, & Toon, 2019a).

With the new risks posed by more intense fires, as well as by world renuclearization, better models of fire behavior and fire-atmosphere interactions can help us address these dangers. Operational fire forecasting gives us the ability to predict where a fire might spread once ignited, which gives firefighters more time to strategize containment methods. Models can also give new insight into fire research efforts on the development of pyroCb, so that we may better understand how these storms form and behave, and how they may affect local fire behavior or even climatology both near and far. Additionally, models can help us address the reborn existential threat of nuclear winter, and hopefully better inform nation-states of the significant risks associated with a nuclear conflict.

## 1.2 Arrangement of the thesis

This dissertation aims to assess modeling methods for improving wind energy forecasting and better understanding smoke lofting behavior resulting from large fire activity. Each chapter includes a stand-alone study formatted for publication in a peer-reviewed journal. Chapter 2 has been published in 2019 in the AMS journal *Monthly Weather Review*. Chapter 3 is in preparation for submission to *JGR: Atmospheres* and Chapter 4 is also in preparation for submission to a different journal, *Atmospheric Chemistry and Physics*. Each chapter opens with a preface outlining the motivation and major findings of the study contained therein. The final chapter provides a summary of each study, their findings, and their implications in the broader context of our future climate.

## Chapter 2

# Incorporation of the Rotor-Equivalent Wind Speed into the Weather Research and Forecasting Model's Wind Farm Parameterization

### 2.1 Preface

Wind energy has been expanding to provide a larger percentage of electrical power around the world. Wind is a renewable energy resource with a levelized cost of energy that is now competitive with coal. Because of this, many nations are increasing their wind farm installations. However, because winds are variable, unforeseen fluctuations in wind speed and direction can impact demand-matching and grid stability. Given its rising presence in electricity generation, it is therefore all the more important that wind energy forecasting is as accurate as possible.

In this section, we examine the impact of adding more detailed physics in the form of the rotor-equivalent wind speed (REWS) to the WRF Wind Farm Parameterization. Wind energy forecasting at the farm-level is often carried out with use of mesoscale-resolution models. The interactions between the turbines and the local atmosphere are therefore parameterized, considering hub-height wind speed to be representative of the entire wind profile across the rotor swept area. With growing turbine sizes—particularly in offshore wind—this assumption is not necessarily true.

We have conducted a sensitivity analysis of forecast response to a selection of linear and non-linear wind profile cases in a series of idealized model simulations. The results indicate that with present, typical turbine sizes, use of the hub height wind speed often does not present significantly different results from simulations run with the REWS. However, in non-linear wind shear situations, the difference between the two physics options is not negligible. This finding should be kept in mind

as turbines increase in size and the likelihood of a non-linear wind shear occurrence increases.

The work presented in this chapter has been reformatted from the following:

Redfern, S., Olson, J. B., Lundquist, J. K., & Clack, C. T. (2019). Incorporation of the rotor-equivalent wind speed into the Weather Research and Forecasting model’s wind farm parameterization. *Monthly Weather Review*, 147(3), 1029-1046.

## 2.2 Abstract

Wind power installations have been increasing in recent years. Because wind turbines can influence local wind speeds, temperatures and surface fluxes, weather forecasting models should consider their effects. Wind farm parameterizations do currently exist for numerical weather prediction models. They generally consider two turbine impacts: elevated drag in the region of the wind turbine rotor disk and increased turbulent kinetic energy production. The wind farm parameterization available in the Weather Research and Forecasting model (WRF) calculates this drag and TKE as a function of hub-height wind speed. However, recent work has suggested that integrating momentum over the entire rotor disk (via a rotor-equivalent wind speed, or REWS) is more appropriate, especially for cases with high wind shear. In this study, we implement the REWS in the WRF wind farm parameterization and evaluate its impacts in an idealized environment, with varying amounts of wind speed shear and wind directional veer. Specifically, we evaluate three separate cases: neutral stability with low wind shear; high stability with high wind shear; and high stability with nonlinear wind shear. For most situations, use of the REWS with the wind farm parameterization has marginal impacts on model forecasts. However, for scenarios with highly nonlinear wind shear, the REWS can significantly affect results.

## 2.3 Introduction

Wind energy has become increasingly important over recent years. Wind energy contributed 5.56% of baseload power to the United States in 2016 (Administration, 2017) and as of 4Q 2017, the United States has 87,077 MW of cumulative, installed wind power capacity, with 28,668 MW



under construction (Services, 2017). Globally, 539,581 MW of wind power capacity is installed, with 52,573 MW of new construction added in 2017 (Griffith, 2018). Wind power will likely continue to expand as the economics of renewable energy are becoming progressively favorable (E. Williams et al., 2017; Services, 2017). With this growth in mind, operational weather forecasting models may need to consider how turbines affect the atmosphere.

Observational studies have demonstrated that wind farms can have microscale effects on atmospheric properties such as winds, temperature, and heat and moisture fluxes. Wind farms extract kinetic energy from the wind, resulting in wakes (S. Lissaman, 1979; Högström et al., 1988; Wang & Prinn, 2010; Iungo et al., 2013; C. M. Smith et al., 2013). Several studies have found a nighttime warming trend downwind of wind farms (Baidya Roy & Traiteur, 2010; Zhou et al., 2012; C. M. Smith et al., 2013; Rajewski et al., 2013; Armstrong et al., 2016; Rajewski et al., 2016), which is likely due to vertical mixing induced by turbine operation. Daytime increases in upward latent heat flux and downward CO<sub>2</sub> flux also occur (Rajewski et al., 2013). As these effects are not negligible, they should be considered in weather models.

To account for turbine impacts, wind farm parameterizations (WFPs) have been developed for mesoscale models (Baidya Roy, 2004, 2011; Fitch et al., 2012). Baidya Roy (2004) implemented a parameterization in the Regional Atmospheric Modeling System (RAMS) to evaluate how wind farms impact local-scale atmospheric dynamics. This WFP modeled turbines as both a momentum sink and a turbulence source, and showed that turbines have small impacts on surface sensible heat fluxes and evapotranspiration, presumably due to the increased near-ground turbulence. The study also found that turbines significantly reduce wind speeds around hub-height. Blahak et al. (2010) and Fitch et al. (2012) later developed WFPs for the Weather Research and Forecasting model (WRF). Fitch et al. (2012) expanded upon Blahak et al. (2010)’s parameterization efforts by basing the momentum extracted from the atmosphere on the manufacturer-specified turbine thrust coefficient.

Some studies have compared WRF wind farm modeling results with observations, and most note some bias in the parameterization. Comparisons between the WRF WFP and power data

taken at the Horns Rev wind farm off the coast of Denmark found that simulations with the WFP qualitatively reproduced wake structures but overall under-forecasted power production for downstream turbines (Jiménez et al., 2015). An additional study comparing WRF WFP mesoscale simulations with data collected in an onshore wind farm in the US Midwest came to a similar conclusion: the WFP improved wind power predictions, but again underestimated power production at downwind turbines (Lee & Lundquist, 2017a). Conversely, Vanderwende et al. (2016) compared the WRF WFP to turbine-resolving large-eddy simulations and found in this case that the WFP overestimated TKE production and underestimated the magnitudes of the wakes. And, regarding impacts on near-surface temperatures, G. Xia et al. (2017) showed that although the WFP reproduced larger-scale, wind farm-driven warming signals consistent with observations, it also caused a nighttime, downwind cooling effect that is currently unverified by measurements.

Before including a WFP in an operational weather forecasting model, the WFP should accurately represent the interactions of wind turbines with atmospheric events, for all possible scenarios. Aside from the suspected bias in the WRF WFP, certain situations may arise in which it does not behave as expected. For example, during mountain-valley cold pool mix-out events, strongly stratified cold air is trapped and shielded from higher wind speeds aloft. Robust vertical wind shear develops at the interface between the cold pool and free troposphere, producing turbulence, which begins to erode the stable layer. Eventually, the overhead winds descend low enough to intersect the turbine rotor layer, resulting in episodes of very high wind shear profiles across the rotor plane. These cold pool events in complex topography occur with regularity; 120 events occurred in the Columbia River basin between 1989-1999 (Whiteman et al., 2001), and in the recent WFIP2 project, at least eight have been recognized between November 2015 and December 2016 (Wilczak et al., 2019). Because the WRF WFP only considers hub-height wind speeds in its physics calculations, it may return inaccurate results for cold pool mix-outs.

In light of this potential for error and aforementioned biases in the WRF WFP, we propose two modifications that aim to improve the representation of wind farms in high wind shear environments. In the following section, we summarize the existing WRF WFP and discuss the components of a

revised WRF WFP (RWFP). The RWFP testing setup is explained in the third and fourth sections, testing results are presented in section five, and section six details the conclusions from this study.

## 2.4 Wind Farm Parameterization

WRF is a popular community modeling framework (W. C. Skamarock et al., 2008; Powers et al., 2017) upon which many regional weather models have been built, including the National Oceanic and Atmospheric Administration (NOAA)’s High Resolution Rapid Refresh (HRRR). Included in the WRF distribution is a wind farm parameterization, which has been well-documented (Fitch et al., 2012; Fitch, Olson, et al., 2013; Fitch, Lundquist, & Olson, 2013; Fitch, 2015, 2016) and has been employed at regional (Jiménez et al., 2015; Volker et al., 2015; Lee & Lundquist, 2017a, 2017b) and continental scales (Vautard et al., 2014).

### 2.4.1 Current Distribution of WFP

The Fitch et al. (2012) parameterization (henceforth referred to as F2012) comes packaged in the WRF distribution. Users must specify turbine properties, such as hub-height, rotor diameter, maximum power output, and they must also provide power and thrust coefficient curves. Most of the parameterization derivations are explained in detail in F2012. Updates made to the WFP in 2015 are documented in the model code and addressed in a note (Fitch 2016). Some important aspects and assumptions of the current WRF WFP are highlighted below.

#### 2.4.1.1 Power Generation

Power generation in the model assumes that turbines are driven by the hub-height wind speeds, with a constant sea level air density of  $\rho_a = 1.23 \text{ kg m}^{-3}$ . It should be noted that this assumption may introduce calculation errors at high elevations. However, for the code to account for variable atmospheric pressure would also require one to obtain density-specific power curves for each turbine used in a simulation, as the power curve delivered with the turbine is rated based on empirical testing done at sea level. Often this information is proprietary, so the WFP as it is

assumes sea-level air density throughout the domain. Power production from an individual grid cell is defined as

$$P_{ij} = \frac{1}{2} (C_P \rho_a |\mathbf{U}_H|^3 A_T N_t)_{ij}. \quad (2.1)$$

Here,  $|\mathbf{U}_H|$  is hub-height wind speed,  $C_P$  is the turbine power coefficient at the hub-height wind speed,  $A_T$  is the turbine swept area defined as  $A_T = \frac{\pi}{4} D^2$ , and  $N_T$  is the number of turbines per grid cell, located at  $(i, j)$ . Power output is calculated every time step for each grid cell containing a turbine.

#### 2.4.1.2 TKE and Momentum Tendencies

The WRF WFP assumes that all turbines in a particular grid cell are driven by the mean wind speed in that grid cell and subgrid-scale heterogeneity is ignored. Further, the momentum drag and turbulent kinetic energy (TKE, or kinetic energy per unit mass in  $\text{m}^2 \text{s}^{-2}$ ) produced by each turbine are evenly distributed through the cell and no explicit wake interactions occur between turbines in a given model grid cell. To calculate the sum of individual turbines F2012 introduced a **wind farm density** variable, which is defined as the number of turbines per square meter. The wind farm density is multiplied through the drag and TKE tendency equations to determine the full impact of the turbines on a per-grid cell basis.

The parameterization assumes that the drag force induced by the turbines on the atmosphere is defined by the basic drag equation:

$$P_{ij} = \frac{1}{2} (C_D \rho_a |\mathbf{U}|^3 A_T N_t)_{ij}. \quad (2.2)$$

Here,  $\mathbf{U}$  is the velocity vector, defined as  $\mathbf{U} = (u, v)$ , and  $C_D$  is the coefficient of drag—in this case, it is equivalent to the turbine thrust coefficient,  $C_T$ , which is a function of wind velocity and is specific to the turbine used.

The change in atmospheric kinetic energy (KE, in  $\text{kg m}^2 \text{s}^{-2}$ ) from air-turbine interactions,

therefore, can be derived as follows:

$$\frac{\partial KE_{Drag}}{\partial t} = -\frac{1}{2} \int_{A_t} C_T \rho_a |\mathbf{U}|^3 dA. \quad (2.3)$$

For numerical simulations, this equation must be discretized across model vertical levels, wind components, and horizontal grid cells, and must account for the possibility of multiple turbines per grid cell. Additionally, the assumption is made that turbines do not affect vertical winds. In the WRF WFP, 2.3 is therefore discretized as

$$\frac{\partial KE_{ijk}}{\partial t} = \frac{\partial |\mathbf{U}|_{ijk}}{\partial t} |\mathbf{U}|_{ijk} \rho_a (z_{k+1} - z_k) \Delta x \Delta y, \quad (2.4)$$

where  $i$  and  $j$  represent model grid locations in the horizontal and  $k$  represents individual model vertical layers. The wind vector in 2.4, therefore, is taken from the grid cell under evaluation (not necessarily at hub height). By defining the wind farm density variable as  $N_t$ , the momentum tendency can be then derived as

$$\frac{\partial |\mathbf{U}|_{ijk}}{\partial t} = -\frac{\frac{1}{2} N_t^{ij} C_T |\mathbf{U}|_{ijk}^2 A_{ijk}}{z_{k+1} - z_k}. \quad (2.5)$$

The parameterization assumes that all energy extracted by turbines that is not converted to electricity instead generates TKE:

$$\frac{\partial TKE_{ijk}}{\partial t} = \frac{\frac{1}{2} N_t^{ij} C_{TKE} |\mathbf{U}|_{ijk}^3 A_{ijk}}{z_{k+1} - z_k}. \quad (2.6)$$

with the TKE coefficient  $C_{TKE} = C_P - C_T$ .

Revisions to the WRF code since F2012 have added in a “normalization” factor (Blahak et al., 2010) that is multiplied through 2.5 and 2.6 for each WFP-active grid cell. As shown in 2.1, the estimate of power using the turbine-specific power curve is only a function of the hub-height wind speed. However, as shown in 2.1 and 2.6, the multi-layer total tendency calculations employed in the WFP are summations that use wind speeds valid at each model level. The normalization factor aims to make these estimates equivalent, allowing changes in the model wind and TKE to

be consistent with total wind energy production, thus conserving energy. This factor is defined as follows:

$$ec = \frac{\frac{1}{2} (C_P \rho_a |\mathbf{U}_H|^3 A_T N_T)_{ij}}{\sum_{k=turbinebottom}^{turbinetop} \frac{1}{2} (C_P \rho_a |\mathbf{U}_{ijk}|^3 A_{ijk} N_T)_{ijk}}. \quad (2.7)$$

The normalization factor and the power equation are the only two calculations that use hub-height wind speed. It follows that, similarly, the rotor-equivalent wind speed, derived in the following two sections, will only affect these two equations.

#### 2.4.2 Rotor-Equivalent Wind Speed (REWS)

In the equations above, the hub-height wind speed dictates how each turbine responds to the atmosphere. However, the assumption that hub-height wind speed and direction are representative of all wind flow across the rotor plane is not always substantiated. Several studies address this issue. Wagner et al. (2009) demonstrates that the use of wind speeds at hub-height to represent the entire wind profile across the rotor swept area has led to errors in power forecasting. Although using hub-height wind speeds for power production may be an adequate approximation for small turbines, as turbines grow in size the uncertainties introduced by this assumption also grow.

The “rotor-equivalent wind speed” (REWS) addresses this problem by integrating momentum across the rotor disk. By dividing the swept area into a series of horizontal segments, one can calculate a weighted average of the wind speeds:

$$REWS = \sum_{k=1}^N \frac{A_{ijk}}{A_T} |\mathbf{U}_{ijk}|. \quad (2.8)$$

Here,  $A_k$  is the cross-sectional swept area within a model layer being evaluated,  $A_T$  is the total cross-sectional swept area of the turbine blades, and  $|\mathbf{U}_k|$  is the magnitude of the velocity vector in the layer being evaluated.

### 2.4.3 REWS, Considering Veer

Just as wind speed may vary across the turbine rotor disk, wind direction may also vary. We therefore also examine the implications of wind directional shear across the rotor swept plane, or as we specifically define it in this paper to include both clockwise and counter-clockwise shear, veer. Veer can reduce the projected turbine power output (compared with the assumption that all wind intersecting the turbine is aligned normal to the rotor plane). Additionally, veer can influence the TKE generation and energy extracted from the atmosphere in the same manner.

Choukulkar et al. (2016) and Clack et al. (2016) define this veer component in their formulations of equivalent wind speed. This definition builds upon the previously-defined REWS by adding directionality into the equation, as follows:

$$REWS_d = \sum_{k=1}^N \frac{A_{ijk}}{A_T} |\mathbf{U}_{ijk}| \cos(\theta_{ijk}). \quad (2.9)$$

Here,  $\theta_k$  is the angle between the wind direction and the turbine axis, defined as the direction the turbine is facing. This value is zero at hub height. All other variables are as previously defined. In the RWFP, we replace the hub-height wind speed  $|\mathbf{U}_H|$  in 2.1 with  $REWS_d$  defined in 2.9. To account for veer in KE loss and TKE generation, a factor of  $\cos(\theta_{ijk})$  is multiplied through 2.5 and 2.6.

Model layer depth can vary dynamically during a simulation due to changing air temperatures. This should not significantly affect the RWFP calculation, as the parameterization is relatively insensitive to vertical resolution (Fitch et al., 2012) and changes on the order of doubling or halving the resolution are needed to effect 5–10% changes in wake structures. Even with up to 10°C temperature changes, layer depth would only see a 3% change, which is not large enough to meaningfully affect wakes.

#### 2.4.4 Modeling Approach

All simulations are conducted using the Advanced Research version of the Weather Research and Forecasting model (WRF-ARW) (W. C. Skamarock et al., 2008) Version 3.8.1, with National Oceanic and Atmospheric Administration (NOAA) internal edits to the code (Benjamin et al., 2016). The idealized test environment has been simplified: the land-surface, radiation, cumulus, and microphysics schemes have all been turned off, as in F2012.

#### 2.4.5 Domain Setup

The test environment attempts to replicate the idealized setup used in F2012. Two domains are set up in a nested configuration, each with 202 x 202 horizontal grid cells. The fine domain has a horizontal resolution of 1 km and is centered in the coarse domain, which has a horizontal resolution of 3 km. The coarse grid has open radiative boundary conditions. The lateral boundary conditions of the fine grid are horizontally interpolated from the coarse grid at each time step. The domains are coupled using a one-way interaction, where values from the interior domain are not returned to and cannot influence the outer domain. The time step is 9 s for the coarse grid and 3 s for the fine grid. There are 81 vertical levels, with the model top set at 20 km. Twenty-eight vertical layers fall within the lower 200 m of the model and 11 layers intersect the rotor swept area (Figure 2.1). The surface is flat with a specified roughness length of 0.01 m and a pressure of 1013 hPa. This surface roughness length has been selected to minimize turbulent mixing in the lowest model layer, to make it easier to maintain stratification in the initialized profiles. An f-plane with a Coriolis parameter of  $10^{-4} \text{ s}^{-1}$  is used.

##### 2.4.5.1 Physics

The simulation environment uses only surface layer and planetary boundary layer physics. Both are parameterized using the Mellor-Yamada-Nakanishi-Niino (MYNN) level 2.5 scheme (Mellor & Yamada, 1982; Nakanishi & Niino, 2009a). Under this scheme TKE alone is treated as a prognostic variable, while all other higher-order moments are diagnostically calculated. Modifications to



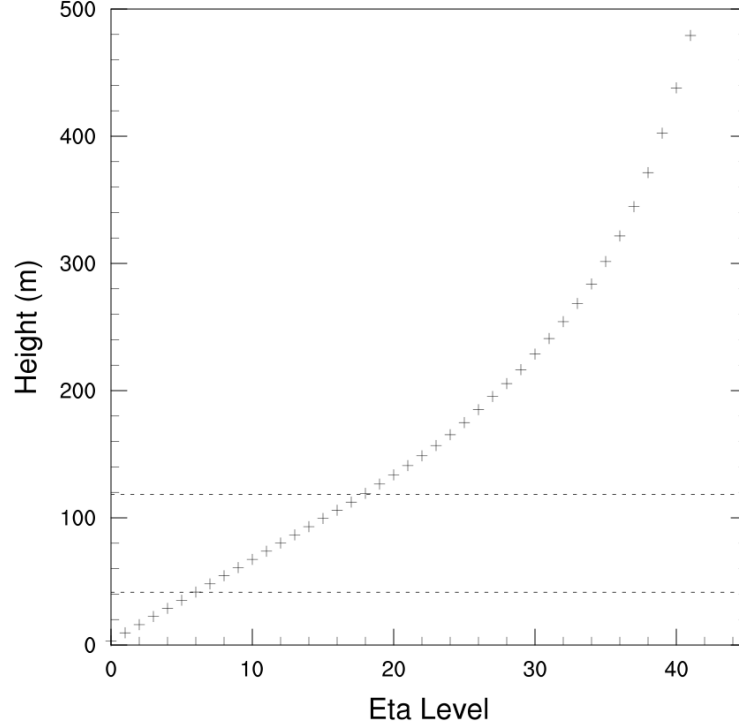


Figure 2.1: Eta levels used for this study, as well as their corresponding heights.

the MYNN scheme’s LES-derived closure constants (Benjamin et al., 2016), which are employed in this study, completely remove the critical Richardson number ( $Ri$ ) of 1, allowing very small mixing to occur even at very large  $Ri$ . Given enough time, wind shear will always mix out. Initializing profiles with  $Ri = 2$  was found to be sufficient to maintain quasi-steady state, high vertical wind shears for the time lengths used in test simulations. The MYNN uses a dynamic turbulence length scale that varies according to atmospheric static stability and TKE. TKE advection has been enabled in the boundary layer. For these simulations, the model is configured such that only the surface momentum flux is calculated in the MYNN surface layer scheme, as the heat and moisture fluxes

are turned off. The atmosphere is dry and remains dry in the absence of these surface fluxes. This simplified configuration is the same one used by F2012 and is employed here so that comparisons between the two studies may be made.

The wind farm is laid out in a 10x10 grid, with one turbine per cell, centered in the fine domain. The coarse grid contains no wind turbines. In contrast to F2012, an open source 1.5 MW wind turbine, based off the GE SLE 1.5MW, is used for the farm, with a hub-height of 80 m and a rotor diameter of 77 m (Schmitz, 2011). The cut-in speed is  $3 \text{ m s}^{-1}$  and the cut-out speed is  $25 \text{ m s}^{-1}$  (Figure 2.2). Winds blowing outside of this velocity range will not rotate the blades or generate power. Power output reaches its maximum at wind speeds of  $12 \text{ m s}^{-1}$ , above which it remains approximately constant before eventually cutting out.

#### **2.4.6 Dynamics**

The WRF model uses a third order Runge-Kutta time integration scheme. The model is configured to reduce the impacts of gravity waves on the simulation results by using an implicit gravity wave dampening layer in the upper-most 5 km of the model domain, in accordance with Klemp et al. (2008), to prevent gravity wave reflection off the model top.

Simple horizontal diffusion is employed, with 2nd order diffusion gradients calculated along coordinate surfaces, which do not use full metric terms. The horizontal eddy diffusion is calculated using the Smagorinsky first order closure approach with a coefficient of 0.25. Additionally, 6th order horizontal diffusion has been activated on model levels, which prevents up-gradient diffusion and reduces  $2\text{-}\Delta x$  wavelength-characterized noise (Knievel et al., 2007).

#### **2.4.7 Initial Conditions**

The RWFP is tested in a series of different idealized atmospheric environments specified by a user-supplied sounding. This sounding contains initial values of domain potential temperature, pressure, inverse air density, and winds, which are calculated using the geostrophic wind balance and interpolated to eta levels.

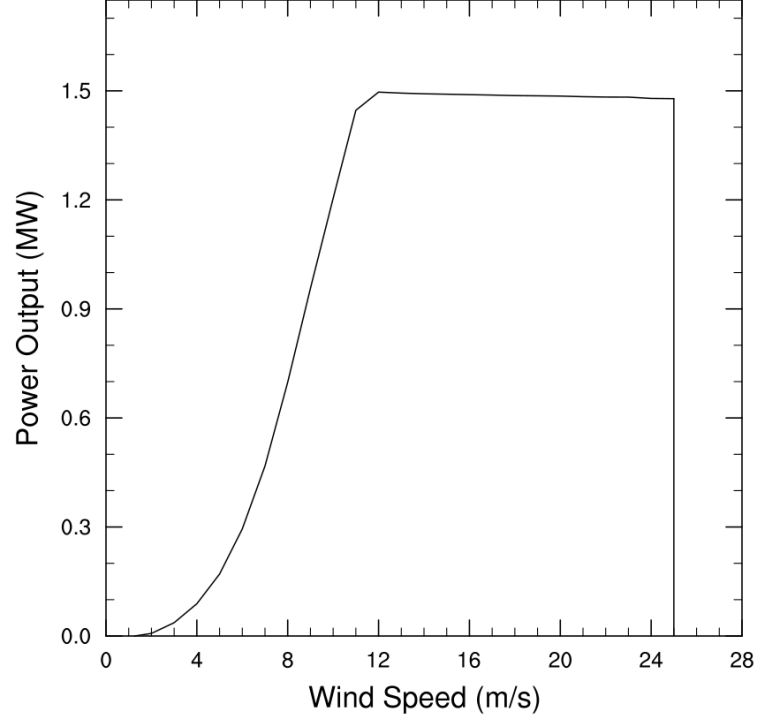


Figure 2.2: Power curve for the PSU Generic 1.5MW Wind Turbine (Schmitz 2011).

To spin up the model, the entire setup – that is, both domains in their full 3D configurations – is run without the wind farm present for a period on the order of days until a steady state is reached. Steady-state is defined by the reduction of the amplitude of inertial oscillations in the winds throughout the domain to less than 2% of the basic state wind speeds. For each subsequent test simulation, the model is restarted from this state, with different WFP configurations. This method significantly reduces the amount of computation resources needed, as the simulation environment does not need to be spun-up for each test run.

## 2.5 Simulation Overviews

Due to the large number of simulations evaluated in this study, a set of acronyms has been defined to reference each one from this point forward. The cases, descriptions, and acronyms can be found in Table 2.1.

### 2.5.1 Neutral Profiles (Cases NF, NR, NV, NB)

A base case simulation is executed for verification purposes. It uses the same initial and forcing conditions as F2012. This environment has constant geostrophic winds blowing at  $10 \text{ m s}^{-1}$  from the model bottom to the model top. The atmosphere is neutrally stratified up to 1000 m, above which a lapse rate is initialized at a constant, stable  $3 \text{ K km}^{-1}$ . The surface temperature is 285 K. After spin-up, the atmosphere equilibrates into a neutral thermal profile with slight variation in wind speed and direction across the rotor plane (Figure 2.3a,b). This simulation is evaluated using both the WFP (NF) and the RWFP (NR, NV, NB). Very little sensitivity to the WFP modifications is anticipated in neutral conditions, so we expect relatively consistent results with F2012.

### 2.5.2 Stable Profiles with Linear Wind Shear (Cases SF, SR, SV, SB)

To assess the role of shear, a series of simulations defined by linear wind shear across the rotor plane is evaluated. The thermodynamics for these cases are all strongly stable below 120 m, with a lapse rate of  $0.1 \text{ K m}^{-1}$  from the ground to 40 m and a potential temperature profile defined by a Richardson number of 2 between 40 m and 120 m. Above 120 m, the atmosphere has a stable  $3 \text{ K km}^{-1}$  lapse rate, as in the previous cases. The winds are calm at  $0 \text{ m s}^{-1}$  up to 40 m, then increase to 6, 8 or  $10 \text{ m s}^{-1}$  (cases ending with 06, 08, 10, respectively) between 40 m and 120 m, above which they remain constant at these values. The winds are initialized to blow zonally only. The robust near-surface inversion is necessary to maintain wind shear in the model; without substantial stability, the winds would mix out to develop a relatively uniform profile throughout the boundary layer. These cases are only spun up for 5 days, which is sufficient to limit noise from

gravity waves propagating within the model domain.

### 2.5.3 Non-linear Wind Shear (Cases MF, MR, MV, MB)

To further examine the effects of the REWS and veer-awareness, we evaluate a stable case with high wind shear related to cold pool mix-out. The initial and forcing conditions are based on observational data obtained during the second Wind Forecasting Improvement Project (WFIP2), a field campaign focused on improving model forecasts of low-level winds over complex terrain (Shaw et al., 2019). The study relies on observations taken by a dense multi-scale network of lidars, sodars, and wind profiling radars located in the United States Pacific Northwest’s Columbia River Basin, where numerous wind farms are located (Wilczak et al., 2019). Data for the project was collected between 01 October 2015 – 31 March 2017 and has captured weather conditions related to cold pools in mountain valleys.

We selected a cold pool mix-out event from 13 January 2016. The profile has been adjusted slightly because the most prominent wind shear is visible across a larger and higher plane than would affect most turbines currently in operation, including the one we have used. Future wind installations will be influenced by a mix-out event like this one as turbines grow in size (Blaabjerg & Ke Ma, 2013; Wiser et al., 2016).

To represent this mix-out event at discrete stages in an idealized framework, a series of three simplified, staggered profiles are simulated. The cold pool is depicted by a layer of relatively calm, easterly winds. The top of the cold pool varies by simulation, from 80 m to 60 m, which represents the sinking of upper-level winds during the mix-out. Above the cold pool are southwesterly winds increasing in speed to  $8 \text{ m s}^{-1}$  at the top of the rotor plane. To prevent rapid near-surface turbulence generation and homogenization of the winds, a strongly stable Richardson number of 2 is maintained for the thermal profile from 0 to 120 m. Above 120 m, winds are held constant (both in direction and intensity), and the lapse rate is stable at  $3 \text{ K km}^{-1}$  up to the model top.

## 2.6 Results

### 2.6.1 Comparison with F2012

An initial comparison with the F2012 results has been conducted to verify proper setup of the simulation environment and to assess how WRF updates in more recent releases will impact WFP results. Some differences emerge between the two studies, which may be explained by the comparisons found in Table 2.2. Overall the findings validate the domain and wind farm parameterization setup.

A wake evolves downwind of the wind farm, with maximum wind speed deficits of  $1.82 \text{ m s}^{-1}$  – stronger than the F2012 maximum of  $1.5 \text{ m s}^{-1}$ . The wake has an e-folding distance through the center of the farm, along the wind direction vector, of 27.3 km (Figure 2.4a). About 2 km upwind of the farm, an induction zone wind speed deficit begins to form, beginning at  $-0.04 \text{ m s}^{-1}$  and reaching  $-0.76 \text{ m s}^{-1}$  at the farm’s leading edge. F2012 saw deficits peaking at  $0.1 \text{ m s}^{-1}$ . A small acceleration flanks the wake, with a slightly larger magnitude ( $0.2 \text{ m s}^{-1}$ ) on the north side than was seen by Fitch, whose maximum acceleration was  $0.1 \text{ m s}^{-1}$ . Similar to F2012, the deceleration of winds ahead of the wind farm extends vertically, perturbing the top of the boundary layer (Figure 2.4c). Wind speed deficits peak at hub height, at the rear edge of the farm.

The TKE impacts deviate from F2012 (Figure 2.4b). Unlike F2012, in this study TKE is enhanced within the farm area and advected downwind of the turbines. The increase in TKE is much lower than what was seen in F2012, with a maximum value of  $0.04 \text{ m}^2 \text{ s}^{-2}$  at hub height. The maximum increase in TKE across the entire 3D simulation area is  $0.16 \text{ m}^2 \text{ s}^{-2}$  and is seen above the farm and downwind of the northeast corner (Figure 2.4d). A reduction in TKE occurs below hub height, with the strongest decrease of  $-0.04 \text{ m}^2 \text{ s}^{-2}$  occurring at about 35 m above ground. Overall, the TKE impact of the WFP is much weaker in this simulation than in F2012. This difference may be attributed to developments to the MYNN PBL scheme between WRF 3.3 and 3.8 as well as from different turbine types used in this study and F2012.

The power output of the farm is greatest in the front line of turbines. Figure 2.5a displays the

fractional power output of each cell, defined as the time-averaged power output of the cell divided by the maximum power output of any cell. The lowest power output is found in the northeast corner of the array, at location (10,10), deviating slightly from F2012, which found that the rear-line turbine directly downwind of the highest-production turbine saw the greatest loss in power output. The south-side turbines located near the southeastern corner of the farm, at (8:10,1), have a greater power output than those located in the rows further north. These turbines are directly exposed to the southerly wind component but are still partially shielded from the turbines to the west. Overall, these results are very similar to those found in F2012.

### **2.6.2 New Physics Options in F2012 Setup (Cases NBASE, NF, NR, NV, NB)**

Very little variation emerges between the neutral case results using the WFP and the RWFP. Simulations have been conducted with each of the following enabled: veer-awareness (NV), the rotor-equivalent wind speed (NR), and both options (NB). In general, the NR case sees the largest differences in TKE, wind speed, and power output, but these differences remain on the order of less than one percent. Although the differences between RWFP cases and the WFP case are negligible, distinct spatial patterns between them do exist. These patterns may grow in magnitude with larger turbine arrays and faster wind speeds.

The wake strength is very slightly increased with NB and NR when compared with the NF case, with negligible change between NV and NF. The e-folding distance in all three RWFP cases remains the same as in the NF case. The largest difference in the magnitude of the wake at hub-height occurs in the NR case, where the maximum deficit is 0.5%, stronger (Figure 2.6a). These differences in wake intensity are the greatest near the rear of the farm and rapidly erode farther downwind.

TKE for all three test cases deviates only slightly from the NF results. In general, TKE is increased with the new physics options. The maximum TKE at hub-height increases by roughly 2% for the NR and NB cases. TKE increases by only 1% for the NV case. These differences are concentrated near the downwind side of the wind farm area (Figure 2.6b).

Overall power is increased for all three test cases, on the order of 1.6% (not nominal) or less. The NR case sees the greatest increase throughout the farm, at 1.4 MW total. Although production from the highest output turbines decreases (-9% for NR), output from the lowest production turbines goes up by more (26.5% for NR), resulting in a net overall increase in power output (Figure 2.5b). The NB simulation is dominated by the REWS implementation, so its power values are comparable to those in the NR case. The NV simulation deviates only slightly from the NF case.

These small differences between the test cases and the NF simulation may be attributed to slight nonlinearities in the wind shear profiles intersecting the rotor layer (Figure 2.3a,b), which affect the rotor-equivalent wind speed and consequently influence the way turbines interact with the atmosphere in these simulations. This effect validates our hypothesis that the modifications will have a small impact in neutral environments. We expect that an increased vertical wind shear would have a greater effect on the model results.

### **2.6.3 Comparing Stable Cases, Constant Wind Shear with New Physics (Cases SF, SR, SV, SB)**

As with the neutral case, few differences emerge between the WFP and the RWFP in the high wind-speed-shear cases. Although vertical wind shear is strong in these simulations (Figure 2.33c), the profile is linear and there is no veer across the rotor swept plane (Figure 2.3d). This results in the REWS and hub-height wind speeds being very similar for all cases. Therefore, the discrepancies in waking, TKE development, and power generation once are again nominal, and no meaningful difference emerges between the SV and SF cases.

The SR\_06 simulation sees the largest deviation from the SF cases in all three evaluated output variables (wake strength, TKE generation, and power production). At the wake's deepest point, it is enhanced by 0.5%, and at its shallowest point it declines by 1.3%. Similarly, TKE is increased by 7.7% at its peak, and reduced by 5% at its minimum. Since wind speeds are already low in these simulations, these changes in waking and TKE are negligible. Overall power output is increased by 8.5%, or 165 kW, which may also be considered insignificant (not shown).



#### 2.6.4 Comparing Stable Cases, Non-linear Wind Shear with New Physics (Cases MF, MR, MV, MB)

Unlike the previous two cases, the cold pool mix-out simulations present more significant differences between RWFP and WFP results. The wind speed and wind direction profiles after spin-up (Figure 2.3e,f) are highly nonlinear. This “staggering” of the two layers impacts the weighted averaging of the RWFP so that the REWS deviates significantly from hub-height wind speed. Additionally, this nonlinearity can dictate whether the turbines turn on (MF\_70, MV\_70) or remain inactivate (MR\_70, MR\_80).

The wake structures strengthen as the inversion moves lower in the atmosphere, analogous to a cold pool being mixed out. When the inversion is set at 80 m, the turbines do not activate, as both hub height and REWS wind speeds are below the cut-in speed of  $3 \text{ m s}^{-1}$ . At 70 m, wind speeds are high enough to turn on the turbines for the MF\_70 and MV\_70 cases. However, the turbines in MR\_70 and MB\_70 remain off. The influence of the REWS lowers wind speeds seen by the turbines to below-cut-in levels. At 60 m, all turbines are on. The M\_60 simulations, therefore, highlight how the different WFP physics influence the winds seen by the turbines and the strengths of the wakes they produce (Figure 2.7). The REWS tends to reduce the wind speed driving the turbines during cold-pool mix-outs, while veer-awareness has a nominal effect. The maximum wake of the MR\_60 case is weakened by 4.7%. With veer-awareness added to REWS (MB), this reduction in wake strength is slightly larger, 4.9%.

The differences in TKE generation are negligible, with the greatest impacts being seen in the MB cases. The largest change is a 12% reduction in the minimum TKE produced in the MB\_60 case, as compared with the MF\_60 case. However, since the TKE is already so low to begin with, this change is trivial.

Power production begins as the inversion drops low enough to raise wind speeds above the cut-in velocity of  $3 \text{ m s}^{-1}$ . As was seen with the waking differences, the REWS reduces the wind speeds driving the turbines. Therefore, turbines in the MF and MV simulations cut in when the inversion

drops to 70 m, but the MR and MB cases do not experience strong enough winds to activate their turbines until the inversion lowers to 60 m (Figure 2.8). In these simulations, the smaller REWS, compared with hub-height winds, results in 41.5% less power production for MR\_60 and 44% less for MB\_60. Veer-awareness has a mixed, yet negligible, impact on power production. At lower wind speeds (MV\_70), it increases power output by 3.2%; however, as the velocity increases, this impact drops to 0.003% (not shown).

## 2.7 Discussion and Conclusions

This study compares the WRF 3.8.1 WFP scheme with a revised WFP (RWFP) that includes two new wind-turbine physics options: 1) the use of the rotor-equivalent wind speed (REWS) instead of hub-height wind speed and 2) the consideration of wind veer across the rotor swept plane. Several simulation environments are set up and evaluated. All are run with the idealized WRF framework. Comparisons are made between results obtained using the WFP and the RWFP. The first set of simulations mirrors the neutral stability setup used by Fitch et al. (2012). The second set of simulations is run in a stable environment with linear wind shear across the rotor layer. The final set of simulations represents a cold pool mix-out—a phenomenon that occurs in the Pacific Northwest’s Columbia River Basin (Whiteman et al., 2001).

Despite former studies emphasizing the potential impact of the REWS, we find that there are few differences in wake development, TKE generation, and power output between the WFP and RWFP for common neutrally- and stably-stratified cases. With a neutrally-stratified profile, wind shear is low, so the RWFP and the standard WRF WFP scheme return similar results (a 0.5% difference in wake strength). In the stable profile cases, wind shear is mostly linear across the rotor swept plane. The REWS and hub-height wind speeds are therefore similar. The greatest difference in wakening magnitude is 1.3%. Although the physics changes exert some minor influence over the results, as indicated by spatial patterns, the magnitude of the resulting differences is small enough to be considered insignificant.

Even though the first two sets of simulations indicated little impact from the RWFP, the

RWFP does have significant implications for the case of the cold pool mix-out—an environment with high, nonlinear wind shear and veer. The new physics options can make the difference between the wind turbines cutting in or remaining inactive, and the use of the REWS can appreciably affect waking and power production. To better understand the implications of our results, we recommend future research that compares RWFP and WFP results with observational data.

Based on our findings, we conclude that for most cases, the RWFP does not affect model performance in a significant manner. The WFP, therefore, is adequate for most wind power forecasting projects. However, for regions where cold pool mix-out events do occur with regularity—such as the Columbia River Basin, where over 6 GW of wind energy is installed and where cold pools are commonplace in the cool season (Whiteman et al., 2001; Wilczak et al., 2019)—the RWFP can increase the accuracy of wind forecasts. Mountainous regions tend to see the highest amounts of wind shear, so the RWFP should have the largest impact in these areas (Clack et al., 2016). In particular, the final set of results demonstrate that the RWFP may be especially useful for timing the activation of turbines during wind ramp-up or ramp-down events, which occur on short timescales (typically less than a few hours). Additionally, certain low-level jets (LLJs) in very stable boundary layers, as well as some near-surface inversions, can have wind shear similar to what we have modeled in the mix-out simulations. However, the wind speeds in low-level jets dipping close to the planetary surface are typically weak and the shear, therefore, is weak as well (Bonner, 1968; R. Banta et al., 2002; R. M. Banta et al., 2007). We advise that further testing of the RWFP using LLJ observations be conducted to conclusively establish the impact of these events.

## 2.8 Acknowledgements

Stephanie Redfern was supported by a fellowship from NOAA GSD (award number NA17OAR4320101). Julie K. Lundquist was supported by the National Science Foundation (grant number 1413980; project title CNH-Ex: Legal, Economic, and Natural Science Analyses of Wind Plant Impacts and Interactions).

Acronym	Stability	$\Delta$ WSP across rotor	$\Delta$ T across rotor	RWFP or WFP?	Initial veer across rotor
NBASE	Neutral	Constant, 10 m s <sup>-1</sup>	Constant 280 K	No WFP	No Veer
NF	Neutral	10 m s <sup>-1</sup>	Constant 280 K	WFP	No Veer
NR	Neutral	10 m s <sup>-1</sup>	Constant 280 K	RWFP, REWS Only	No Veer
NV	Neutral	10 m s <sup>-1</sup>	Constant 280 K	RWFP, Veer Only	No Veer
NB	Neutral	10 m s <sup>-1</sup>	Constant 280 K	RWFP, REWS, Veer	No Veer
SF_06	Stable linear	a. 0-6 m s <sup>-1</sup>	a. 284-311 K	WFP	No Veer
SF_08		b. 0-8 m s <sup>-1</sup>	b. 284-334 K		
SF_10		c. 0-10 m s <sup>-1</sup>	c. 284-365 K		
SR_06	Stable linear	a. 0-6 m s <sup>-1</sup>	a. 284-311 K	RWFP, REWS Only	No Veer
SR_08		b. 0-8 m s <sup>-1</sup>	b. 284-334 K		
SR_10		c. 0-10 m s <sup>-1</sup>	c. 284-365 K		
SV_06	Stable linear	a. 0-6 m s <sup>-1</sup>	a. 284-311 K	RWFP, Veer Only	No Veer
SV_08		b. 0-8 m s <sup>-1</sup>	b. 284-334 K		
SV_10		c. 0-10 m s <sup>-1</sup>	c. 284-365 K		
SB_06	Stable linear	a. 0-6 m s <sup>-1</sup>	a. 284-311 K	RWFP, REWS, Veer	No Veer
SB_08		b. 0-8 m s <sup>-1</sup>	b. 284-334 K		
SB_10		c. 0-10 m s <sup>-1</sup>	c. 284-365 K		
MF_60	Stable mix-out	Constant 2 m s <sup>-1</sup> to	a. 284-469 K b. 284-487 K c. 284-515 K	WFP	135° at a. 60 m b. 70 m c. 80 m
MF_70		a. 60 m			
MF_70		b. 70 m			
MF_80		c. 80 m			
		2 to 8 m s <sup>-1</sup> by 120 m			
MR_60	Stable mix-out	Constant 2 m s <sup>-1</sup> to	a. 284-469 K b. 284-487 K c. 284-515 K	RWFP, REWS only	135° at a. 60 m b. 70 m c. 80 m
MR_70		a. 60 m			
MR_70		b. 70 m			
MR_80		c. 80 m			
		2 to 8 m s <sup>-1</sup> by 120 m			
MV_60	Stable mix-out	Constant 2 m s <sup>-1</sup> to	a. 284-469 K b. 284-487 K c. 284-515 K	RWFP, Veer only	135° at a. 60 m b. 70 m c. 80 m
MV_70		a. 60 m			
MV_70		b. 70 m			
MV_80		c. 80 m			
		2 to 8 m s <sup>-1</sup> by 120 m			
MB_60	Stable mix-out	Constant 2 m s <sup>-1</sup> to	a. 284-469 K b. 284-487 K c. 284-515 K	RWFP, REWS, Veer	135° at a. 60 m b. 70 m c. 80 m
MB_70		a. 60 m			
MB_70		b. 70 m			
MB_80		c. 80 m			
		2 to 8 m s <sup>-1</sup> by 120 m			

Table 2.1: Overview of idealized simulations.

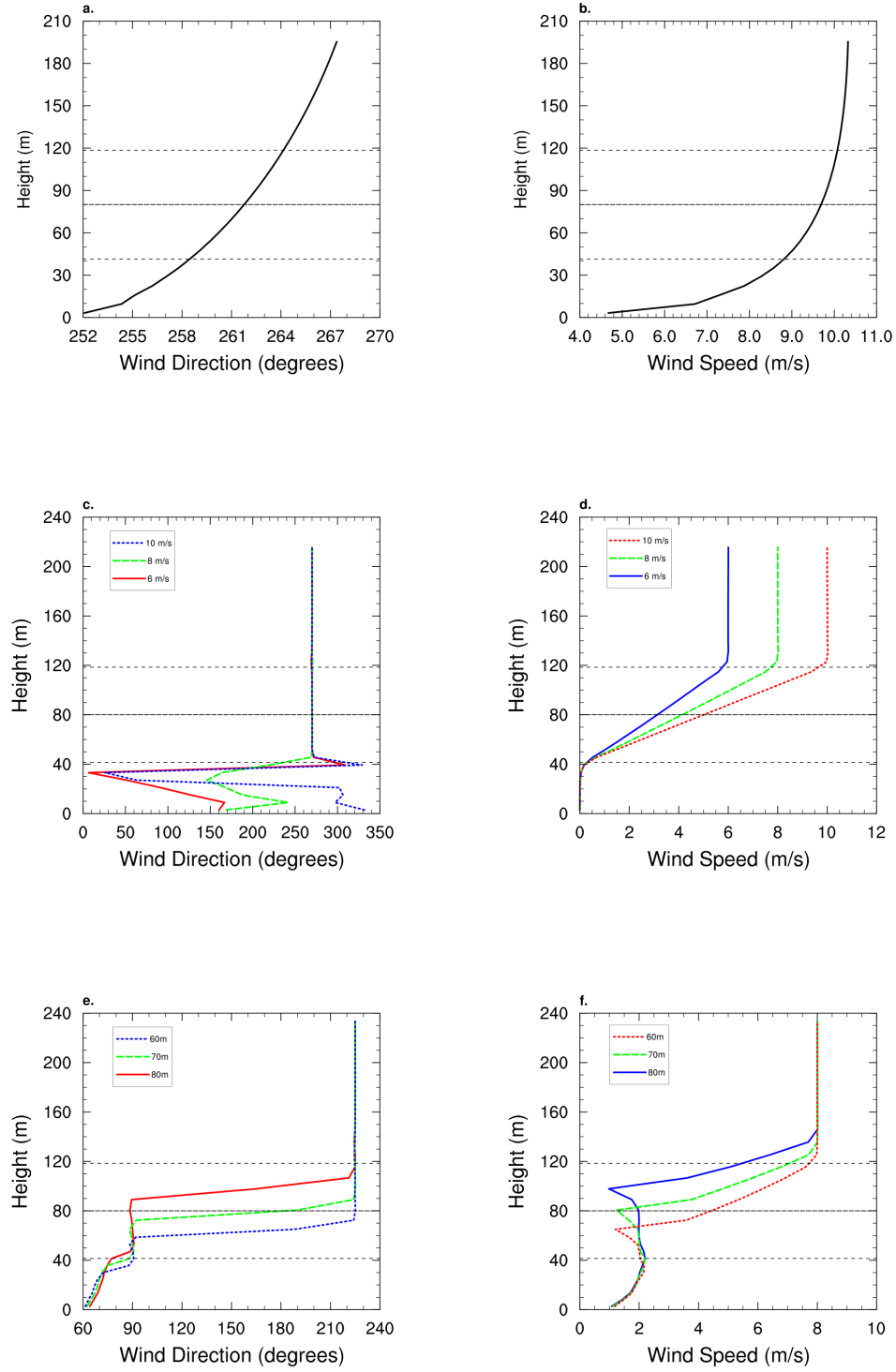


Figure 2.3: Post-spin-up wind direction and wind speeds for the neutral (a - b), stable (c - d), and mix-out (e - f) simulations.

	<b>F2012</b>	<b>Redfern et al., 2019</b>
Turbine	Repower 5M	Open-source GE SLE 1.5 MW
Temporal Averaging	6 hours	12 hours
Skin Surface Temperature	285 K	280 K
Surface Pressure	1000 hPa	1013 hPa
Inversion Location	Unknown	200 m
Eta Levels	Unknown	Figure 2.1
WRF Version	3.3	3.8.1
WFP Version	2011	2015
Nesting Configuration	Two-way	One-way

Table 2.2: Comparison between F2012 and Redfern et al., 2019

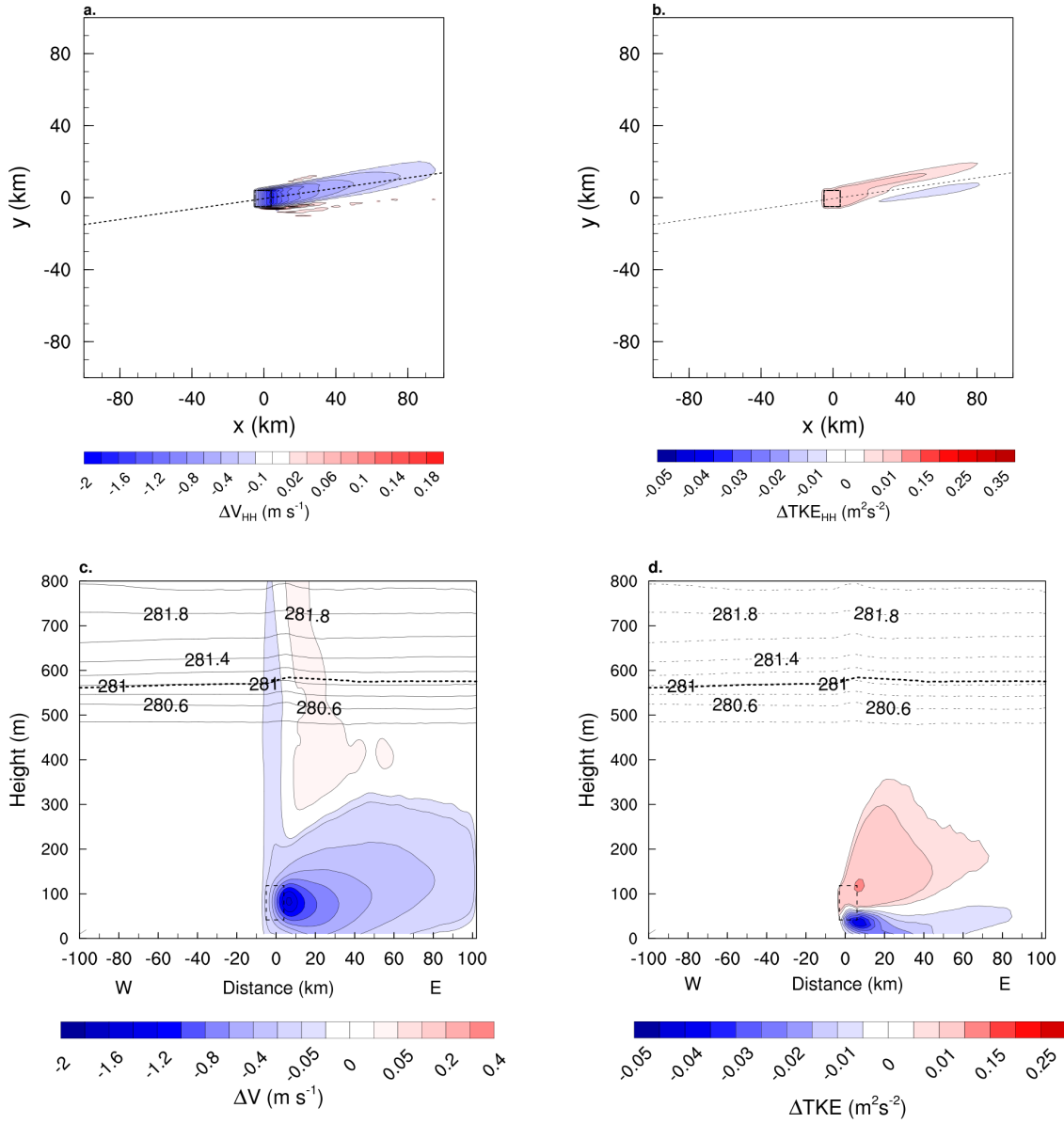


Figure 2.4: Horizontal cross-section of simulation domain taken at hub height showing the wake (a) and TKE generation (b). The black dashed outline indicates the wind farm. Vertical cross-section taken through the center of the wind farm, along the wind direction vector, showing the wake (c) and TKE generation (d). The black dashed outline indicates the wind farm, the gray lines show potential temperature, and the thick black dashed line is the top of the boundary layer.

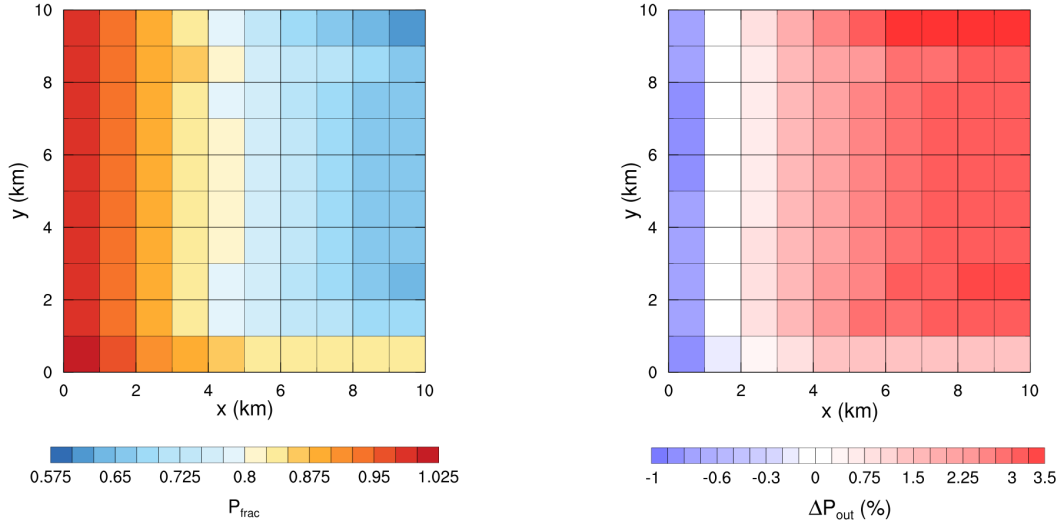


Figure 2.5: Fractional power output in each grid cell of the wind farm, defined as the temporal average of power output in the grid cell divided by the maximum power output of any grid cell over the simulation period (a). Percent difference in power output between the NF and NR simulations (b).

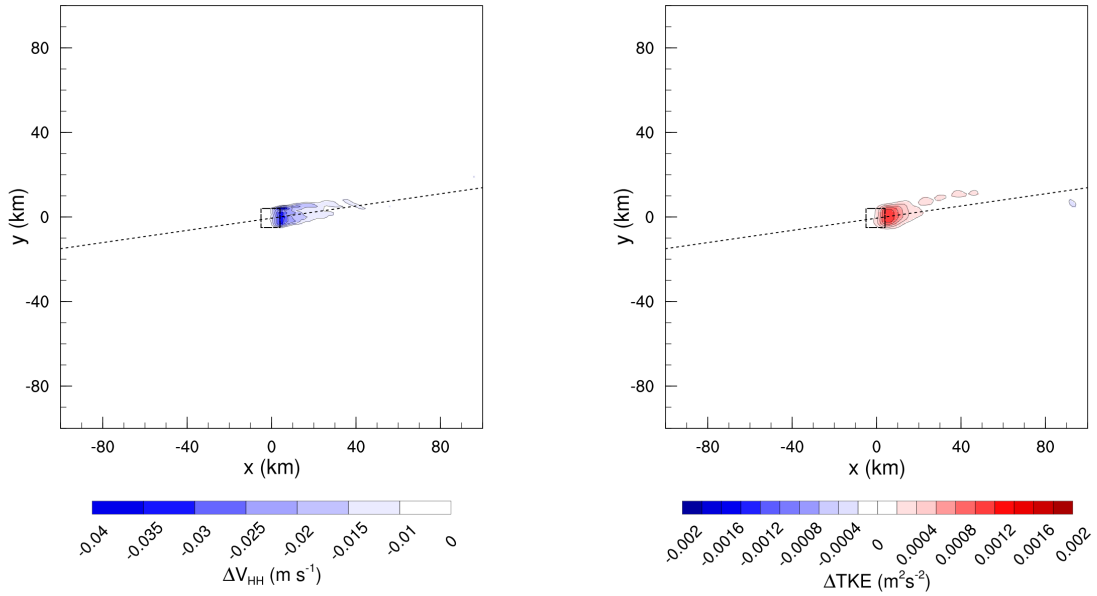


Figure 2.6: Difference between the waking (a) and TKE generation (b) in the NR and NF simulations. Negative values in (a) indicate a stronger wake, and positive values in (b) indicate greater TKE.



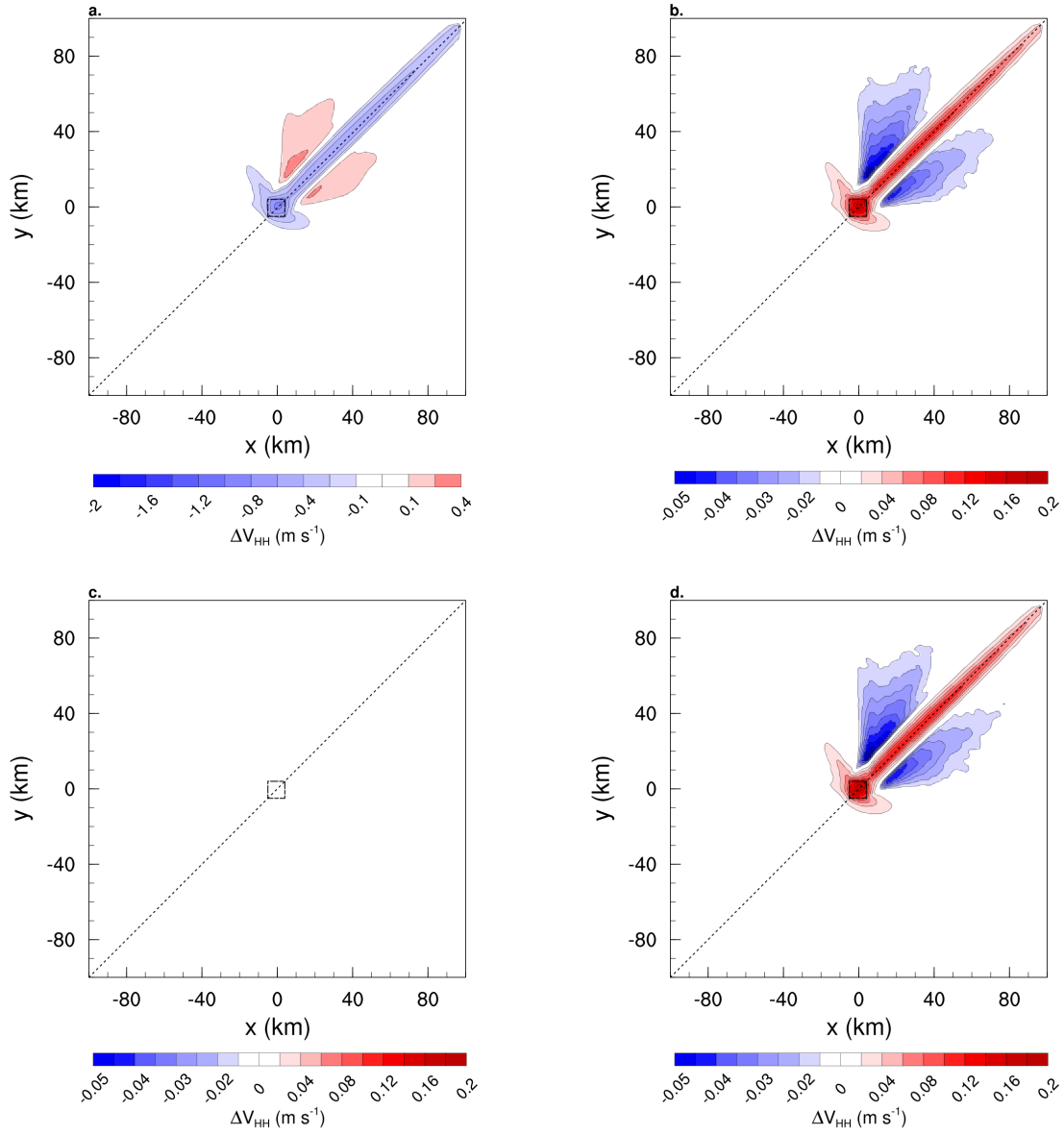


Figure 2.7: Waking and acceleration of winds in the MF\_60 simulation (a). Differences between the waking in MR\_60 (b), MV\_60 (c), MB\_60 (d) and MF\_60. Positive values in (b, c, d) indicate a weakening of the wake. Negative values along the flanks indicate a weakening of the acceleration on either side of the wake.

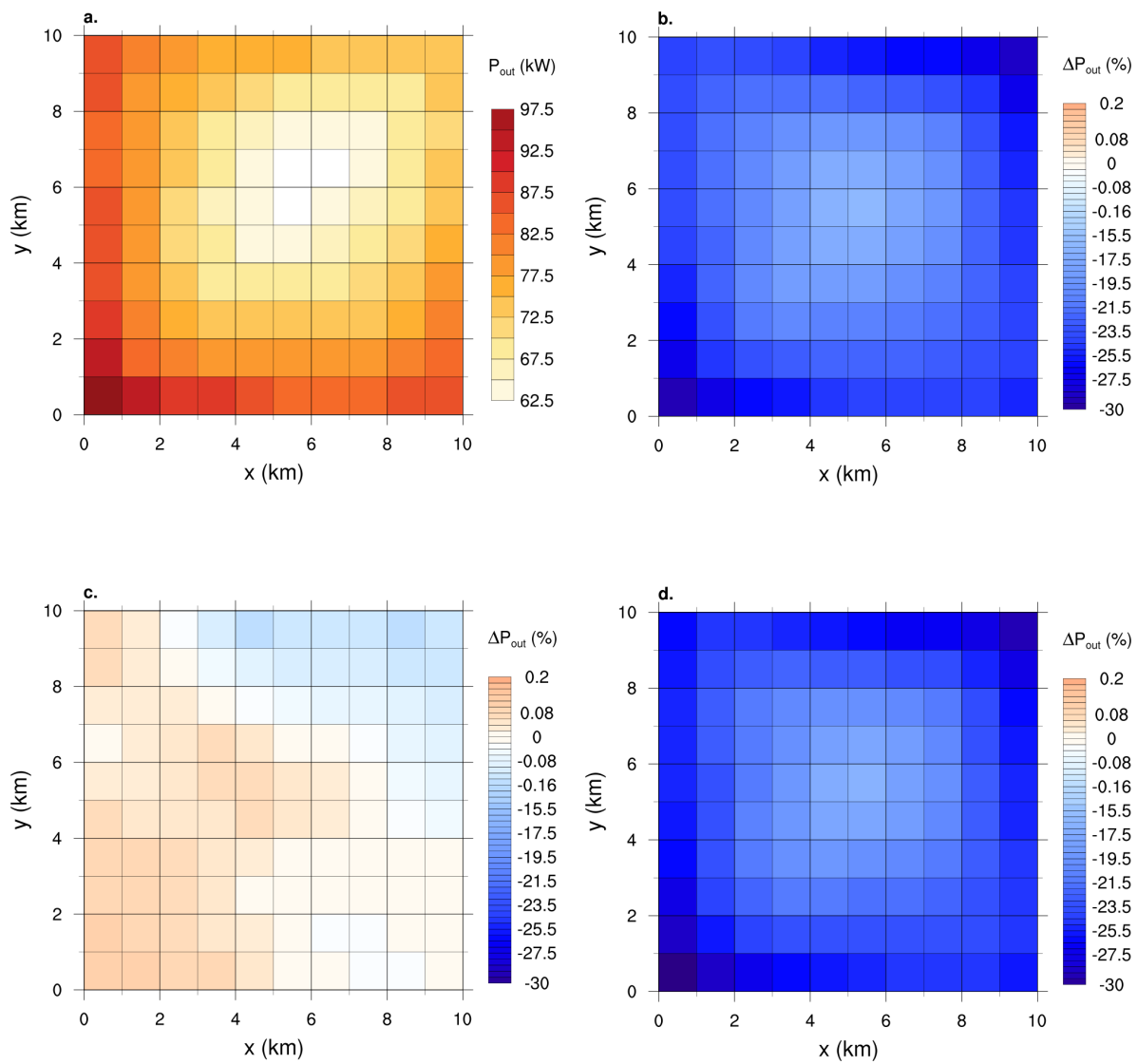


Figure 2.8: Power output for the MF\_60 simulation, in kW (a). Percent change in power output between MR\_60 (b), MV\_60 (c), MB\_60 (d) and MF\_60.

## Chapter 3

### Upper Atmosphere Smoke Injection from Large Areal Fires

#### 3.1 Preface

Understanding of large fire behavior has increased in importance as we face a drier world—one in which the fire season is expanding in both length and intensity (Flannigan, Stocks, & Wotton, 2000). Additionally, the revived nuclear threat adds to the urgency of extreme fire characterization. Whether a result of drought or nuclear war, large fires risk lofting great amounts of smoke into the upper troposphere and stratosphere. Such an event could have climatologic effects near and far; already, we have seen anomalies in stratospheric wind patterns after the 2019 Australian forest fires, and wildfire-driven stratospheric aerosol injection comparable to that of a small volcanic eruption (Peterson et al., 2018b; Kablick et al., 2020). If enough smoke rises above the tropopause, it could remain there for months to years.

By characterizing how large fires behave and how their plumes respond to local atmospheric conditions, we may be able to better predict pyroCu and pyroCb development, which could help inform evacuation notices and fire spread. Additionally, quantifying upper atmosphere aerosol injection is instrumental for policymakers needing to understand the full scope of possible outcomes from conflict engagement.

This chapter presents a modeling analysis of the sensitivity of plume behavior to the surrounding weather conditions. A series of simulations are run in an idealized WRF environment, with one atmospheric variable changed in each iteration. Through comparative analysis of the results, we corroborate and expand upon the findings of earlier studies: winds, stability, and humidity all influence smoke rise.

### 3.2 Abstract

Large fires can inject smoke into the upper troposphere and lower stratosphere. Detailed fire simulations allow for assessment of how local weather interacts with these fires and affects smoke lofting. In this study, we employ the fire simulation package in the Weather Research and Forecasting model (WRF-Fire), Version 4.0.1, to explore how smoke lofting from a fire burning a homogeneous fuel bed changes with varying local winds, relative humidity, and atmospheric boundary-layer stability for two different-sized areal fires. We find that the presence of moisture has the greatest influence on the results by raising the altitude of lofting, while faster winds speeds dampen lofting and lower the injection height. Stably stratified conditions further inhibit plume propagation compared with neutrally stratified conditions.

### 3.3 Introduction

Large fires have the potential to loft considerable amounts of smoke high in the atmosphere. If the fires burn intensely enough, their sensible heat flux can generate powerful convection (Luderer et al., 2006; Trentmann et al., 2006). Convection can also be enhanced by cloud formation if the atmosphere is humid. Aerosol byproducts of combustion can act as cloud condensation nuclei (CCNs), which can seed pyrocumulus (fire-derived clouds, or pyroCu) and pyrocumulonimbus (fire-derived storms, or pyroCb) development. PyroCb in particular can generate deep convection, which has the potential to inject smoke into the upper atmosphere and stratosphere. When aerosols are lofted, high-speed, upper-level winds can advect them to locations far from the fire source before they are removed from the atmosphere, and therefore they can affect climate elsewhere on a months-long timescale (M. Fromm et al., 2010a; Peterson, Hyer, & Wang, 2014; Peterson et al., 2018a; Yu et al., 2019).

The impact of smoke transport on climate has been a research topic for decades. In the late 20th century, Cold War tensions between the United States and the Soviet Union presented the risk of nuclear war. The 70,000 nuclear weapons then in existence exceeded the numbers of

military targets by orders of magnitude, so urban areas were almost certain to be targeted. In an early research study, Crutzen and Birks (1982) suggested that urban attacks might cause fires in surrounding forested regions, leading to very dense but short-lived smoke palls (Crutzen & Birks, 1982). Another early study—Turco, Toon, Ackerman, Pollack, and Sagan (1983a)—found that whole cities—with much larger fuel loads than forests—could be ignited, with powerful enough convection to loft combustion byproducts into the upper troposphere and stratosphere, where residence times could be on the order of years (Turco et al., 1983a). In a few weeks’ time, these aerosols would circle the planet and limit sunlight globally. As a result, following significant drops in temperature and ensuing crop failure, people would either freeze or starve to death. This outcome was given a name: nuclear winter (Turco et al., 1983a). Despite denuclearization efforts over the last forty years, nine nations still possess a total of 14,000 nuclear weapons, of which about 5000 are deployed (with the rest being dismantled) (SIPRI, 2019). This stockpile is enough to attack with more than 10 weapons each city with over 100,000 people in the U.S., Russia, and China (Kristensen, 2019; Arms Control Association, 2019). Nuclear winter, therefore, remains a risk.

More recent research has employed both global climate models (GCMs) and high-resolution models to assess these possible climate impacts, and they have by and large corroborated the findings of early studies (Covey et al., 1984; Cotton, 1985; Penner et al., 1986; Ghan et al., 1988; Robock, Oman, & Stenchikov, 2007; Robock, Oman, Stenchikov, Toon, et al., 2007; Toon et al., 2007; Robock & Toon, 2012a; Reisner et al., 2018; Coupe et al., 2019b). Most GCM-based studies are initialized with a certain amount of smoke loading at a specified injection height, based on the size and number of weapons considered. These altitudes are often informed by observations from mass fires, such as in Hamburg during the second world war, or by 1980’s simulations using mesoscale models that were driven by energy release rates (Penner et al., 1986; Small & Heikes, 1988; Turco, Toon, Ackerman, Pollack, & Sagan, 1990). Using this method, Robock, Oman, Stenchikov, Toon, et al. (2007), Toon et al. (2007), Toon, Robock, and Turco (2008), and Coupe et al. (2019b) found that, given an exchange with the strategic weapons allowed under treaties between the U.S. and Russia, a nuclear winter is a possible outcome. Further, the detonation of

100 Hiroshima-sized bombs in Pakistani and Indian urban areas could produce climate effects that endanger global agricultural productivity (L. Xia, Robock, Mills, Stenke, & Helfand, 2015; Toon et al., 2019; Jägermeyr et al., 2020). Only 1.5 megaton’s worth of explosives used on urban areas could cool global average temperatures by  $1.25^{\circ}\text{C}$  for several years and cause anomalously cold temperatures of  $0.5^{\circ}\text{C}$  for over a decade (Toon et al., 2019). In contrast to these findings, Reisner et al. (2018), using a low-fuel loading scenario of an estimated  $0.14\text{ g cm}^{-2}$  within the target area (Robock, Toon, & Bardeen, 2019) and  $0.91\text{ g cm}^{-2}$  across the entire domain, suggests that the risk of significant climate perturbations is small because the bulk of the smoke rising from urban targets will never ascend above the lower troposphere. This particular study used a fine-resolution model to simulate a detonation in the East Lake country club region of Atlanta (Robock, Toon, & Bardeen, 2019) to predict a smoke concentration profile, which was then applied in a global climate model to more generally assess the impacts of high-altitude smoke transport following a broader-scale nuclear exchange (Reisner et al., 2018). The fuel sources were based on satellite imagery of the region and idealized atmospheric conditions of  $6\text{ m s}^{-1}$  surface winds and a stable and dry atmosphere were used in the microscale model.

Some studies focused on local smoke lofting, rather than on global climatic effects, have indicated that weather plays a significant role in fire plume behavior, which affects how much smoke is injected in the upper atmosphere. PyroCu and pyroCb development is sensitive to local environmental moisture (M. Fromm et al., 2010a; Lareau & Clements, 2016; Peterson, Hyer, Campbell, Solbrig, & Fromm, 2016), and as previously mentioned, these phenomena can generate deep convection. Additionally, wind speeds determine whether or not a mass fire develops into a conflagration or a firestorm—the latter of which causes much deeper smoke lofting (Glasstone & Dolan, 1977; Cotton, 1985; Penner et al., 1986). In the context of climatic forcing by upper atmosphere aerosols, it is important, therefore, to have localized estimations of plume rise.

In this study, we use large-eddy simulations (LES) to simulate fire growth in a homogenous, wildland fuel bed to evaluate smoke lofting due to mass fire development, on time scales relevant to plume behavior. We quantify the sensitivity of this lofting to varying atmospheric conditions.

Two fire sizes are examined, informed by the presumed affected areas following a small-sized (15 kiloton) nuclear weapon air burst, which is consistent with the Hiroshima nuclear explosion, and a larger weapon (100 kiloton), which could be present in the Indian arsenal, since they exploded a weapon with a yield near 50 kt in 1998 (Wellerstein, 2012). The makeup of the fuel bed is less dense than what would be found in an urban setting, however. Fuel loading, at  $1.3 \text{ g cm}^{-2}$ , is an order of magnitude or more lower than what would be expected if the fire area consisted of buildings, refineries, and other similar targets. Consequently, this smoke sensitivity study primarily focuses on how local weather conditions affect plume rise. Longer-term radiatively-driven lofting, which has been seen in observations Yu et al. (2019) and climate models, is not considered.

The simulations and model setup are described in Section 3.4. In Section 3.5, we address the role of oxygen starvation, present our findings on how wind speeds, atmospheric moisture, and boundary-layer stability affect vertical smoke distributions, and compare several metrics to evaluate the comparative sensitivity of plume rise to winds and humidity. Finally, we provide a brief discussion and conclusions in Section 3.6.

### 3.4 Model Environment

The simulations use the Advanced Research Weather Research and Forecasting Model (WRF-ARW, henceforth referred to as WRF), Version 4.0.1 (W. C. Skamarock & Klemp, 2008; Powers et al., 2017). WRF is a numerical weather prediction model capable of simulating nested domains with outer boundaries specified either by coarser-scale models or reanalysis data, or by idealized conditions—the latter of which is useful for parameter sensitivity studies like this one. As an open-source model, WRF offers ease of accessibility and, therefore, simulation reproducibility. The model setup, explained below, is also summarized in Table 3.1.

WRF-Fire, the fire modeling parameterization in WRF, simulates the fire spread and heat release (latent and sensible) that results from a wildland fire. This heat release feeds back into the atmospheric component of WRF, influencing local meteorology. A passive smoke tracer option may be activated. WRF-Fire was first introduced in 2004 as an integration into WRF that coupled

the CAWFE tracer model with a level-set fire spread algorithm (Clark, Coen, & Latham, 2004; Patton & Coen, 2004a; Mandel, Beezley, & Kochanski, 2011a; Coen et al., 2013a). In this study, we use a more recent version of WRF-Fire, in which a level-set method, which is a mathematical algorithm used to track front propagation (Osher & Sethian, 1988), is used to determine the fire spread. This technique improves the accuracy of its fire-front tracking by incorporating high-order numerical schemes and solutions of an additional equation for level-set re-initializations (Muñoz Esparza, Kosović, Jiménez, & Coen, 2018; Jiménez, Muñoz Esparza, & Kosović, 2018).

### 3.4.1 Model Setup

As described in Table 3.1, the simulations include two domains: an outer mesoscale domain with periodic boundary conditions, acting as the reference flow, and a nested LES. The outer domain has a horizontal grid resolution of 1.1 km across a 200 x 200 km domain. The LES nest is centered inside the parent, with a horizontal grid resolution of 100 m and spanning a 19.8 km x 19.8 km domain. The vertical resolution for both domains is the same, with 80 levels stretched between the ground and the model top at 18 km. Due to the low model top, we assume a mid-latitude location with a tropopause at 12 km and a Coriolis parameter of  $10^{-4} \text{ s}^{-1}$  (Wilcox, Hoskins, & Shine, 2012). The fire mesh, a subgrid of the nested domain used with the fire spread algorithm, has a 25-m horizontal grid spacing. The fire is lit only in the nest, and feedback from the nest to the parent domain does not occur. The simulations automatically terminate when the fire reaches the edge of the LES domain, which could occur as quickly as 1.5 hours for the high wind speed simulations used in this study.

WRF physics and dynamics are simplified. The outer domain uses the Mellor-Yamada-Nakanishi-Niino (MYNN) PBL scheme (Nakanishi & Niino, 2009b). Since the nest is configured with LES resolution, no planetary boundary layer (PBL) scheme is required or specified in this domain. Both domains use Thompson graupel microphysics (Thompson, Rasmussen, & Manning, 2004a; Thompson, Field, Rasmussen, & Hall, 2008). The MYNN surface-layer scheme is used to account for near-surface heating impacts, but no land-surface parameterization is used. For



simulations incorporating radiative fluxes, the Rapid Radiation Transfer Model for the Korean Integrated Model (RRTMK) short- and longwave schemes are enabled (Baek, 2017). The model is initialized and run in a non-hydrostatic environment. A third-order Runge-Kutta time integration scheme is used, with a time step of 0.5 s in the outer domain. Eddy diffusion is handled by horizontal Smagorinsky first-order closure for the mesoscale domain, and by 1.5 order TKE closure for the LES nest. Moisture and scalar advection variables are calculated via a positive-definite scheme. Fifth-order horizontal and third-order vertical advection accuracy is used. To reduce the impact of gravity wave reflection within the domain, upper-level Rayleigh damping with a coefficient of  $0.2 \text{ s}^{-1}$  is employed within a depth of 5 km from the model top (Klemp et al., 2008). This damping layer is not expected to affect smoke lofting within the vertical range of interest in this study.

### 3.4.2 Simulations Overview

We vary geostrophic wind speed and wind shear, atmospheric moisture, boundary-layer stability, and ignition area in sixteen different simulations to evaluate how meteorological variables influence the smoke distribution generated from two different-sized mass fires. In all cases, the outer domain is initialized and run (spun up) for four hours to achieve equilibrium from the initial condition, after which the interior domain is initialized and run for either 4 or 6 hours, depending on turbulence generation in the nested domain, before the fire is lit. The cell perturbation method (Muñoz Esparza & Kosović, 2018) is used to generate TKE in the nest, and Figure 3.1 shows the thermal and wind profiles for that domain in each subset of simulations after they have spun up. Once the domains have been spun up, a fire is ignited in the center of the inner domain and burns for 90 minutes. Output from this final segment of the simulations is what we have evaluated in this study.

Soundings for the four moist profiles, of which only MR\_75 develops any convective available potential energy (CAPE) after spinup, are presented in Figure 3.2. CAPE is a measurement of a parcel’s potential energy for rise after it reaches the free troposphere, and it is generally used as a metric for the development of deep convection (Moncrieff & Miller, 1976; Fritsch & Chappell,

1980). Before ignition, MR\_75 has an average CAPE value of  $41.26 \text{ J kg}^{-1}$ .

The base case for each fire size is a low-wind scenario with constant  $2.5 \text{ m s}^{-1}$  geostrophic winds throughout the domain, no radiation, a dry atmosphere, and a neutrally stratified, 2-km deep boundary layer capped by a stable layer extending through the troposphere (Fig. 3.1b,d,f). The other cases are divided into subsets based on variations in boundary-layer stability (Stable, with  $\frac{d\theta}{dz} = 6 \text{ K km}^{-1}$  from the top of the boundary layer to the tropopause), winds (Calm, MidWi, HiWi, Shear), or moisture and radiation (M50, MR25, MR50, MR75). Specifications for each simulation can be found in Table 3.2. All background winds are applied as geostrophic forcings acting from the ground to the top of the atmosphere. All cases have the same stable thermal profiles above the boundary layer ( $\frac{d\theta}{dz} = 6 \text{ K km}^{-1}$  to the tropopause, and  $\frac{d\theta}{dz} = 15 \text{ K km}^{-1}$  above that). A small amount of fuel moisture (defined as 8% of the fuel content) is released into the atmosphere upon ignition in all cases.

Following spinup, either a 2-km radius or 4-km radius fire is ignited in the center of the nest, both lit areally. For all cases, the fire burns for the same amount of time—1.5 hours. In the high-wind case, the fire reaches the domain edge at this point, so the other cases are terminated at the same time to facilitate comparison.

### 3.4.3 Fuel Source

A nuclear weapons strike would cause an areal ignition. Key military bases, population-dense cities, or other strategic and anthropogenically-developed locations—all having dense fuel loads—would be likely targets. Observations from World War II, during which over 60 fires were started by incendiary bombing, suggest that firestorms, which generate strong enough convection to loft a great amount of smoke into the upper atmosphere, can develop when the fuel loading exceeds  $4 \text{ g cm}^{-2}$  (Glasstone & Dolan, 1977). For our simulations, we use heavy logging slash as the fuel bed, which has a smaller loading of  $1.3 \text{ g cm}^{-2}$ . WRF-Fire has been developed as a wildland fire parameterization, so it offers 13 fuel sources as defined by the Anderson 13 Standard fuel categories (Anderson, 1982a). Heavy logging slash is the densest option available. A previous

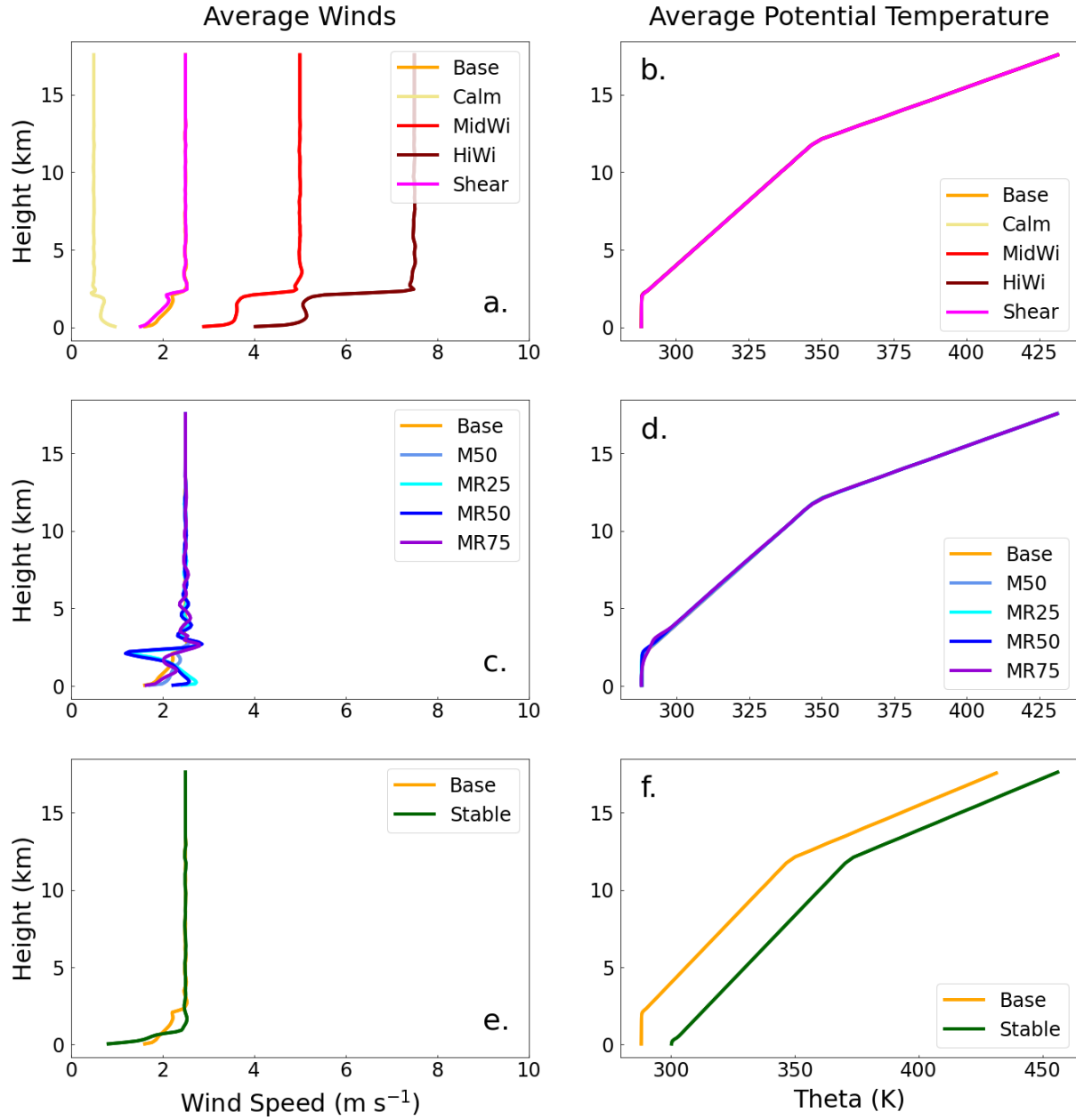


Figure 3.1: Domain-averaged winds in the nest after spin-up for the winds subset (a), moisture subset (c), and stability subset (e). Thermal profiles after spin-up for the winds subset (b), moisture subset (d), and stability subset (f).

study simulating the Hamburg firestorm of WWII used a fuel loading of about  $2.6 \text{ g cm}^{-2}$  (Penner et al., 1986)—about two times as large as ours. Therefore, our simulations may most directly represent forest fire pyroconvection, which can occur in situations with wildland fuel loading (Luderer et al., 2006; Trentmann et al., 2006; M. Fromm et al., 2010a; Peterson, Hyer, et al., 2016). The  $1.3 \text{ g}$

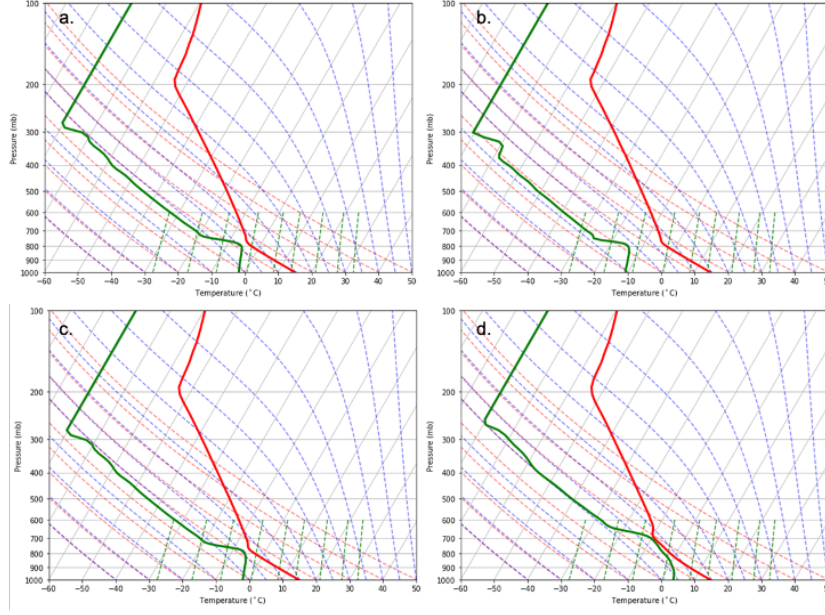


Figure 3.2: Post-spinup soundings for the four moist cases: M50 (a), MR25 (b), MR50 (c), and MR75 (d). Green indicates the dew point temperature profiles, while red indicates the environmental temperature profiles.

$\text{cm}^{-2}$  of fuel is also similar to the fuel load assumed by Reisner et al. (2018) of  $0.91 \text{ g cm}^{-2}$  (Robock, Toon, Bardeen, Xia, et al., 2019).

WRF-Fire considers the fuel source to be 100% combustible, with 2% of it forming PM<sub>2.5</sub> smoke, which then is transported through the domain as a passive tracer. To calculate the smoke profile, all smoke that has exited the domain must be accounted for. An estimate of total smoke (in and out of the domain) at each height can be calculated by assuming that all smoke at the edges of the domain will exit by the next output write time. This time interval has been selected independently for each simulation to minimize error between the smoke generated (an aggregate model variable that updates each time step) and the estimated smoke presence. For the final smoke profile, the smoke is assumed to remain fixed in the vertical after it exits the domain. To calculate the error at each vertical level, the percentage difference between the total smoke generated and the total calculated smoke in (and exited from) the domain is multiplied through the values at each height. This difference is less than 5% for all cases.

### 3.4.4 Model Uncertainty

WRF-Fire is under ongoing development; therefore, it has some limitations that could lead to either under-estimation or over-estimation of smoke profile concentrations. As the smoke is a passive tracer, it does not seed cloud development, nor is smoke scavenged out of the atmosphere via rainfall (both factors leading to overestimation of smoke). Oxygen starvation, which would limit fuel burned or prolong the period of burning, is not considered but is discussed in Section 3.5.1 (overestimation). Lightning, which could spark new ignitions, is not simulated (leading to an underestimation of burn area and, therefore, smoke). The wildland fuel density used here is lower than that of urban fuels (underestimation), but the fuel bed is being modeled as continuous, without breaks in the source (overestimation). The fuel burns quicker than urban fuels, leading to an initial burst of heat release and initial lofting, followed by a tapering once the ignition area has burned out, which does not mirror what has been modeled in past studies focused on nuclear winter (underestimation). The fire parameterization has been developed for perimeter and point fires, not areal ignitions as is prescribed in this study (unsure of the consequences). Long-range fire spotting, otherwise known as branding and a method of fire propagation (Tarifa, Notario, & Moreno, 1965; Koo, Pagni, Weise, & Woycheese, 2010), is not currently supported by the model (underestimation). Finally, smoke does not interact with radiation to enable self-lofting behavior (underestimation of lofting and residence time) (Robock, Oman, Stenchikov, Toon, et al., 2007; Mills, Toon, Turco, Kinnison, & Garcia, 2008; Yu et al., 2019). All of these elements of uncertainty must be taken into consideration when examining the results of these simulations.

## 3.5 Results

The amount of smoke injected into the upper troposphere and lower stratosphere determines the amount of smoke that may ultimately rise above the tropopause, given enough time and radiative heating. Although not considered here, this process can be simulated in climate models, as shown in Toon et al. (2019), where smoke injected between 3.5 and 7 km below the tropopause

ultimately ascended into the stratosphere. To assess the impacts of local meteorological conditions on smoke transport into the upper atmosphere, we quantify the vertical smoke profile (integrated over the x-y plane to yield  $\text{Mg m}^{-1}$  of altitude). First, however, we present an analysis of potential oxygen starvation in the model. Following that is the smoke profile analysis, and finally we address some metrics—vertical velocity, CAPE, and horizontal wind speeds—that may be used at the time of combustion to ascertain how high the plume could rise.

### 3.5.1 Oxygen Starvation in the Model

One point of concern in modeling large fires is the overlooked potential for oxygen starvation. For combustion to occur, a fuel source, a heat source, and oxygen must all be present. Once the amount of oxygen in air drops below 16%, however, fires can no longer be sustained. Models that do not incorporate chemistry interactions, including WRF-Fire, typically do not consider the potential for oxygen depletion. Therefore, particularly intense, simulated fires may not be physically viable. The initial amount of oxygen in a grid cell with an active fire, combined with the convergence of surrounding air into the fire center, must be large enough to support the heat release and burn rate being calculated.

To check for oxygen starvation, the mass of oxygen initially present in the lowest two grid cells (ground to 200m) is first calculated according to Equation 1, with an assumed simplified air composition of 79% nitrogen ( $F_{N_2}$ ) and 21% oxygen ( $F_{O_2}$ ) by volume. The molar mass of  $O_2$  is  $32 \text{ g mol}^{-1}$  ( $M_{O_2}$ ) and the molar mass of  $N_2$  is  $28 \text{ g mol}^{-1}$  ( $M_{N_2}$ ). Air pressure ( $P$ ) is given in units of Pa. Each element of the equation is given at the grid cell on the fire mesh with the location  $(i, j)$  at time  $t$ .

$$O_{2,present,ijt} = \left(\frac{dP_{ijt}}{g}\right)(dx_{ij})(dy_{ij}) \frac{1}{(M_{O_2})(F_{O_2}) + (M_{N_2})(F_{N_2})} M_{O_2} F_{O_2} \quad (3.1)$$

The combustion of oxygen is a function of heat release rate. Both Thornton (1917) and Huggett (1980) found an average heat release rate ( $HRR_{avg}$ ) of  $13.1 \text{ MJ kgO}_2^{-1}$  for the burning of organic

solids. This constant is used to determine the amount of oxygen consumed in accordance with the fire's heat release rate. The oxygen depletion over time is calculated using linear interpolation between heat release rates on 1-minute outputs, with a time step ( $\Delta t$ ) of 0.1 s. The consumption of oxygen per time step is calculated in Equation 2.  $HRR_{ij}$ , the heat release rate in each ignited grid cell, is given in  $\text{W m}^{-2}$ . The variables  $dx_{ij}$  and  $dy_{ij}$  refer to each cell's extent in the x and y directions.

$$O_{2,cons,ijt} = \sum_{n=0}^{(\Delta t * 600s) - 1} \frac{1}{HRR_{avg}} (dx_{ij})(dy_{ij})(\Delta t) \left( (HRR_{ij,t+1} - HRR_{ijt}) \left( \frac{n}{\Delta t * 600s} \right) + HRR_{ijt} \right) \quad (3.2)$$

The oxygen consumed by combustion is subtracted from the oxygen originally present in the cell each time step, resulting in a cumulative depletion of oxygen. Replenishment of air via inflow to the area is not considered in Equation 2; however, oxygen is assumed to be consumed during this time within a 200-m deep layer.

The most intense heat release occurs during the areal ignition of the fires. The fire spreads quickly inward from the outer perimeter, and once the ignition area has been completely burned, what remains is a perimeter fire with a much lower HRR. This process of bulk, rapid fuel consumption takes about four minutes for the 2-km radius fires, and about seven minutes for the 4-km radius fires (Figure 3.3). The greatest oxygen consumption occurs during this time.

Assuming a well-mixed boundary layer during and following ignition, we can infer a 30-minute turnover time in the vertical for the lowest 2 km of the model. Therefore, we have only plotted oxygen depletion for this time period in Figure 3.3 and assume that turnover following the initial ignition will suffice to maintain burning in what eventually becomes, for all cases, a perimeter fire.  $\text{O}_2$  levels drop to just below 16%, the amount necessary for sustained burning, by minute 30. However, by looking at a cross-sectional plot of winds during this time (Fig. 3.4), we see that  $\text{O}_2$  is in fact replenished by horizontal flow into the burn area, at velocities of up to  $15 \text{ m s}^{-1}$ . With

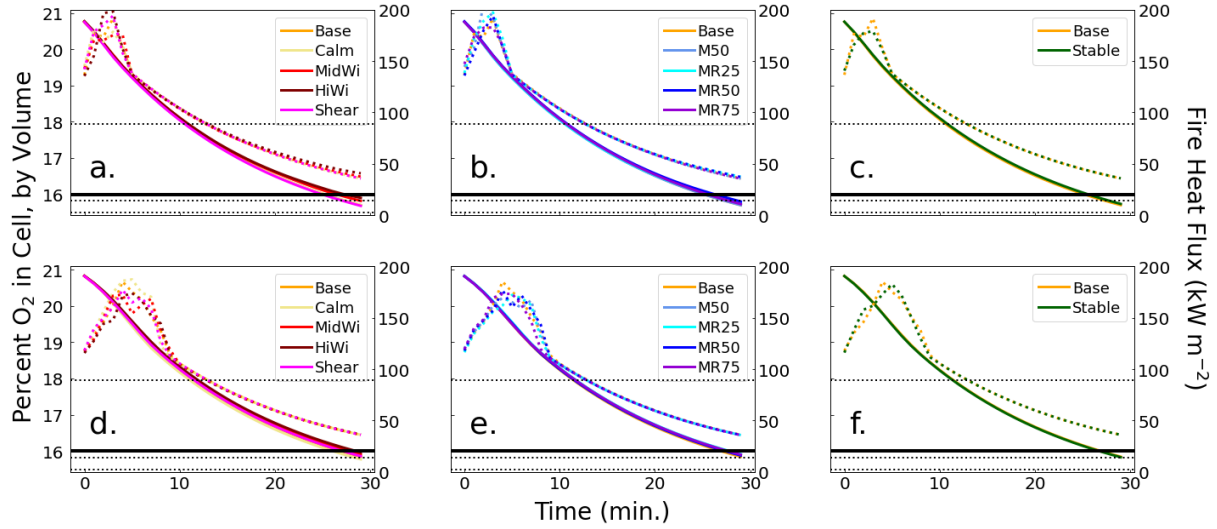


Figure 3.3: **Top:** Average oxygen depletion in the lowest 200 m of the model across burned area, assuming no air replenishment (left axis, solid), and heat release rate ( $\text{kW m}^{-2}$ ), right axis, dotted) for the 2-km ignition radius fires, grouped by simulation subset (a: Winds, b: Moisture, c: ABL Stability). **Bottom:** Average oxygen depletion in the lowest 200 m of the model across burned area, assuming no air replenishment (left axis, solid), and heat release rate ( $\text{kW m}^{-2}$ ), right axis, dotted) for the 4-km ignition radius fires, grouped by simulation subset (d: Winds, e: Moisture, f: ABL Stability). The heat release rates for each of Penner et al. (1986)'s three fire simulations are marked in each plot by horizontal dotted lines ( $\text{HRR} = 2.2 \text{ kW m}^{-2}$ ,  $14 \text{ kW m}^{-2}$ ,  $89 \text{ kW m}^{-2}$ ). The 16% depletion threshold is depicted via a thick horizontal line on each plot.

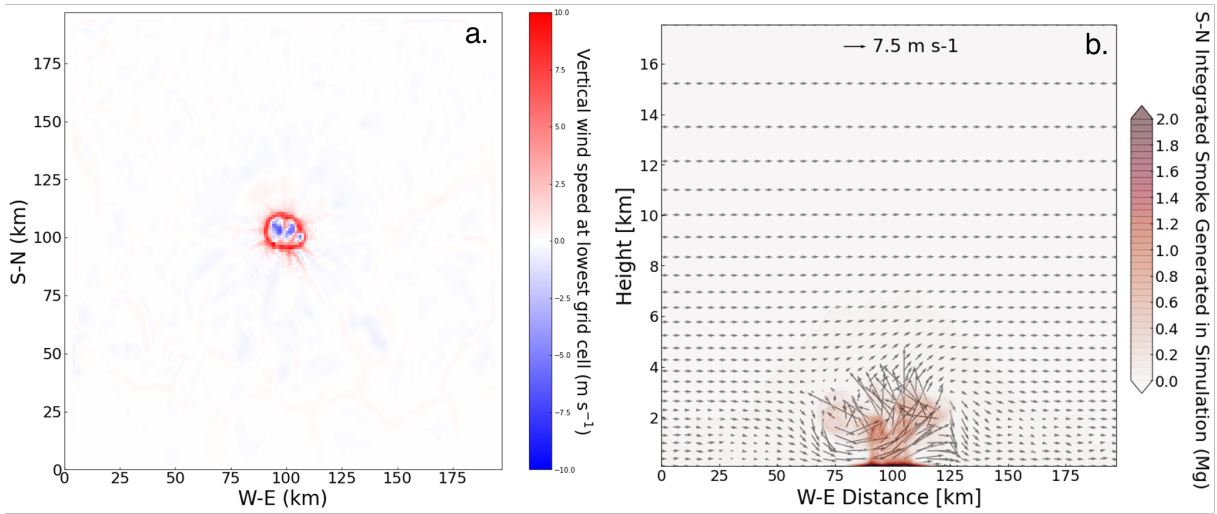


Figure 3.4: Left: Planar view of vertical velocities for Base\_2 at Right: Average oxygen depletion per grid cell across burned area (solid), assuming no air replenishment, and heat release rate ( $\text{W m}^{-2}$ , right axis, dotted) for the 4-km ignition radius fires, grouped by simulation subset (Top: Winds, Middle: Moisture, Bottom: ABL Stability).



this inflow and considering a full vertical turnover of air in the boundary layer after 30 minutes, oxygen starvation will not be a factor limiting fuel burn.

### **3.5.2 Smoke Lofting**

Quantification of how meteorology affects the depth of smoke lofting can help better inform assessments of pyrocumulus risk in fire forecasting models and the radiative impacts of large fires in climate models. Therefore, the primary interest of this study is evaluating the sensitivity of smoke lofting to local weather conditions. Here, we examine how varying wind speeds, boundary-layer stability, and moisture affect the immediate rise, or injection height, of smoke into the upper atmosphere. We find that in general, higher wind speeds dampen lofting by dispersing smoke horizontally higher up where the convection column weakens, moisture enhances plume rise due to latent heat release, and a neutral boundary layer provides better thermal conditions for deeper ascension than a stable boundary layer. The quantity of smoke that reaches the upper atmosphere in each simulation is presented in Table 3.3 for the 2-km radius fires and Table 3.4 for the 4-km radius fires.

#### **3.5.2.1 Wind Speeds**

Previous studies suggest that wind speeds will affect whether a mass fire develops only as a conflagration, which spreads quickly downwind, or a firestorm, which remains relatively stationary. A firestorm exhibits inward flow of near-surface air from every radial point towards its center; it will generate its own wind systems (Countryman, 1964; Morton, 1964). Firestorms are more likely to consume all the fuel in the ignition area and loft it to higher altitudes than conflagrations. One observational study from WWII suggests that an ambient wind speed of 8 mph, or roughly  $3.6 \text{ m s}^{-1}$ , is the tipping point between conflagration and firestorm development (Rodden, John, & Laurino, 1965). Slower winds favor the firestorm, while faster speeds favor a conflagration. Due to our lower fuel loading, we do not see development of a firestorm in our Base and Calm cases. We do not see winds flowing into the fires center from all radial directions, even during ignition.

In four simulations for each ignition radius, we vary the geostrophic wind speed, which is kept constant throughout the domain, between  $0.5 \text{ m s}^{-1}$  and  $7.25 \text{ m s}^{-1}$ . We also evaluate one slight wind shear case for each ignition size, with speeds increasing from  $0 \text{ m s}^{-1}$  to  $2.5 \text{ m s}^{-1}$  in the boundary layer, above which winds are held constant at  $2.5 \text{ m s}^{-1}$ . There is no specified wind directional shear, except for that which arises due to the Coriolis force (with a Coriolis parameter assumed to be  $10^{-4} \text{ s}^{-1}$  for a mid-latitude location) and frictional forces.

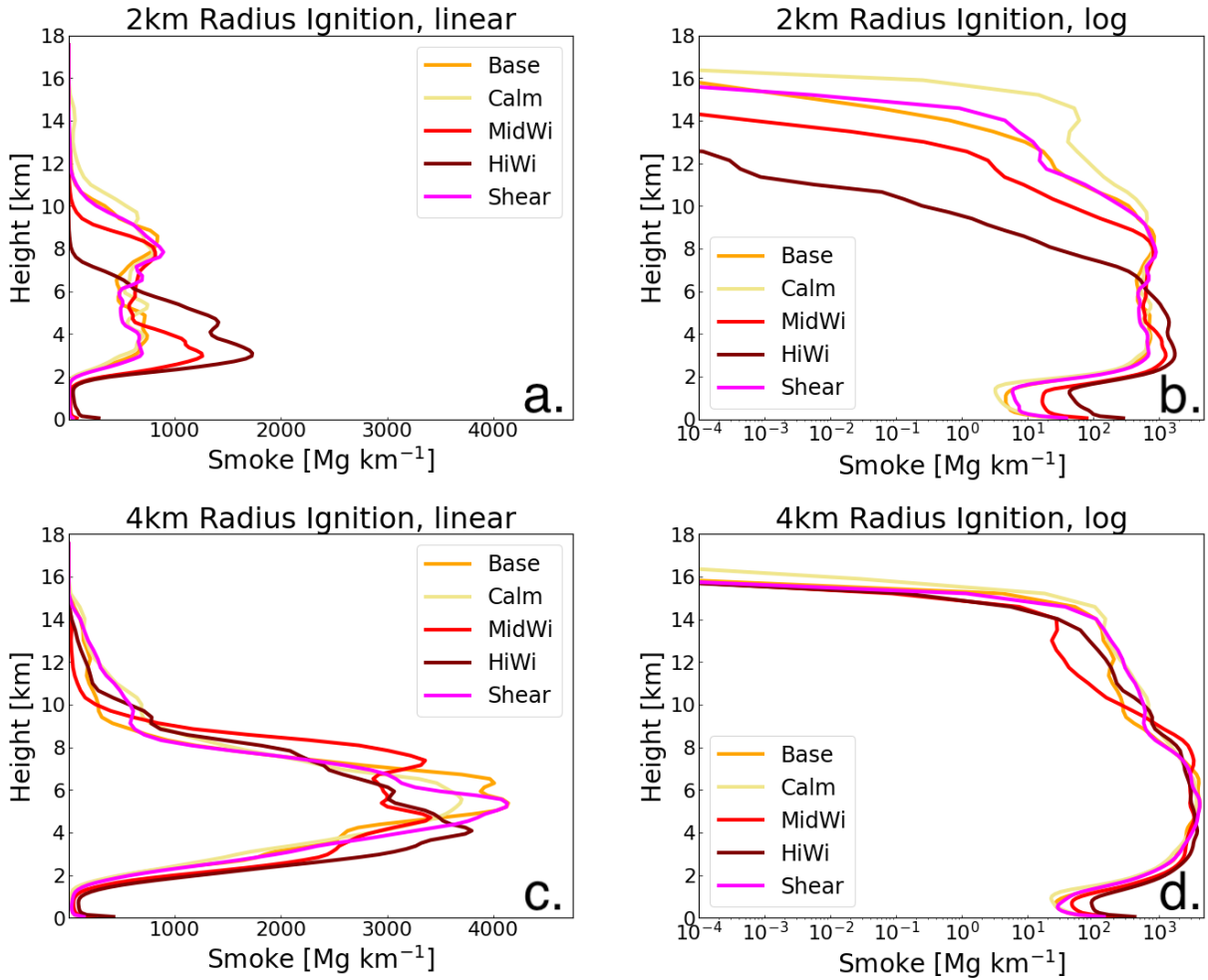


Figure 3.5: Final profiles of vertical smoke distribution (in  $\text{Mg km}^{-1}$ ) for the wind simulations after 1.5 hours of burning. Linear plots (a,c) and logarithmic plots (b,d), for the 2km radius (a,b) and 4km radius (c,d) ignitions are shown.

## 2-km Radius Fire

In this set of simulations, the vertical smoke profiles in the 2-km radius fire 1.5 hr after fire initiation demonstrate the impact wind speeds have on lofting (Fig. 3.5a,b). The largest amount of smoke generation occurs in HiWi\_2, as the faster winds cause the fire to spread more rapidly over the course of 1.5 hours, therefore burning a larger swath of land (5.65% of the domain, compared with 3.2% in CalmWi\_2). However, this case also results in a negligible amount of lofting into the stratosphere and the smallest amount of smoke reaching the upper atmosphere, as strong horizontal winds prevent deep vertical motion (Figure 3.6). Similarly, MidWi\_2 features a nominal amount of smoke reaching beyond tropopause and a small, although not negligible, amount extending above 9 km. Conversely, the weaker wind simulations result in a greater amount of upper atmospheric smoke presence (Fig. 3.5a,b). In CalmWi\_2, 15% of the total smoke generated rises above 9 km; Base\_2, with  $2.5 \text{ m s}^{-1}$  winds, allows 9.25% of total smoke to rise this high (Table 3.3). The addition of a small amount of wind speed shear in the boundary layer, as compared with Base\_2, has a slight impact on lofting; smoke above 9 km is reduced, and smoke above the tropopause remains roughly the same.

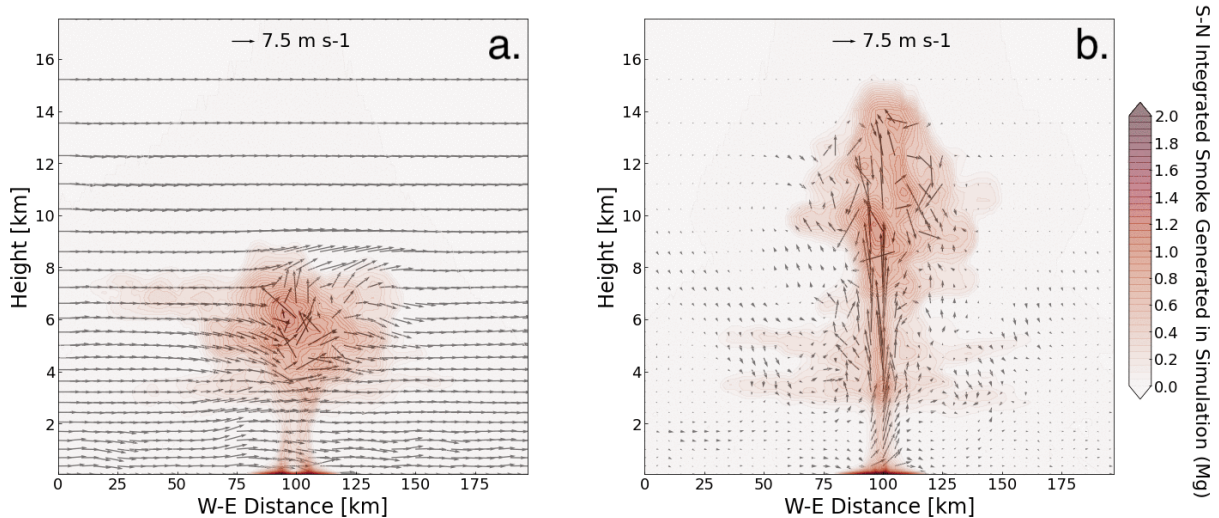


Figure 3.6: Cross-sectional winds taken from a W-E transect through the domain center, with integrated smoke (colored contours), for HiWi\_2 (a) and CalmWi\_2 (b). Stronger horizontal winds in HiWi\_2 dampen the convective lofting of smoke.

### 4-km Radius Fire

All cases in the 4-km wind variability simulations result in a greater amount of smoke reaching the upper atmosphere than in the 2-km radius fire, as the increased surface heat flux from the larger ignition area results in stronger convection. As with the 2-km radius fire, the smallest amount of smoke generation and the largest amount of upper atmosphere smoke injection for this subset occurs in the quiescent case (CalmWi\_4). However, compared with the 2-km radius fire, a smaller percentage of total smoke production reaches the upper atmosphere—6.13%, as compared with 15.03%. Despite a 400% increase in the ignition area of the larger fire, the total amount of smoke reaching the upper troposphere and stratosphere increases by 275.1 kg, or only 154%. Additionally, the percent smoke reaching the stratosphere decreases by 0.2%, despite an overall increase in total smoke above the tropopause of 86.3 kg, or nearly doubling (Table 3.4).

The higher wind speed cases—MidWi\_4 and HiWi\_4—both see an increase in percent smoke rise into the upper troposphere and stratosphere with the larger ignition area. HiWi\_4 in particular returns in a greater amount of upper troposphere plume presence when compared with the 2-km radius simulation. Presumably the stronger convection resulting from the larger ignition area provides enough energy to inject more smoke above the inversion at the tropopause. Additionally, the rapid increase in area burned by HiWi\_4 compared with MidWi\_4 contributes to a significantly larger amount of smoke generation, as well as a rise in the fire’s heat release rate. As a result, HiWi\_4 has a bigger gain in smoke lofting (Fig. 3.5).

#### 3.5.2.2 Moisture and Radiation

The inclusion of moisture and a radiation scheme in the model is important for a realistic simulation. Evaluating the impact of water vapor can provide insight into how significant a role it plays in smoke lofting. The ignition of vegetation releases moisture that can contribute to cloud formation, but the addition of water vapor introduces the potential for pyrocumulonimbus formation, which has been shown to inject smoke into the stratosphere (M. Fromm et al., 2010a).

In three simulations for each ignition radius, moisture is varied among a constant 25% (MR25), 50% (M50, MR50), and 75% (MR75) relative humidity uniformly throughout the domain, with the RRTMK radiation parameterization enabled. Of note is that the global average humidity in the boundary layer is around 75%. In addition to these simulations, another case with 50% relative humidity is run without any radiation considered. These simulations are compared alongside the base case, which is dry and does not include radiative effects (Fig. 3.7). All simulations have constant  $2.5 \text{ m s}^{-1}$  winds throughout the domain and a thermal profile mirroring that of the base scenario.

## 2-km Radius Fire

In general, adding moisture into the atmosphere enhances air parcel ascent, as that moisture releases latent heat when it rises and condenses. If cloud droplets rise high enough, they freeze into ice—a process that also releases heat. When radiation is considered, a slightly cooler troposphere, as compared with the M50 cases, develops during spinup. Because of this, we see deeper convection for MR50\_2 once the fire is lit, leading to a greater amount of precipitation (here, precipitation is the combination of rain and graupel). Since our passive smoke tracer follows the dynamics of the atmosphere, smoke follows the precipitation out of the upper troposphere, leading to a reduced amount of smoke above 9km and above 12km by the simulations' end (Fig. 3.8a). Similarly, we see a smaller smoke injection above 9km and 12km for MR25\_2 compared with Base\_2. This occurs, again, due to the effects on smoke by precipitation. Base\_2 sees no precipitation development, whereas MR25\_2 does, and as a result a greater amount of smoke exits the upper troposphere and stratosphere in MR25\_2, as compared with Base\_2 (Fig. 3.8b).

M50\_2 lofts over 20% of its smoke production into the upper troposphere, while MR50\_2 injects only 14.8% that high. Similarly, Base\_2 results in a 9.25% plume rise above 9 km, while MR25\_2 only convects 7.2% to that level. Still, when comparing all the cases using a radiation scheme, an increase in background humidity results in an increase in the amount of smoke reaching

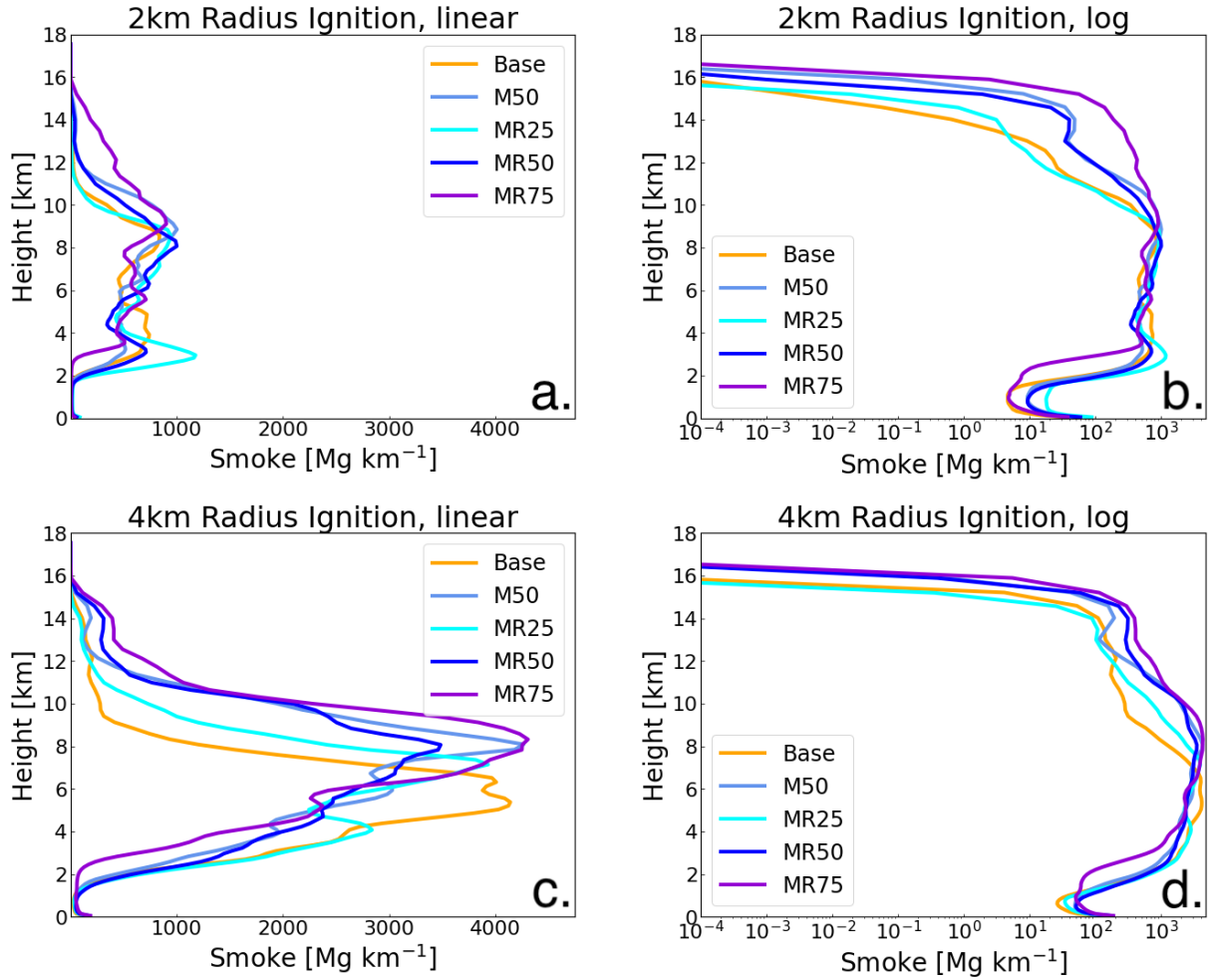


Figure 3.7: Final profiles of vertical smoke distribution (in  $\text{Mg km}^{-1}$ ) for the moist simulations after 1.5 hours of burning. Linear plots (a,c) and logarithmic plots (b,d), for the 2km radius (a,b) and 4km radius (c,d) ignitions are shown.

the upper troposphere. MR75\_2 sees the greatest amount of smoke lofting of all the 2-km radius ignition simulations, with over 30% extending above 9 km and 6.9% rising into the stratosphere (Table 3.3, Fig. 3.7a,b).

#### 4-km Radius Fire

When the fire radius is increased to 4 km, the precipitation difference between MR50\_4 and M50\_4 is smaller than that between MR50\_2 and M50\_2 (Fig. 3.8). As a result of this precipitation difference and the deeper convection with radiation, MR50\_4 injects a greater amount of smoke

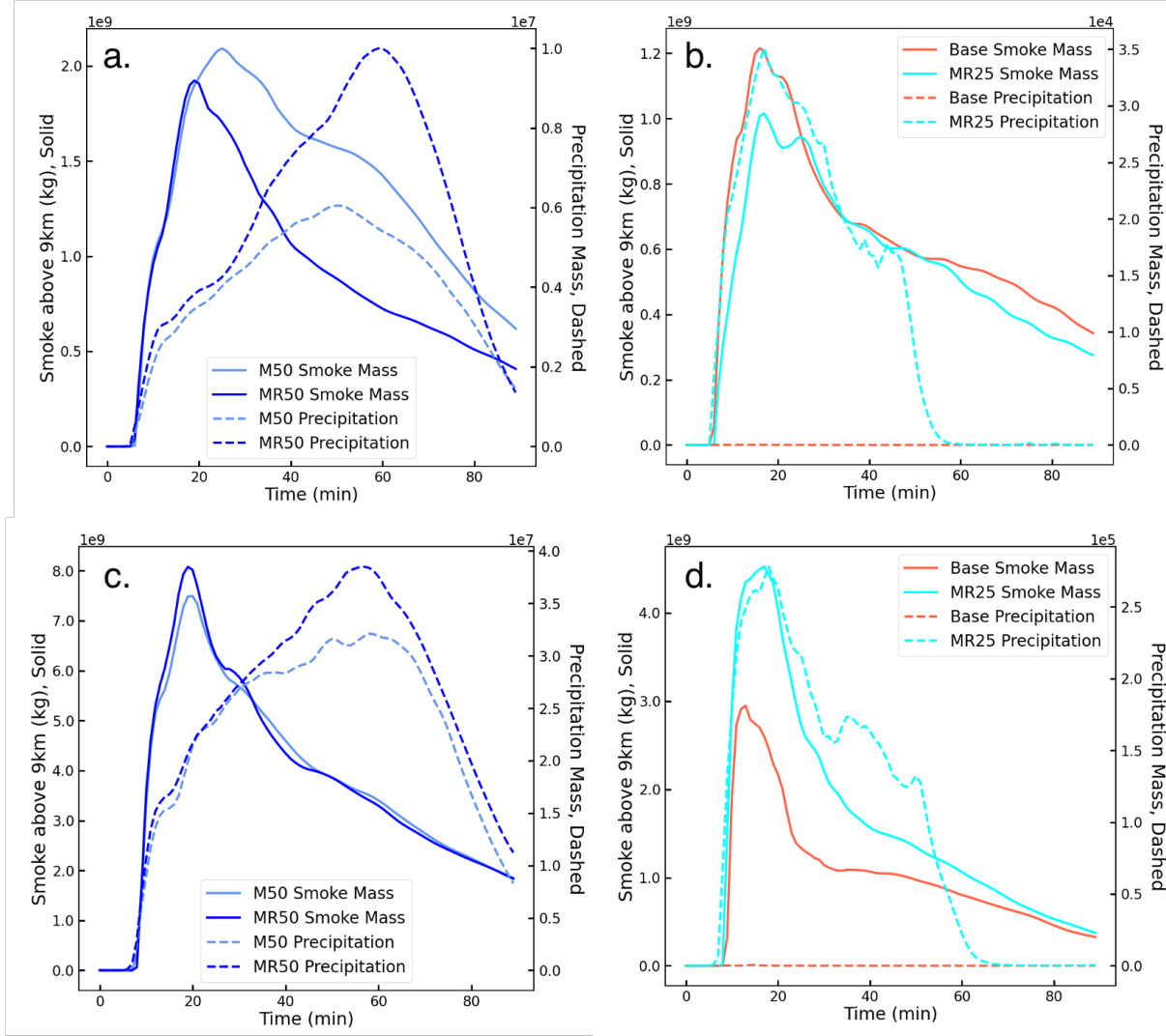


Figure 3.8: Time series of total smoke above 9 km (solid) and precipitation in the domain (dashed) for M50.2 and MR50.2 (a), Base.2 and MR25.2 (b), M50.4 and MR50.4 (c), and Base.4 and MR25.4 (d).

above 9km than MR50.4 (14.76%, compared with 14.37%). Likewise, even though Base.4 does not develop precipitation while MR25.4 does, the stronger convection with the larger fire size, deepened by the increased latent heat release in MR25.4, lofts enough smoke above 9 km that even with rainout more smoke still remains in the upper troposphere in MR25.4 (5.93%) than in Base.4 (3.02%).

MR75 lofts the most smoke of all the simulations, at almost 20% above 9 km and 2.6% above 12 km for MR75.4, followed by the less humid cases in accordance with their water vapor

content (Table 3.4). Despite significant increases in the total smoke rise into and above the upper troposphere, the overall percent smoke rise above 9km and 12km for all the moisture cases is lower for the 4-km radius fire than for their counterparts with the 2-km radius fires (Tables 3.3 and 3.4).

Following these findings, we may also conclude that even though scavenging effects are not considered in WRF, the effect of scavenging is somewhat represented due to the parcel-following behavior of the passive smoke tracer.

### **3.5.2.3 Atmospheric Boundary Layer (ABL) Stability**

ABL stability, hereafter also referred to as atmospheric stability, may enhance or reduce a large fire's intensity, which in turn affects the probability it will mature into a firestorm (Cotton, 1985; Penner et al., 1986). Past studies have indicated that a stable atmosphere will dampen convection strength, while a more convective atmosphere will enhance lofting capacity. Two cases—neutral (the base case) and stable—have been selected to evaluate this theory. Both have a stable free troposphere, with varying stability in the 2-km deep boundary layer. In the case of both fire sizes, we find that boundary-layer stability exerts a slight influence on the smoke distribution.

With the smaller ignition radius and, therefore, the lower heat release, the stable boundary layer dampens plume rise. Compared with Base\_2, which lofts over 9% of the smoke generated into the upper troposphere and stratosphere, Stable\_2 is only able to inject 3.16% that high (Table 3.3, Fig. 3.9a,b). However, when the fire radius is increased to 4 km, the difference between the two cases' lofting capabilities shrinks, and Base\_4 lofts only 1.07% more smoke above 9 km than Stable\_4 (Table 3.4, Fig. 3.9c,d). We conclude that, as with the moisture variability, the heat release associated with the larger fire size can overwhelm the influence of atmospheric stability.

### **3.5.3 Relative Importance of Moisture and Winds**

Certain metrics can give us insight into which atmospheric factors more strongly affect the depth of smoke lofting from a fire. Horizontal wind speeds, vertical velocity, and CAPE facilitate comparative analysis among fires in varying atmospheric conditions to evaluate in which settings



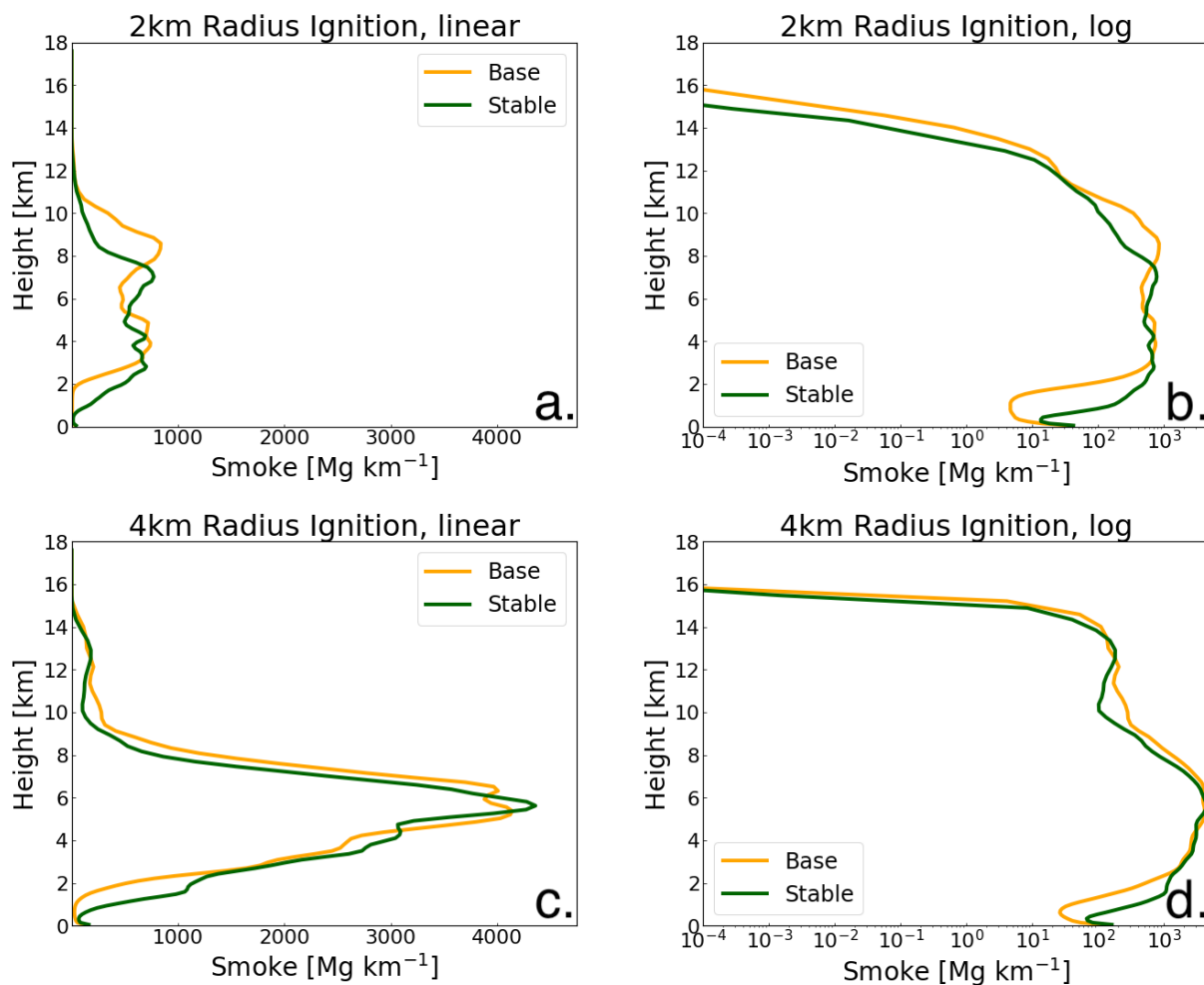


Figure 3.9: Final profiles of vertical smoke distribution (in  $\text{Mg km}^{-1}$ ) for the stability simulations after 1.5 hours of burning. Linear plots (a,c) and logarithmic plots (b,d), for the 2km radius (a,b) and 4km radius (c,d) ignitions are shown.

more smoke may rise high in the atmosphere.

### 3.5.3.1 Horizontal Wind Speeds and Vertical Velocity

The simulations for both the 2-km radius and 4-km radius fires have shown that despite fire size, the horizontal wind speeds will influence vertical velocity and, therefore, the total amount of smoke reaching the upper troposphere and stratosphere. With the smaller fire, which has a weaker heat flux and lower vertical velocities ( $w$ ), horizontal winds can more easily mix the plume out lower

in the atmosphere. The stronger the horizontal winds, the less smoke will be lofted. A clear trend emerges between vertical velocity and horizontal wind speeds (Fig. 3.10). They have a negative linear relationship with an R-squared value of 0.95. Similarly, vertical velocity and smoke above 9 km also have a linear relationship, with an R-squared value of 0.94 (Fig. 3.10a). Smoke in the stratosphere and horizontal wind speeds are related via an exponential decay function.

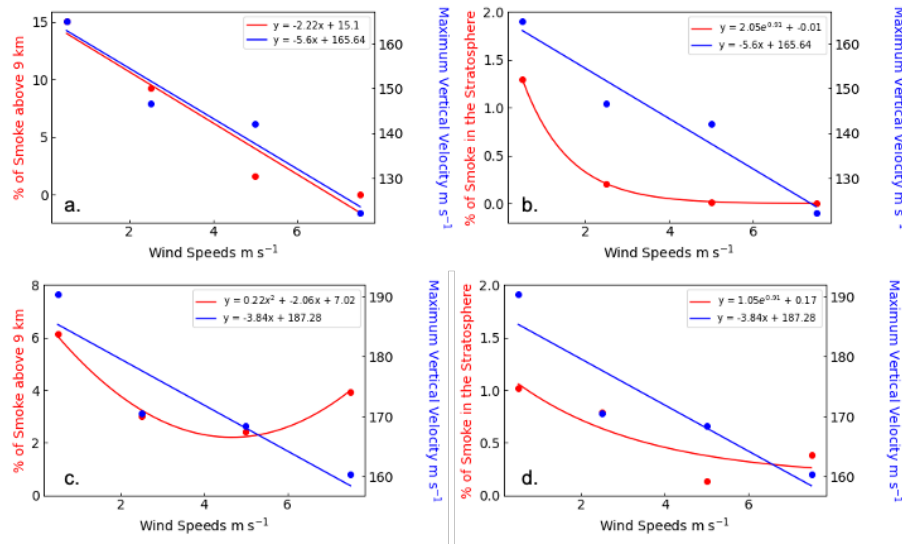


Figure 3.10: Percent of smoke reaching the upper troposphere (a,c) and stratosphere (b,d) compared with wind speeds (red) and maximum vertical velocity in the domain compared with wind speeds (blue), for the 2-km radius ignition (a,b) and the 4-km radius ignition (c,d).

With an increase in heat flux, the relationship between smoke rise and horizontal winds becomes less clear. Vertical velocity and wind speeds maintain a negative linear relationship, with an R-squared value of 0.84 (Fig. 3.10c). However, the link between vertical velocity and upper tropospheric and stratospheric lofting, as found here, shifts. They both correlate with horizontal wind speeds via a second-order polynomial, as percent lofting begins to increase with higher wind speeds at this fire size (Fig. 3.10d). This relationship should be viewed cautiously, as the heat release during ignition slightly differs between the two simulations, as can be seen in Fig. 3.3. The heat flux for HiWi\_4 continually rises, peaks, and then drops, whereas for MidWi\_4, the heat release rate is not a constantly increasing value when the fire is lit. This difference results in a greater

amount of initial lofting for HiWi-4, which is made possible because the convection from this larger fire is less affected by the background horizontal winds.

The updraft velocities seen in our simulations are extremely fast, as they result from such a large area of fuel igniting at once. Additionally, we assess only four data points for each fire size. Therefore, we recommend further simulations incorporating a larger sample size with slower vertical velocities and more ambient horizontal wind speed variability to better quantify these relationships.

### 3.5.3.2 Vertical Velocity and CAPE

CAPE and vertical velocity ( $w$ ) after ignition can indicate how much smoke is lofted; however, we find that CAPE presents a much stronger signal. CAPE is a measurement of rising potential present in a parcel, based on its buoyancy. Higher CAPE values imply that the parcel will rise. Negative values are associated with stability. Vertical velocity specifies how quickly a parcel is currently ascending or descending. By comparing the maximum values of each, for each simulation, with the percent of smoke lofted into the upper troposphere, a relationship between the metrics and smoke rise emerges.

For the smaller fires, as maximum CAPE of any parcel at the surface and maximum  $w$  during the simulation increase, the total smoke injected in the upper troposphere generally increases as well (Fig. 3.11). CAPE has a relatively strong correlation with the percent of smoke that reaches the upper troposphere ( $r^2$  value of 0.8), while vertical velocity has a weaker relationship ( $r^2$  of 0.46). With the increased fire size and higher HRR, the CAPE-smoke relationship weakens slightly ( $r^2$  of 0.7), and the  $w$ -smoke relationship deteriorates altogether.

As is seen in Figure 3.11a and b, the cases with relative humidities at 50% or greater stand out against what could otherwise be a strong positive relationship between vertical velocity and smoke lofting: higher  $w$  would be correlated with increased more smoke rise. The addition of moisture, however, enhances smoke lofting above and beyond the effect of high vertical wind speeds, and the three higher-moisture cases for each fire size have more lofting than what would be indicated by a  $w$ -smoke correlation. If we consider maximum  $w$  as a metric linking smoke lofting with background

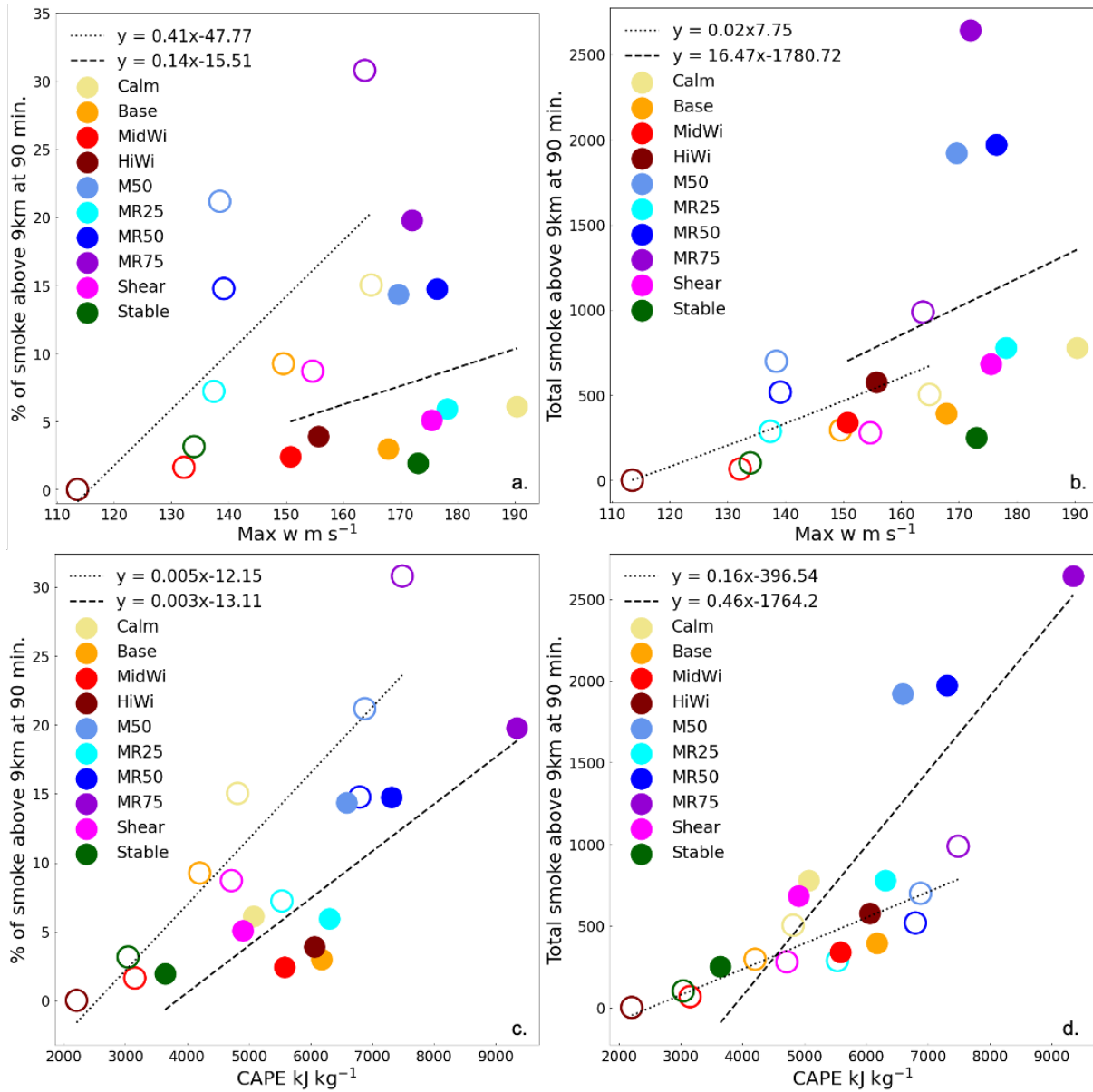


Figure 3.11: Maximum vertical velocity (a,b) and maximum CAPE within the fire area (c,d) compared with % smoke rise above 9 km (a,c) and total smoke rise above 9 km in Mg (b,d), for all 20 simulations. The unfilled markers indicate values from the 2-km radius ignition, while the solid markers correspond to the 4-km radius fire. Each plot has regressions plotted over their 2-km (dotted) and 4-km (dashed) subsets of data points.

winds (as that relationship has already been demonstrated), and CAPE as a metric linking lofting with atmospheric humidity, the insensitivity of the CAPE-smoke relationship to varied wind speeds, when compared with the sensitivity of the  $w$ -smoke relationship to moisture, calls attention to how

moisture exerts more influence over plume rise than horizontal winds.

Additionally, in general, the cases with specified background moisture develop higher CAPE than the dry cases of the same ignition area. However, the dry, quiescent simulations have the highest maximum  $w$  values. Although vertical velocities may reach larger values—particularly in situations where horizontal wind speeds are weak—the role of latent heat release and the generation of buoyancy throughout the vertical extent of the domain plays a more dominant role in plume rise than horizontal winds.

These two findings, therefore, highlight the pivotal role moisture has in dictating plume height. We can conclude that moisture effects are more influential on plume rise than winds.

### 3.6 Discussion

In this study we have evaluated how local meteorology impacts the depth of smoke injection in the atmosphere as the result of a large, areal fire ignition. Specifically, the effects of varying background wind speeds, relative humidity, and atmospheric stability are examined for two different initial fire areas. Additionally, for the cases with moisture, the effects of a radiation parameterization are also evaluated. Although previous studies (Penner et al., 1986) found that plume rise is very sensitive to the fuel burned (and, therefore, the amount of energy released), changes in fuel loading are not considered here. Our simulations all employ a homogeneous wildland fuel bed loading of about  $1.3 \text{ g cm}^{-2}$ , which, although consistent with wildfires, is low compared with urban fuel sources.

Overall, our results all support the conclusions of most previous studies focused on urban fires following a nuclear conflict. Rodden et al. (1965), Crutzen and Birks (1982), and Penner et al. (1986) determined that a moist atmosphere and denser fuels enhance lofting, while a stable atmosphere and increased horizontal wind speeds dampen it. In this study, we find that the inclusion of moisture has the most significant impact—more so than either of the other factors assessed—on deep convection, for both fire sizes. A reduction in horizontal wind speeds also enhances plume rise, while the addition of thermal stability in the ABL dampens it.

We have also shown that an increase in fire size does not increase the overall area average heat release rate; it does, however, escalate the overall energy release from the fuel bed upon ignition, as a larger area is consumed by fire. This greater energy release generates overall stronger convection, but it is spread over a wider swath of land. As a result, with the larger fire area, the gains in smoke lofting compared with the increase in smoke generation are smaller, so many of the 4-km simulations actually exhibit a decrease in the percentage of smoke injected into the upper atmosphere.

Additionally, as convection strengthens and vertical velocities increase (as with the larger fires), factors affecting lofting that are directly impacted by stronger upward motion become less crucial in influencing plume injection height. Horizontal wind speeds and boundary-layer stability lose their significance in damping plume rise; stronger upward motion allows the smoke rise to overcome these elements and more homogeneously reach deeper into the upper atmosphere. And, because the convection column raises smoke so high and so quickly, the effects of radiation on latent heating are also diminished. Plume injection heights for these particular larger fire simulations, therefore, become more comparable with one another. With respect to variations in water vapor, the increased convection has little impact on the influence atmospheric humidity has on plume rise, which is derived from latent heat release into the convection column. Faster vertical velocities do not especially affect the relevance of moisture, so the relative differences in smoke lofting among MR25, MR50, and MR75 remain consistent between the two fire sizes. These differences (or lack thereof) are depicted in Fig. 3.12, where a metric for lofting (the height above which 50% of smoke is lifted) is plotted for each case and fire size.

We compare our final vertical smoke profiles with those of Penner et al. (1986) and Reisner et al. (2018) in Fig. 3.13. Unlike the Penner et al. (1986) study, we do not have a specified, constant heat release in our fire area, as shown in Fig. 3.3. Penner et al. (1986) applied heat release rates of  $89 \text{ kW m}^{-2}$  ( $10 \text{ g cm}^{-2}$  fuel loading),  $14 \text{ kW m}^{-2}$  ( $3 \text{ g cm}^{-2}$  fuel loading), and  $2.2 \text{ kW m}^{-2}$  ( $0.5 \text{ g cm}^{-2}$  fuel loading) to simulate three separate fires, with the highest mass loading fire burning for 6 hours, and the other two burning for 12 hours. In contrast, our fires burn for a shorter period

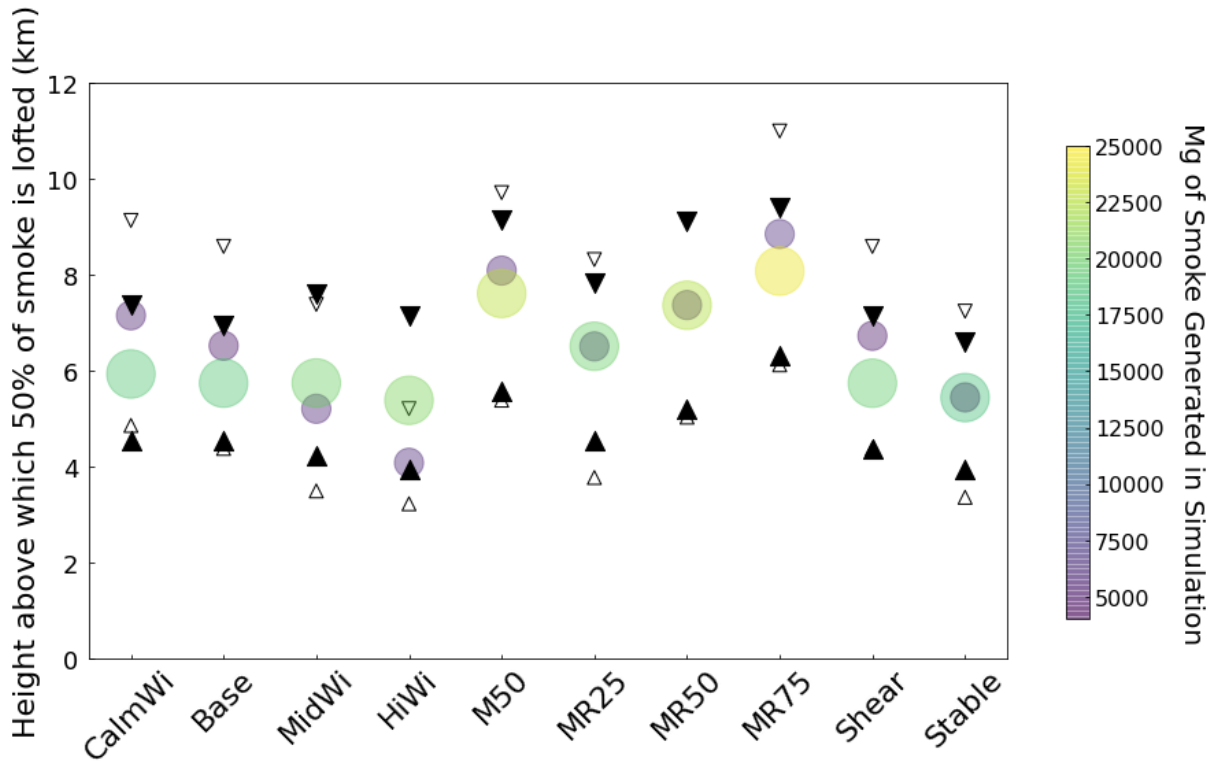


Figure 3.12: Height above which half of the smoke is lofted, based on the final vertical profiles, for each simulation (circles). Smaller markers indicate the 2-km radius fire; larger markers indicate the 4-km radius fire. Markers are colored according to the amount of smoke generated by that simulation. Additionally, the heights above which 25% and 75% of the smoke is lofted are indicated by triangles (upward facing for 25%, downward for 75%), with smaller, hollow markers signifying the 2-km radius ignition, and larger, filled markers signifying the 4-km radius ignition.

of time (1.5 hr) and the surface heat release decreases with time as the fuel in the initial ignition area (mass loading of  $1.3 \text{ g cm}^{-2}$ ) is consumed and the fires begin to spread as perimeter fires. The FIRETEC simulation conducted by Reisner et al. (2018) is more comparable in that regard. That simulation was run for 40 minutes, and the heat release replicated what would be expected as their fuel depleted with time.

Interestingly, we find that the distribution of our vertical profiles more closely aligns with those of Penner et al. (1986) than of Reisner et al. (2018). HiWi.2 injects the majority of its smoke between 3 and 5km, which is akin to Penner et al. (1986)'s  $14 \text{ kW m}^{-2}$  case. MR75.2 injects the majority of its smoke between 6 and 9 km, slightly below Penner et al. (1986)'s  $89 \text{ kW m}^{-2}$  injection

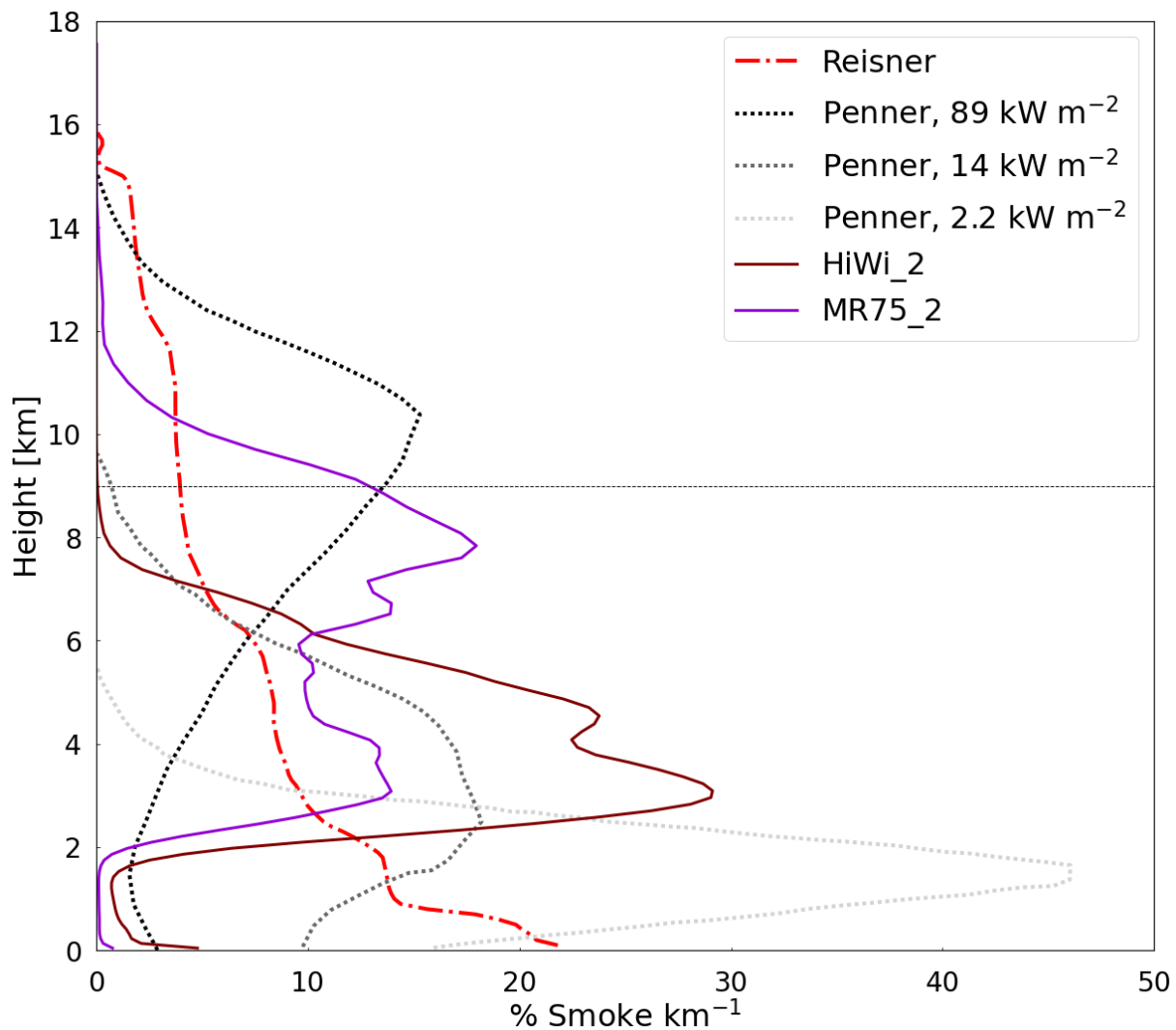


Figure 3.13: Final vertical smoke distributions of fires simulated in Penner et al. (1986) (dotted), Reisner et al. (2018) (dash-dotted), and this study (HiWi\_2 and MR75\_2 only, solid). 9 km height is marked by the horizontal dashed line.

point that peaks just below 11 km. Reisner et al. (2018), on the contrary, saw diminishing smoke injection higher up in the atmosphere, with the bulk of smoke injection occurring within the lowest kilometer of the model. Therefore, compared with the most recent study (Reisner et al., 2018), our results imply a much different risk factor associated with a nuclear conflict. While we did not inform a GCM simulation with the output of our microscale modeling to evaluate the large-scale climate forcing from our fires, we can qualitatively conclude that higher relative humidity and more



quiescent conditions at the detonation site, as well as a denser fuel load (associated with a higher heat release rate), could ultimately deliver a higher nuclear winter risk than what was shown by Reisner et al. (2018).

As previously mentioned, the findings in this study are constrained by certain aspects of the model used and the environment selected. Our fuel bed is representative of a wildland source, which has lower fuel density and higher moisture content than urban fuels. The most likely scenario resulting in the ignition of a large, areal fire, as is simulated here, would be the detonation of a powerful weapon, likely in an urban center. WRF-Fire does not currently incorporate cloud seeding, scavenging, or rainout of particulate matter; however, scavenging and rainout are both indirectly captured by the nature of the passive tracer and its parcel-following character. Radiative self-lofting of smoke is not considered. There are no breaks in the fuel bed, nor is there any heterogeneity, as would be found in an urban (or even a mixed wildland) domain. Branding is not considered; lightning is also not modeled. Finally, there is no oxygen starvation within the model, although we demonstrate that oxygen starvation likely does not play a role in our simulations.

This study has examined the influence of several local atmospheric factors on plume rise following the ignition of a large, areal, wildland fire, and has found that background winds, relative humidity, and boundary-layer stability are all important. The motivating context for this idealized sensitivity study is to increase understanding of what local atmospheric factors may prime a region for deep smoke and soot lofting following a nuclear conflict. Therefore, to develop a better understanding of how denser fuel sources may influence smoke lofting, future work with an urban fire model and a global climate model, preferably one considering aerosol effects, is recommended.

### 3.7 Acknowledgments

Funding for this study has been provided by the Open Philanthropy Project. This work was authored [in part] by the National Renewable Energy Laboratory, operated by Alliance for Sustainable Energy, LLC, for the U.S. Department of Energy (DOE) under Contract No. DE-AC36-08GO28308. Funding provided by the U.S. Department of Energy Office of Energy Efficiency

and Renewable Energy Wind Energy Technologies Office. The views expressed in the article do not necessarily represent the views of the DOE or the U.S. Government. The U.S. Government retains and the publisher, by accepting the article for publication, acknowledges that the U.S. Government retains a nonexclusive, paid-up, irrevocable, worldwide license to publish or reproduce the published form of this work, or allow others to do so, for U.S. Government purposes.

This work utilized resources from the University of Colorado Boulder Research Computing Group, which is supported by the National Science Foundation (awards ACI-1532235 and ACI-1532236), the University of Colorado Boulder, and Colorado State University.

<b>WRF Parameter</b>	<b>d01</b>	<b>d02</b>
Horizontal Resolution	1.1 km	100 m
Horizontal Extent (Grid Cells)	200 x 200	199 x 199
Number of Vertical Levels	80	
Model Top	18 km	
Lowest Vertical Level	60 m	
Time Step	3 s	0.27 s
Time Integration Scheme	Runge-Kutta 3rd Order	
Advection Scheme	5th-order Horizontal; 3rd order Vertical	
Coriolis Parameter	$10^{-4} \text{ s}^{-1}$	
Planetary Boundary Layer Scheme	MYNN	-
Eddy Coefficient Option	2D horizontal diffusion	1.5-order SGS TKE
Surface Layer Scheme	MYNN	
Turbulence & Mixing	-	Isotropic with 1.5-order TKE closure scheme
Damping	Upper-level Rayleigh layer of $0.33 \text{ s}^{-1}$ with a depth of 5 km	
Roughness Length	0.3 m	
Microphysics Scheme	Thompson	
Boundary Conditions	Periodic	Interpolated, One-way Nested
Fire Grid Mesh	-	4:1
Ignition Radius	-	2-km or 4-km
Fuel Source	-	Heavy Logging Slash, 0.9 m depth ( $1.3 \text{ g cm}^{-1}$ )
Smoke Handling	-	Passive Tracer

Table 3.1: WRF Configuration

Simulation	Label	Wind Speed	Stability	Moisture	Radiation	Wind Shear	Relative Humidity
Base	Base	2.5 m s <sup>-1</sup>	Neutral	Dry	No	No	0%
Calm	CalmWi	0.5 m s <sup>-1</sup>	Neutral	Dry	No	No	0%
Mid Winds	MidWi	5 m s <sup>-1</sup>	Neutral	Dry	No	No	0%
High Winds	HiWi	7.5 m s <sup>-1</sup>	Neutral	Dry	No	No	0%
50% RH	M50	2.5 m s <sup>-1</sup>	Neutral	Moist	No	No	50%
25% RH + Radiation	MR25	2.5 m s <sup>-1</sup>	Neutral	Moist	Yes	No	25%
50% RH + Radiation	MR50	2.5 m s <sup>-1</sup>	Neutral	Moist	Yes	No	50%
75% RH + Radiation	MR75	2.5 m s <sup>-1</sup>	Neutral	Moist	Yes	No	75%
Wind Shear	Shear	2.5 m s <sup>-1</sup>	Neutral	Dry	No	Yes	0%
Stable	Stable	2.5 m s <sup>-1</sup>	Stable	Dry	No	No	0%

Table 3.2: Simulation Overviews. When referenced elsewhere, each label is followed by an underscore and the fire radius. For example, the base case for the 2-km radius fire will be referred to as Base\_2. Note: "Moist," as used in describing the simulations, refers specifically to the addition of atmospheric humidity. Once the fire is lit, all simulations see some release of moisture from the fuel source.

Simulation	Total Smoke (Mg)	Smoke above 9 km (Mg)	Smoke above 9 km (%)	Smoke above 12 km (Mg)	Smoke above 12 km (%)	Total Error (%)
Base_2	3.2E3	296.1	9.25	6.6	0.21	2.45
CalmWi_2	3.4E3	504.1	15.03	43.3	1.29	-2.26
MidWi_2	4.1E3	67.2	1.64	0.5	0.01	-4.27
HiWi_2	4.8E3	0.6	0.01	0.0	0.00	-1.13
Shear_2	3.2E3	279.6	8.71	6.9	0.22	2.39
M50_2	3.3E3	699.4	21.17	37.3	1.13	1.20
MR25_2	4.0E3	287.7	7.23	4.3	0.11	-3.12
MR50_2	3.5E3	518.3	14.77	33.6	0.96	2.14
MR75_2	3.2E3	987.9	30.79	222.6	6.94	2.21
Stable_2	3.2E3	102.2	3.16	4.0	0.12	2.34

Table 3.3: Smoke generation, upper atmosphere and stratospheric smoke lofting, with the 2-km radius ignition area. Negative error values indicate an overestimation of total smoke in the atmosphere, compared with actual smoke generation at the surface, while positive values indicate an underestimation.

Simulation	Total Smoke (kg)	Smoke above 9 km (kg)	Smoke above 9 km (%)	Smoke above 12 km (kg)	Smoke above 12 km (%)	Total Error (%)
Base_4	1.3E4	394.0	3.02	103.5	0.79	0.56
CalmWi_4	1.3E4	779.2	6.13	129.6	1.02	2.80
MidWi_4	1.4E4	388.9	2.43	18.6	0.13	-1.62
HiWi_4	1.5E4	576.6	3.92	56.7	0.39	-1.58
Shear_4	1.3E4	682.7	5.09	124.2	0.93	-1.71
M50_4	1.3E4	1921.6	14.37	134.16	1.00	-1.84
MR25_4	1.3E4	780.2	5.93	77.0	0.59	2.14
MR50_4	1.3E4	1972.6	14.76	235.2	1.76	0.54
MR75_4	1.3E4	2642.5	19.79	349.3	2.62	-1.75
Stable_4	1.3E4	251.7	1.95	99.1	0.77	1.49

Table 3.4: Smoke generation, upper atmosphere and stratospheric smoke lofting, with the 4-km radius ignition area. Negative error values indicate an overestimation of total smoke in the atmosphere, compared with actual smoke generation at the surface, while positive values indicate an underestimation.

## Chapter 4

### The addition of aerosol-atmosphere interactions to address pyrocumulonimbus formation in the Weather Research and Forecasting Model

#### 4.1 Preface

As fires and the fire season have evolved with climate change, more attention is being paid to pyrocumulus (pyroCu) and pyrocumulonimbus (pyroCb) events. Recent wildland fires have drawn more awareness to the extreme weather that powerful fires can generate when the right atmospheric conditions are present. Therefore, accurately simulating pyroCu and pyroCb has risen in importance. There still remains much to be explored about pyroCb, but model simulations can help us develop a better understand of how and why pyroCu and pyroCb form.

In this section, we simulate the Bald Fire—a 2014 summer wildland fire in Northern California that generated pyroCu—three times, to explore the effects of interactions between smoke and cloud microphysics. The first simulation is run with Thompson microphysics and no aerosol-awareness (which prevents the smoke generated from the fire from interacting with cloud formation processes). The second uses the aerosol-aware version of the Thompson scheme, which adds into the model an explicit aerosol number concentration to nucleate new cloud droplets. The final simulation builds on the second one by also including estimated water-soluble particle counts released from fire combustion in the water-friendly aerosols already considered in the aerosol-aware Thompson parameterization.

We find that the addition of the aerosol-coupled scheme (in both cases that use it) results in more cloud water and less precipitation than occurs with the non-coupled scheme. Addition-

ally, we find an overall greater amount of liquid and frozen atmospheric water with the coupled parameterization than without it, despite overall lower heat fluxes in these simulations. Cold cloud development is more prominent in the coupled simulations, and there is more precipitation in the non-coupled case. Overall, there are some important differences that should be further studied, which could provide an avenue for further development of operational fire forecasting models.

## 4.2 Abstract

Accurately representing pyrocumulus (pyroCu) and pyrocumulonimbus (pyroCb) development is becoming increasingly important in fire forecasting models. PyroCb, in particular, can deepen into powerful storms that can cause violent weather, spark new fires through lightning strikes, and inject a substantial amount of fire smoke and other combustion byproducts into the upper atmosphere and lower troposphere (UTLS). The long-term climatologic impacts of the last item are currently unknown, but a broadened understanding of what conditions can result in such dramatic lofting, and how much smoke can be convected into the UTLS, can inform climate models examining such effects. In this study, we simulate a fire that burned in Northern California during the 2014 wildfire season. This fire developed pyroCu and pyroCb during its second day, when upper-level monsoonal moisture advected over the region. We run three separate simulations using the Weather Research and Forecasting Model, Version 4.0.1 (WRF-ARW) and its fire parameterization (WRF-Fire) to explore interactions between fire smoke and cloud microphysics. All three simulations use a passive tracer to represent fire smoke. The first simulation does not consider any aerosol-atmosphere interactions. The second simulation assumes a specified number of environmental aerosols that do interact with the microphysics. Finally, the third simulation employs a simple coupling between combustion byproducts and the microphysics, allowing for a greater number of water-friendly aerosols to seed cloud development. We find that the addition of aerosol coupling does result in a slightly larger amount of cloud activity by the end of the simulations, as well as less precipitation and more cold cloud development.

### 4.3 Introduction

Intense wildfires can release a great amount of heat as they burn, generating powerful convection—known as pyro-convection—as a result. If enough moisture is present, clouds and rainstorms can form. These features, known as pyrocumulus (pyroCu) and pyrocumulonimbus (pyroCb) (American Meteorological Society, 2013), have the potential to transport large amounts of combustion byproducts like smoke and biomass aerosols into the upper troposphere and lower stratosphere (UTLS), where they can remain for months and have widespread climatic consequences (M. Fromm et al., 2000). This phenomenon has also been attributed to hypothetical scenarios wherein a nuclear exchange occurs and enough urban fires are ignited to create a "nuclear winter" (Turco et al., 1983b).

The evaluation of pyroCu and pyroCb is a relatively new area of research, as they were only first recognized in early 2000. M. Fromm et al. (2000) noted a 1998 stratospheric aerosol increase at high northern latitudes, and postulated that it was the result an active wildfire year in northwestern Canada and Russia. Previously, the main source of such anomalies was considered to be volcanic activity (Luderer et al., 2006; M. Fromm et al., 2010b). Primary observational analysis since then has been conducted by way of case studies—the most notable early examples being Alberta’s 2001 Chisholm Fire and Australia’s 2003 Canberra fire (M. D. Fromm & Servranckx, 2003; Rosenfeld et al., 2007; M. Fromm, Torres, et al., 2008; M. Fromm, Shettle, et al., 2008)—but investigations of pyroCb activity over longer time spans (Kahn et al., 2008; Peterson, Fromm, et al., 2016; Peterson, Hyer, et al., 2016; Kablick et al., 2020) as well as modeling work have been increasing in frequency.

Many aspects of pyroCu and pyroCb formation are still not well understood, but studies so far have uncovered information about the roles various factors play in determining how and why they develop. Typical fire forecasting measures such as the Haines index (Haines, 1989)—a measurement derived from measurements of the moisture content and stability in the lower atmosphere—can be useful in predicting deep fire cloud development (M. Fromm et al., 2010b; Peterson, Hyer, Campbell, et al., 2014; Peterson, Hyer, et al., 2016), but other metrics such as convective available



potential energy (CAPE) are not as helpful, as pyroCb's can form with both high and low values present (M. Fromm et al., 2010b; Peterson, Hyer, Campbell, et al., 2014; Peterson, Hyer, et al., 2016; Peterson, Fromm, et al., 2016; K. J. Tory, Thurston, & Kepert, 2018). The inverted-V sounding profile characteristic of severe weather and dry thunderstorm formation (Beebe & Bates, 1955; Wakimoto, 1985) under typical convective criterion has been widely associated with pyroCb presence (Rosenfeld et al., 2007; K. Tory & Thurston, 2015; Peterson, Hyer, et al., 2016; K. J. Tory et al., 2018). That is, environments conducive to pyroCb development have been noted to have a dry, unstable boundary layer, above which is a moist mid-tropospheric layer (Fig. 4.3). In the Western North American mid-latitude region, the source of the upper-level moisture is often monsoonal activity (Lareau & Clements, 2016; Peterson, Hyer, et al., 2016). This setup is typical for dry thunderstorm formation, and it has been found to be favorable for North American pyroCb development, as well (Nauslar, Kaplan, Wallmann, & Brown, 2013; Peterson, Hyer, Campbell, et al., 2014; Peterson, Hyer, et al., 2016). These storms, therefore, commonly form during the mid-afternoon to evening hours. Additionally, compared with other severe weather systems, pyroCb are seeded with a higher number of cloud condensation nuclei (CCNs) that originate from the fire smoke (Rosenfeld et al., 2007). Their anvils last longer as a result (D. T. Lindsey & Fromm, 2008).

There has also been debate over which factor is more important in determining pyroCb activity: latent heating derived from moisture release when wildland fuels burn (Potter, 2005; Cunningham & Reeder, 2009), or the sensible heat flux from the fire itself coupled with mid-tropospheric moisture (Trentmann et al., 2006; Luderer, Trentmann, & Andreae, 2009; Lareau & Clements, 2016). Models have indicated that entrainment of dry air into the plume in the free troposphere can decrease the strength of convection, supporting the argument that atmospheric humidity is an important factor in pyroCb formation, more so than that provided by the fuel source.

Observational studies have led to newfound understanding of not only pyroCb dynamics and development, but also how powerful they can be. After only three hours of pyroCb development, enough of the Chisholm Fire's plume was injected into the UTLS that it encircled the entire Northern Hemisphere and remained for three months before decaying (M. Fromm et al., 2000). A

similar phenomenon occurred following the Canberra Fire, which was discovered to have released more energy at its peak burn intensity than the WWII Hiroshima nuclear bomb (M. Fromm et al., 2006). In 2017, a rampant wildfire season in the U.S. Pacific Northwest and British Columbia injected into the UTLS a smoke load comparable to that from a volcanic eruption (Peterson et al., 2018b; Yu et al., 2019). While volcanoes have been observed to loft large amounts of smoke—on the order of teragrams—into the stratosphere, they only do so infrequently (M. Fromm et al., 2010b). Therefore, the implications of a fire season injecting this level of smoke, especially in light of the expectation of longer and more intense fires to come as the result of climate change, has significant seasonal and climatic implications (Peterson, Hyer, et al., 2016).

In this modeling study, we use the Weather Research and Forecasting model and its fire parameterization (WRF-Fire) to simulate a fire based on one that burned in California during summer, 2014 (Lareau & Clements, 2016). A day and half after ignition, an upper-level moist layer blew over the area, coinciding with the afternoon formation of a pyroCb. We attempt to simulate the deep cloud formation observed above the fire by running WRF-Fire with three different microphysics options—one without aerosol-microphysics coupling, one with the coupling, and one with the coupling and an added aerosol load from fire combustion—to address the hypothesis that introducing a water-friendly aerosol scheme will lead to a greater number of CCNs and increased cloud formation, which can lead to deeper convection as a result. We evaluate the differences among these simulations’ abilities to represent pyroCu and pyroCb formation.

The paper is laid out as follows: The next section provides an overview of the case chosen for this study, as well as the motivation behind its selection. Following that, we give a description of the model setup and an explanation of the method used to add combustion aerosols to the water-friendly aerosol count. We then present our findings, followed by a brief discussion and conclusions from the study.

## 4.4 Case Selection and Scope of Study

The fire selected for this study ignited in Northern California on July 31, 2014. Known as the Bald Fire, it burned over 14,000 ha during its first two days and on the second afternoon, following the advection of a mid-tropospheric moist layer into the region, pyroCu and pyroCb formed. The cloud tops extended up to a height of 12 km. Lareau and Clements (2016) found that outside of the pyroCu, the smoke layers rose to only around 6 km. Additionally, their findings back up the argument that upper-level moisture—particularly in the form of monsoonal surges for the western coast of North America—play a particularly pertinent role in pyroCu and pyroCb formation.

Due to the focus and findings of the Bald Fire observational study, we have selected it for evaluation with WRF-Fire. This study examines the model’s capacity for simulating pyroCu and pyroCb above the Bald Fire with two different Thompson microphysics options: one that does not include aerosol-cloud effects, and one which does consider aerosol-microphysics coupling (a scheme that henceforth will be referenced as TWFA) (Thompson et al., 2008; Thompson & Eidhammer, 2014). And, because TWFA only considers environmental aerosols, we run a third simulation that includes an additional coupling combustion particle number with the Thompson parameterization. An explanation of how particle count is estimated is provided in Section 4.5.2. Overall, three different simulations are run (Table 4.2).

## 4.5 Methods

### 4.5.1 Model Setup

The model used in this study is the Advanced Research Weather Research and Forecasting Model (WRF), Version 4.0.1 (Powers et al., 2017; C. Skamarock et al., 2019). WRF is a fully compressible, non-hydrostatic atmospheric model that employs terrain-following coordinates, and it is used for both research numerical weather forecasting. WRF-Fire couples with the model to simulate both the fire spread at a sub-grid scale, using a level-set algorithm, and the fire’s heat release (latent and sensible), which interacts with the surrounding meteorology (Mandel, Beezley,

& Kochanski, 2011b; Coen et al., 2013b; Jiménez et al., 2018; Muñoz Esparza, Kosović, Jiménez, & Coen, 2018). This parameterization has been developed to work with 13 pre-defined fuel categories, known as the Anderson wildland fuel standards (Anderson, 1982b). Users may choose to enable a passive smoke tracer to track plume advection.

The model is set up with three, one-way nested domains centered with one another, with horizontal grid cell resolutions of 3 km, 1 km, and 100 m. The innermost domain has a fire grid scaled down by 4:1, giving it a resolution of 25 m for fire-front tracking (Muñoz Esparza, Kosović, et al., 2018). Each grid has the same vertical resolution, with 80 eta levels spaced on the order of 20 m close to the Earth’s surface and stretching out higher in the atmosphere. The domains are positioned such that the fire ignition location is off-center to the southwest, allowing for growth and spread towards the northeast. The domain layout is depicted in Figure 4.1.

The outer domain is forced with ERA5 reanalysis data at 3 hour intervals. Reanalysis datasets are assimilations that combine historical atmospheric, land, and ocean data with output from forecast models to provide a global, synthesized history of the earth’s climate, which can then be used in research applications (Keeley, 2013). The ERA5 data has been released by the European Centre for Medium-Range Weather Forecasts (ECMWF), which has generated a series of reanalysis datasets titled ERA-Interim (ERA-I) and ERA5. ERA5 is the most recent release, with updates from ERA-I that include uncertainty estimates and new parameters. Satellite and in-situ observations are assimilated to inform this dataset, which spans from 1950 through the present. ERA5 has a horizontal resolution of 31km and 137 levels in the vertical expanse, running from the earth’s surface to 80 km (Hersbach et al., 2020).

Three simulations are run with the model parameters outlined in Table 4.1. Both shortwave and longwave radiative forcing are handled by the RRTMG scheme (Iacono et al., 2008). The two outer domains at mesoscale resolutions use the Mellor-Yamada-Nakanishi-Niino (MYNN) planetary boundary layer (PBL) scheme (Nakanishi & Niino, 2009b) and the Smagorinsky first order closure scheme to manage horizontal diffusion. The innermost domain is of large eddy simulation (LES) resolution, and therefore requires no PBL parameterization as most turbulence is resolved within

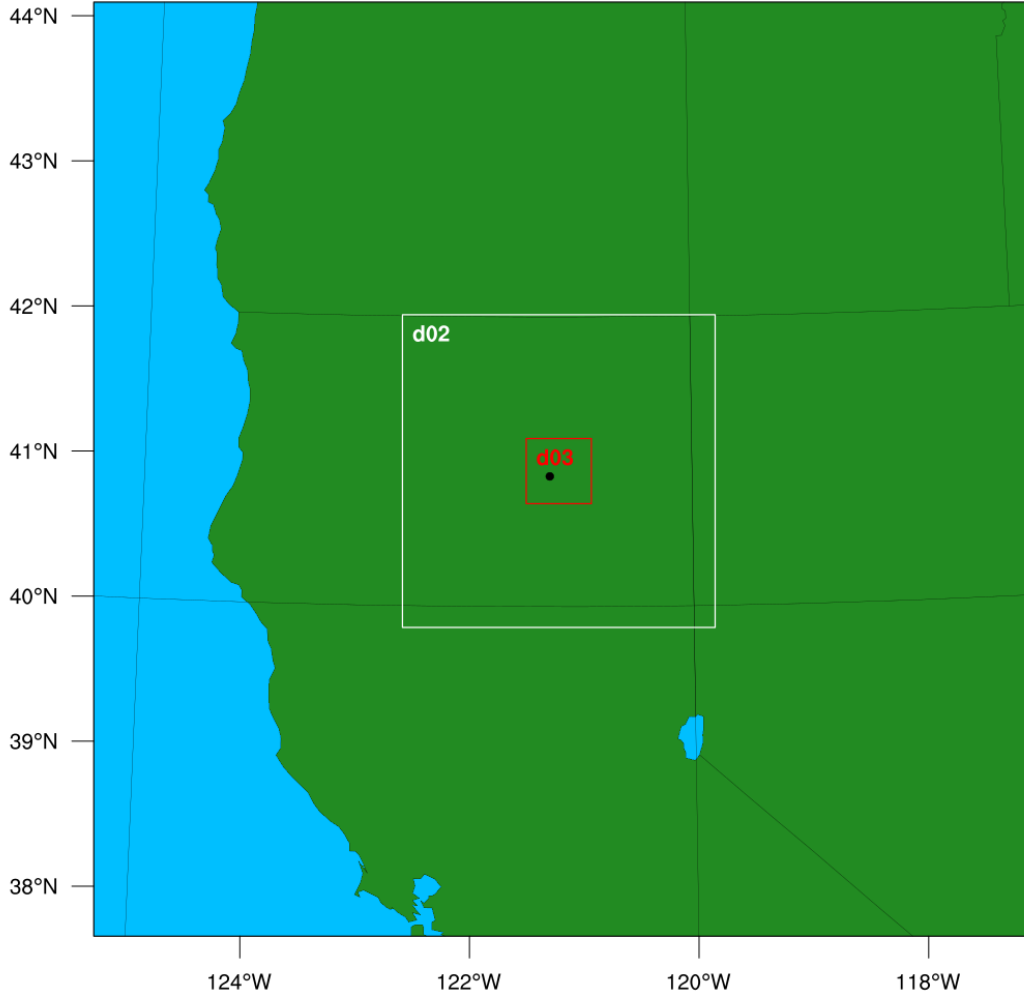


Figure 4.1: Domain extents. The Pacific Ocean is indicated by blue on the western side of the outer domain, while parts of California, Nevada, Oregon and Idaho are all captured by the green area. The fire is indicated by the black marker in d03.

each grid cell. Instead, this domain uses a 3-dimensional 1.5 order turbulent kinetic energy (TKE) closure scheme (Lilly, 1966). Surface layer turbulent fluxes are addressed with the revised MM5 Monin-Obukhov formulation (Jiménez et al., 2012). Land-surface interactions are handled via the unified Noah land-surface model (S.-h. Chen & Dudhia, 2000; Ek et al., 2003; Tewari et al., 2004). To prevent model instability, vertical velocity damping is employed, and a 6 km upper-level Rayleigh relaxation layer is enabled (Klemp et al., 2008). Finally, moisture and scalar variables are calculated with a positive-definite advection scheme.

Each simulation uses the physics and dynamics options listed in Table 3.1, although the microphysics in each differs (Table 4.2). The first case, labeled noWFA, uses the Thompson microphysics scheme and no water-friendly aerosols. The second case, labeled WFA, runs with aerosol-aware Thompson microphysics, which includes in the parameterization a preset distribution of water-friendly aerosols that interact with the traditional Thompson microphysics and seed cloud formation. The aerosol number concentrations are included in a lookup table referenced by the parameterization, and they represent sulfates, sea salts, and organic matter. The number activated at any time step depend on the localized model state (temperature and vertical velocity). Finally, the third case, labeled SMK, employs the aerosol-aware Thompson microphysics and also assumes an additional number of aerosols are generated by fire combustion, which supplement the already-present environmental aerosol concentration (details presented in Section 4.5.2). In all three simulations, smoke is released as a tracer, and it is considered passive in noWFA (only follows the dynamics of the atmosphere), but does interact with the atmosphere in WFA and SMK. The fuel map for the simulations is defined by data taken from the 2014 USGS LANDFIRE database (Ryan & Opperman, 2013).

The fire is ignited on July 31, 2014, 23:00 PDT (August 1, 2014, 06:00 UTC) at 40.9°N, 123°W, in the innermost domain only. Nesting is one-way, so the fire does not affect atmospheric dynamics in the 1-km and 3-km grids. The simulations begin on July 31 at 12:00, when the outer domain is initialized (the two inner domains are initialized 6 hours later), and run through 3:20 PDT on August 2, when the fire front reaches the domain edge and the simulation terminates. Data is output at 1 hour intervals until 11:00 PDT on August 2, when output time is refined to 5 min resolution. Satellite imagery indicates that pyroCu began to develop at 13:30 PDT on August 2, when moist air at 400 hPa advected over the region. Ground-based observational data for the pyroCu and subsequent pyroCb is available through 15:32 PDT (Lareau & Clements, 2016). The simulations terminate when the fires reach the LES nest’s eastern edge, which occurs at a different time for each case, with noWFA reaching the domain boundary first, then WFA, followed by SMK. All complete between 15:00 and 16:00 PDT.

#### 4.5.2 Water-friendly aerosol and combustion coupling

Because combustion organics provide a large number of CCNs that can enhance cloud formation above fires, it may be important to include this effect in fire forecasting models. To adjust for the introduction of these aerosols and their cloud seeding impacts, we have included in one simulation a simplified coupling of combustion smoke with the TWFA microphysics scheme. To calculate an estimation of hydrophilic particle numbers released from a fire, we use an emission factor ( $EF_{PN}$ ) equation for water-soluble particle number released from forest fire combustion, as found by Janháall, Andreae, and Pöschl (2010) and presented in Eq. 4.1. This factor is then multiplied by the amount of fuel burned by combustion (Eq. 4.2) to get total number of particles emitted by the fire.

$$EF_{PN}(kg^{-1}) = (34.4E15 - (34.6E15)(MCE)) \pm 0.8E15 \quad (4.1)$$

$$FB(kg) = A_{F,t} * fgi * \Delta t \quad (4.2)$$

The numerical values in Eq. 4.1 were empirically derived by Janháall et al. (2010). Modified combustion efficiency  $MCE$ , which is the ratio of  $CO_2$  released from combustion to  $CO_2$  plus  $CO$  released from combustion, is assumed to be 0.95, an average value taken from those used in the Janháall et al. (2010) study. In the second equation,  $FB$  is the fuel burned, in kg. The term  $fgi$  is fuel loading, in  $kg\ m^{-2}$ . Fire area per time step in  $m^2\ s^{-1}$  is  $A_{F,t}$ . The model timestep is presented as  $\Delta t$ .

The number of combustion aerosols generated are summed with the environmental aerosols already assumed by the TWFA scheme. This new aerosol concentration then informs heterogeneous cloud droplet and ice particle initialization at each time step. As this is a simplified coupling, the properties of the aerosols are not readjusted from the specifications of environmental aerosols already present in the TWFA lookup table.

## 4.6 Results

The results from this study overall support our hypothesis that the introduction of water-friendly aerosols into the model will increase the number of cloud particles, which we find reduces droplet growth and precipitation. Additionally, we find that with the aerosol-microphysics coupling (WFA and SMK), deeper convection appears to develop, which results in higher cloud tops and a greater amount of smoke lofted higher in the atmosphere. This enhanced lofting is due to a greater amount of latent heat release, which results from a higher incidence rate of condensation and freezing as opposed to collision, coalescence, and accretion, which accelerate particle growth and lead to precipitation. Additionally, the fire spread rate of noWFA is generally higher than that of WFA and SMK, causing the fire to hit the domain edge and terminate earlier than the other two. One thing we do not see in any of the simulations is persistent pyroCu and pyroCb, which were observed above the fire in 2014. Clouds form repeatedly and at their deepest, all tops reach almost 12 km, but their depth rapidly dissipates (Fig. 4.2).

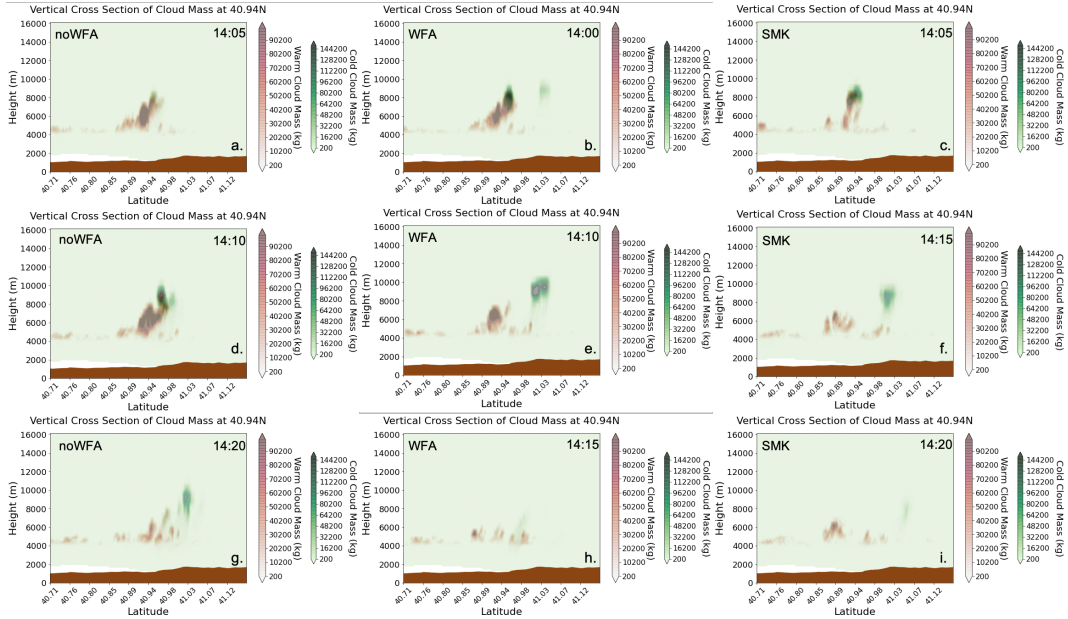


Figure 4.2: W-E cross sections of integrated cloud mass in the N-S direction. Ice, snow, and graupel are considered "cold," while rain and cloud water are "warm." The time stamps of each plot are for August 2 PDT. Plots a, d, and g show the rapid cold cloud progression for noWFA; b, e, and h show the same for WFA; and c, f, and i show the same for SMK.



#### 4.6.1 Fire Spread and Heat Flux Differences

Observations of the Bald Fire showed pyroCu initiation at 13:30 PDT, as a layer of monsoonal moisture around 400 hPa advected into the region (Lareau & Clements, 2016). The simulations' thermodynamic conditions roughly parallel those observed in the region, with a sounding profile showing a dry lower layer and moisture much farther aloft ahead of the fire area before pyroCu formation (Fig. 4.3).

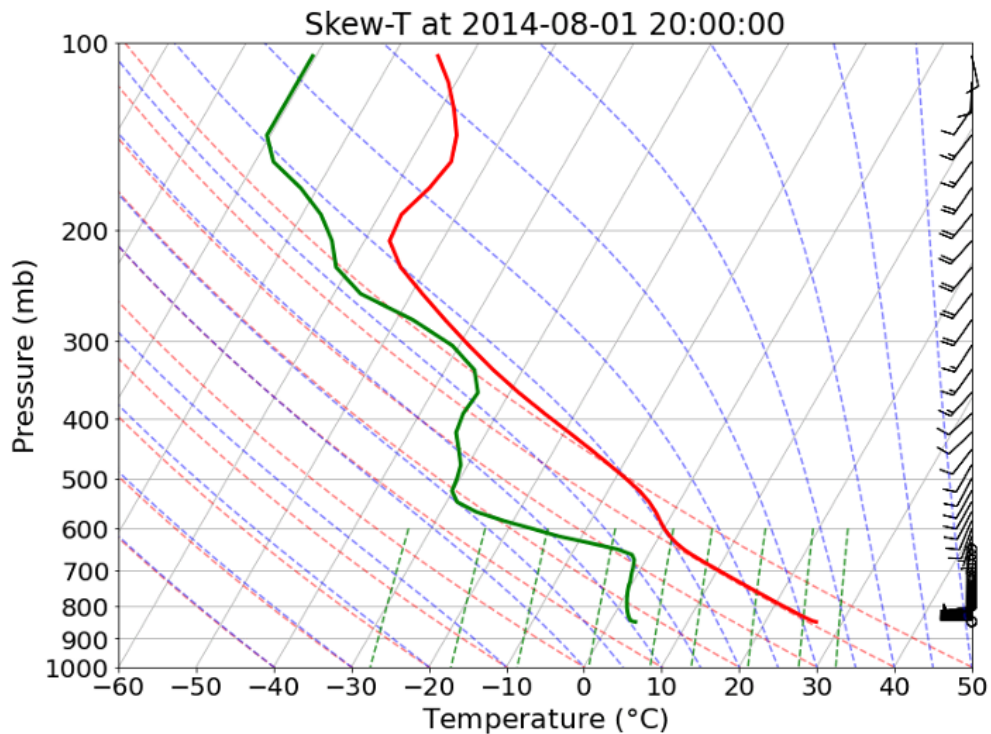


Figure 4.3: Model sounding at the leading (west) side of LES nest, centered in the N-S direction. The green line indicates the dew point temperature profile. The red line shows the atmospheric temperature profile. Moisture at around 350 mb is advected into the region.

The Bald Fire grew nearly 7000 ha on August 2, covering just over 14,000 ha by the end of its second day of burning. Our model results present a burn area of over twice that size, as the spread rapidly increases at two separate times during the simulations—once in the afternoon of the first day, and again during the transition to daytime on the second day, after which the fire spread rate continues to increase until shortly before the simulations complete (Fig. 4.4). This growth

results in an increase of the fire-generated heat flux (Fig. 4.5). As can be seen by comparing the two plots, a rise in fire spread rate will result in a stronger heat flux.

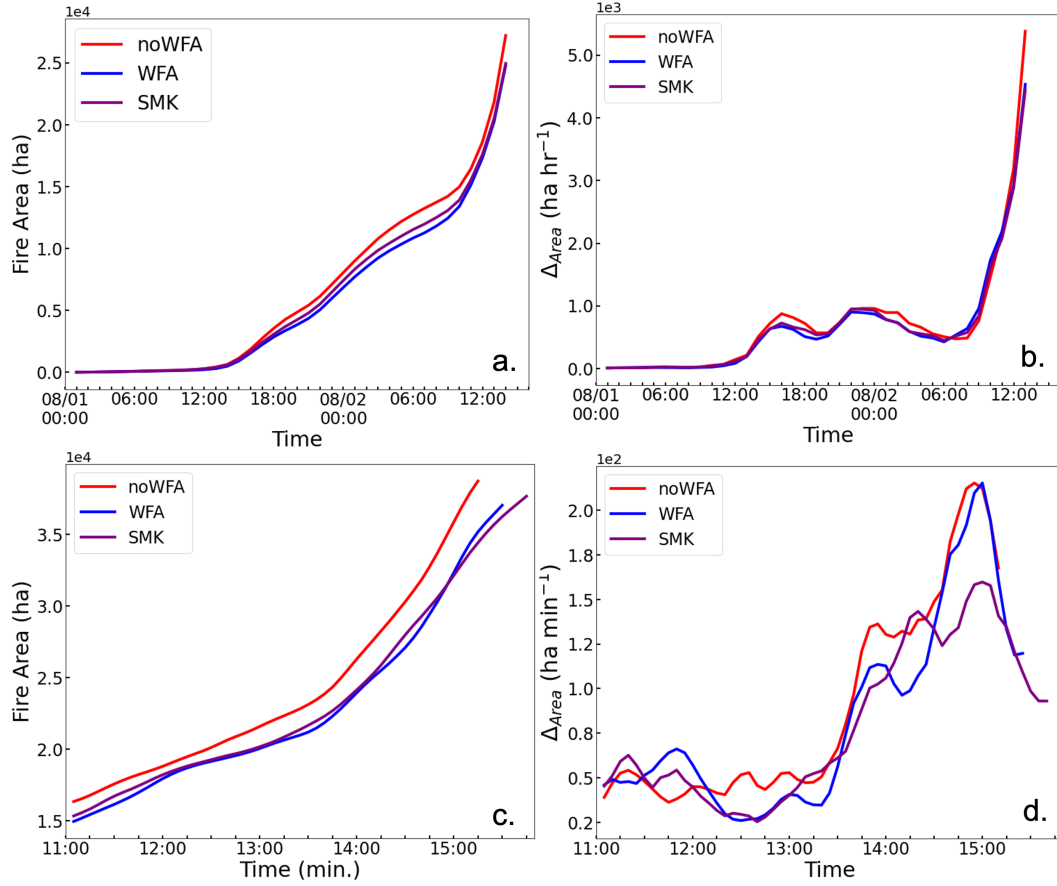


Figure 4.4: Total area burned and change in area burned over time, shown at 1 hr intervals starting with ignitions (a, b) and at 5 min. intervals for the last four hours of the simulation (c, d). The change in burn area is plotted as a rolling 15-minute average.

To better understand the surface wind, updraft, and downdraft behavior during the fire, we have plotted Figures 4.6 and 4.7, which depict maximum 10-m horizontal wind speeds, updrafts, and downdrafts, in the domain at each vertical level over time, for the entire simulation and for the last four hours (at a temporally finer output resolution). Additionally, Fig. 4.8 shows the differences in these maximum wind speeds during the last four hours of the simulations between noWFA and WFA, and between WFA and SMK.

There are two periods during which wind speeds increase, the fires spread more rapidly, and

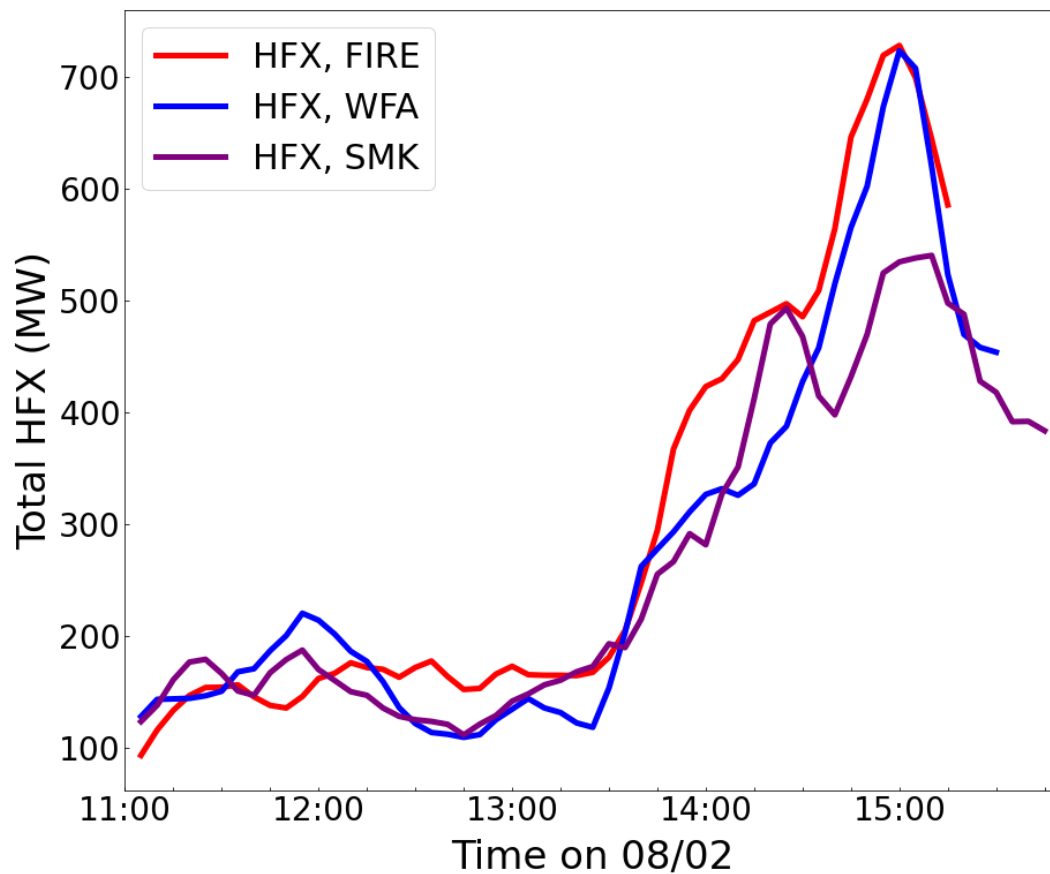


Figure 4.5: Total heat flux from the fire over time, for each simulation, output at 5 min. intervals and shown with a 15 min. moving average.

their surface heat fluxes strengthen. The first increase in 10 m winds is evident in Fig. 4.6a,b,c, which occurs in the late afternoon and evening of August 1, between the hours of 15:00-16:00 and 20:00. This event coincides with an increase in fire spread rate for all three simulations, shown in Fig. 4.4b. Winds pick up again during the final hours of the simulation, specifically beginning around 14:00 (Fig. 4.7a,b,c), as the monsoonal moisture moves into the region. This event is also evidenced by the increase in surface heat flux and fire spread rate beginning around the same time. In all three simulations, the increased spread and subsequent rise in fire intensity leads to stronger convection, as shown in Fig. 4.7d,e,f. Interestingly, WFA sees stronger vertical motion than SMK. Higher-level horizontal winds also increase during this time, as upper-level updrafts

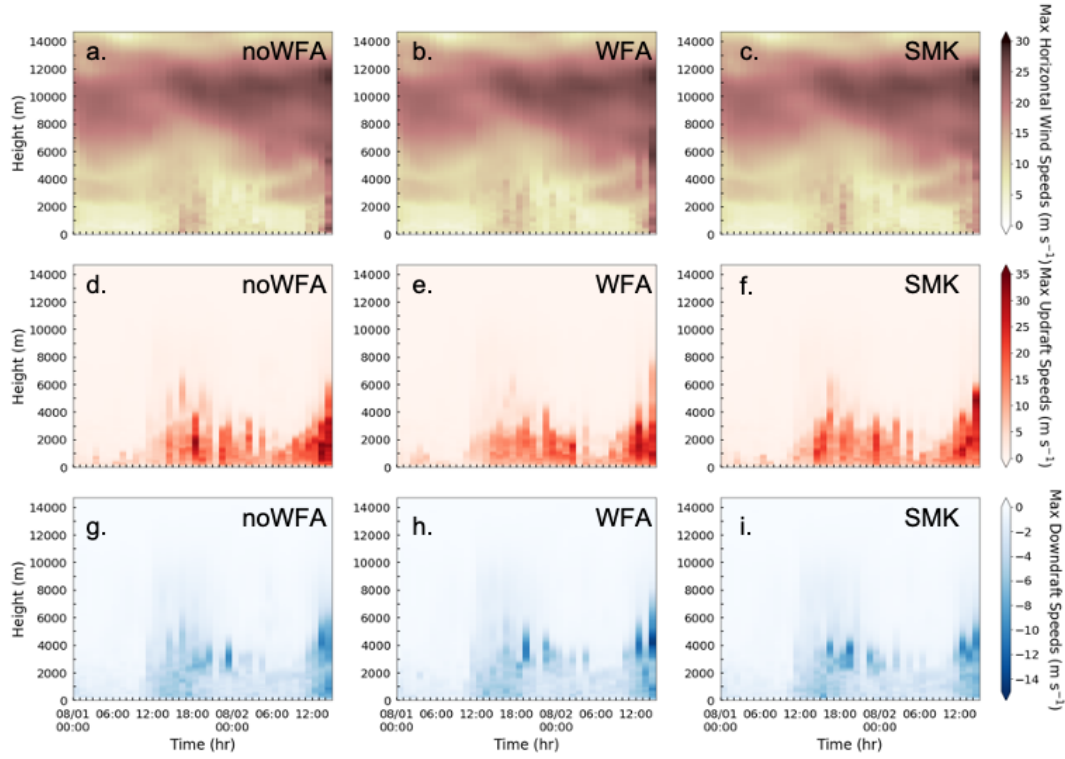


Figure 4.6: Maximum winds at each height in the domain for each hour of the simulations, beginning at 00:00 on August 1. Plots a, b, and c depict maximum horizontal wind speeds. Plots d, e, and f show maximum updraft speeds. Plots g, h, and i present maximum downdraft speeds. The left hand column (a, d, g) show results for noWFA. The center column (b, e, h) show results for WFA. The right hand column (c, f, i) show results for SMK.

draw the surrounding air into the convection column.

Focusing on the last four hours for comparison among the simulations, it is apparent that updrafts higher in the atmosphere are stronger with the aerosol-aware simulations. Because clouds form at different times for all three simulations, individual time steps themselves cannot be compared; instead, we compare time steps for each simulation where updrafts are the dominant vertical motion. The plots on the left side of Fig. 4.8 show differences in horizontal wind speeds, updrafts, and downdrafts between noWFA and WFA. Panel c shows overall stronger updraft speeds higher in the atmosphere for WFA as compared with noWFA at the end of the simulation when cloud development escalates. Additionally, horizontal wind speeds higher in the atmosphere are greater

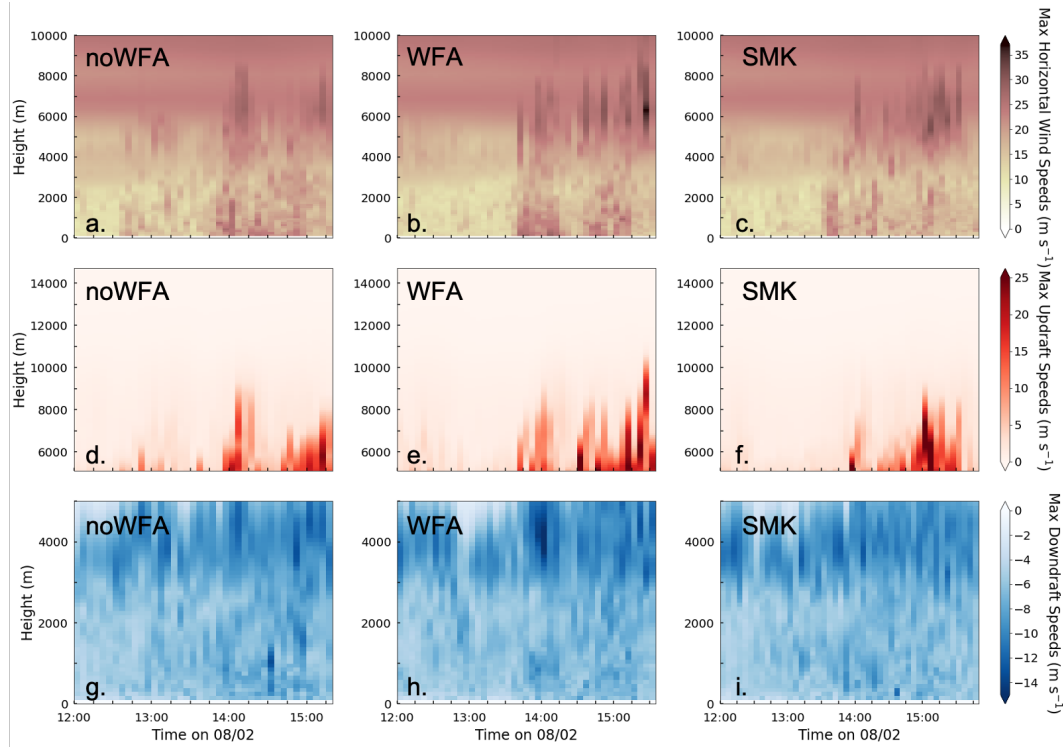


Figure 4.7: Maximum winds at each height in the domain for the last four hours of the simulations, beginning at 12:00 on August 2 and plotted at 5 minute intervals. Plots a, b, and c depict maximum horizontal wind speeds. Plots d, e, and f show maximum updraft speeds. Plots g, h, and i present maximum downdraft speeds. The left hand column (a, d, g) shows results for noWFA. The center column (b, e, h) shows results for WFA. The right hand column (c, f, i) shows results for SMK.

for WFA as compared with noWFA, clarifying and verifying what is seen in Fig. 4.7.

In comparing wind speeds in WFA with those of SMK (Fig. 4.8b,d,f), some unexpected differences emerge. In general, horizontal and vertical wind speeds at higher altitudes in WFA are greater than those in SMK, indicating deeper convection, despite running with a smaller number of aerosols. One possible explanation for this phenomenon is that the fire spread for this case towards the simulations' end is notably higher than that of SMK; it therefore has a higher total heat flux (Fig. 4.5). Aerosols, then, are lofted higher into the atmosphere from the fire's sensible heat release, and consequently continue to act as CCNs at a higher altitude, increasing the depth of cloud development. The near-surface vertical velocities for WFA are indeed larger than those for

SMK at this time, and horizontal wind speeds throughout the vertical column are all faster than those for SMK, suggesting stronger inflow of surrounding air into the convection column up to 8 km and supporting this theory.

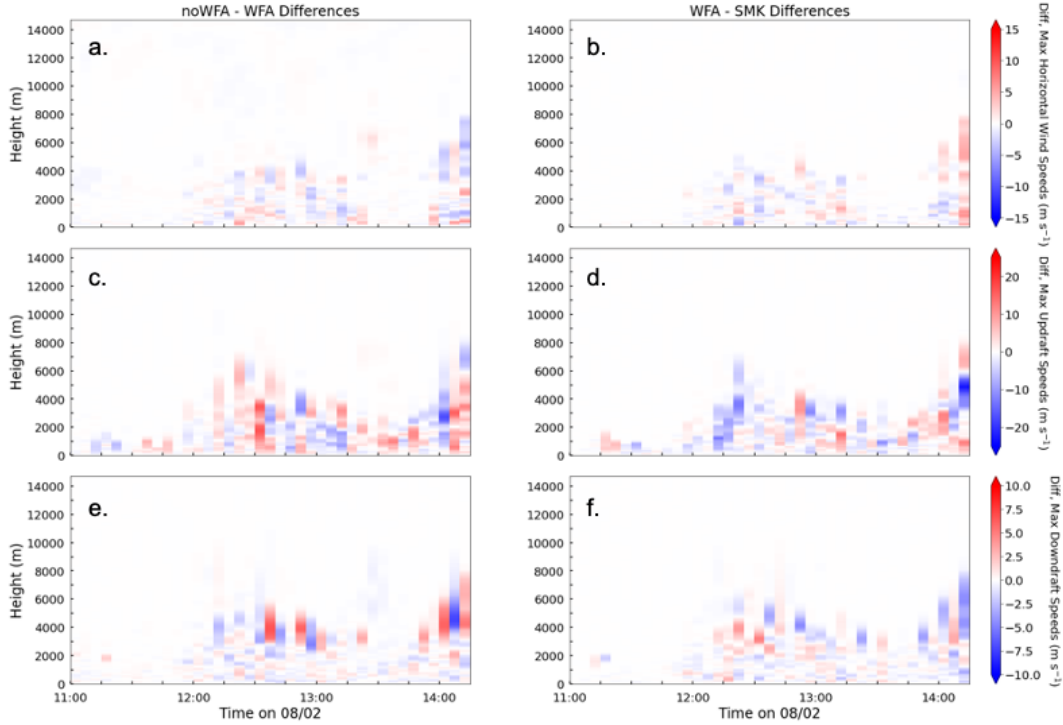


Figure 4.8: Differences in maximum winds at each height in the domain for the last four hours of the simulations, beginning at 11:00 on August 2 and plotted at 5 minute intervals. Plots a and b depict maximum horizontal wind speeds. Plots d and e show maximum updraft speeds. Plots g and h present maximum downdraft speeds. The left hand column (a, c, e) shows results for noWFA minus WFA. The right hand column (b, d, f) shows results for WFA minus SMK.

#### 4.6.2 Differences in Cloud Condensation Nuclei

The stronger heat flux beginning around 11:00 PDT in each simulation deepens convection above the fires. Cloud formation between 13:00 and simulation termination shows both liquid and solid water content increasing over this time (Fig. 4.10f). Additionally, cloud top temperatures (CTTs) begin to drop, indicating higher cloud tops and, accordingly, stronger convection (Fig. 4.9). As the fire spread rate for noWFA accelerates shortly before 14:00, it follows that CTTs in

this simulation see a local minimum shortly after 14:00. Notably, despite having a greater overall sensible heat flux (Fig. 4.5) and a sharper increase in the rate of fire area spread (Fig. 4.4d) than WFA and, in particular, SMK, noWFA sees higher CTTs near the end of the simulations.

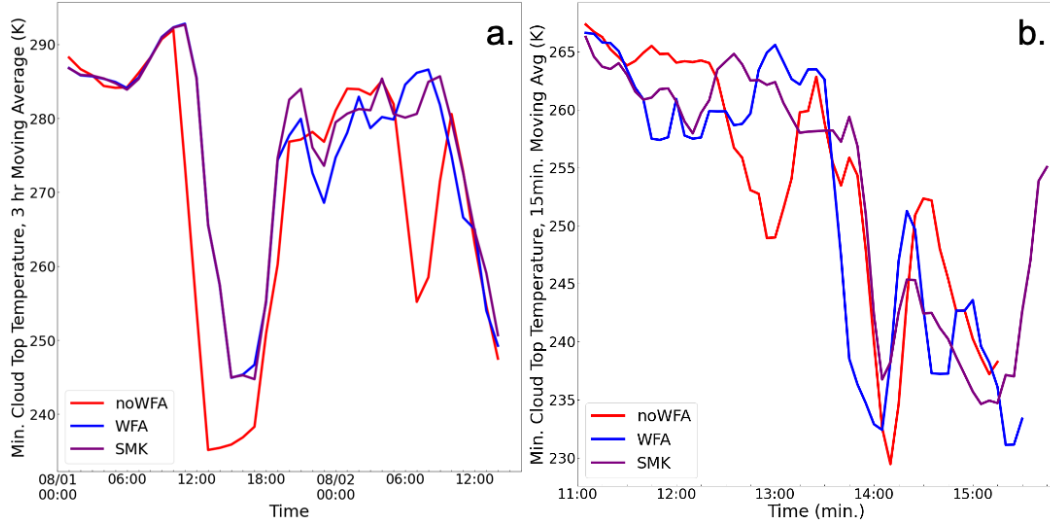


Figure 4.9: Time series of cloud top temperature for all three simulations, from ignition to termination (a), and for the last four hours of the simulation (b). CTTs are plotted with a rolling 15-minute average.

Initially, the cloud formation patterns follow the rate of fire spread (cold clouds have a slight delay), with peaks for all three simulations occurring just after 13:30 (Fig. 4.4). However, despite having a generally lower rate of spread in the last four hours than noWFA, both WFA and SMK form a greater amount of ice, snow, and cloud water during the final hours as the heat flux rises, lofting a greater concentration of aerosols higher in the atmosphere. And, because the heat flux is correlated with the fire spread rate, which for these two cases is roughly the same, we can infer that this addition of more CCNs promotes a greater amount of condensation, forming cloud drops, some of which rise and coalesce into ice formed due to the presence of water-friendly aerosols. Looking further and comparing SMK with WFA, we can see that despite a slower fire spread (Fig. 4.4d), a lower heat flux (Fig. 4.5), and weaker updrafts (Fig. 4.8d), SMK still generates comparable amounts of cloud water, ice, and snow. This trend may also be attributed to the relatively higher



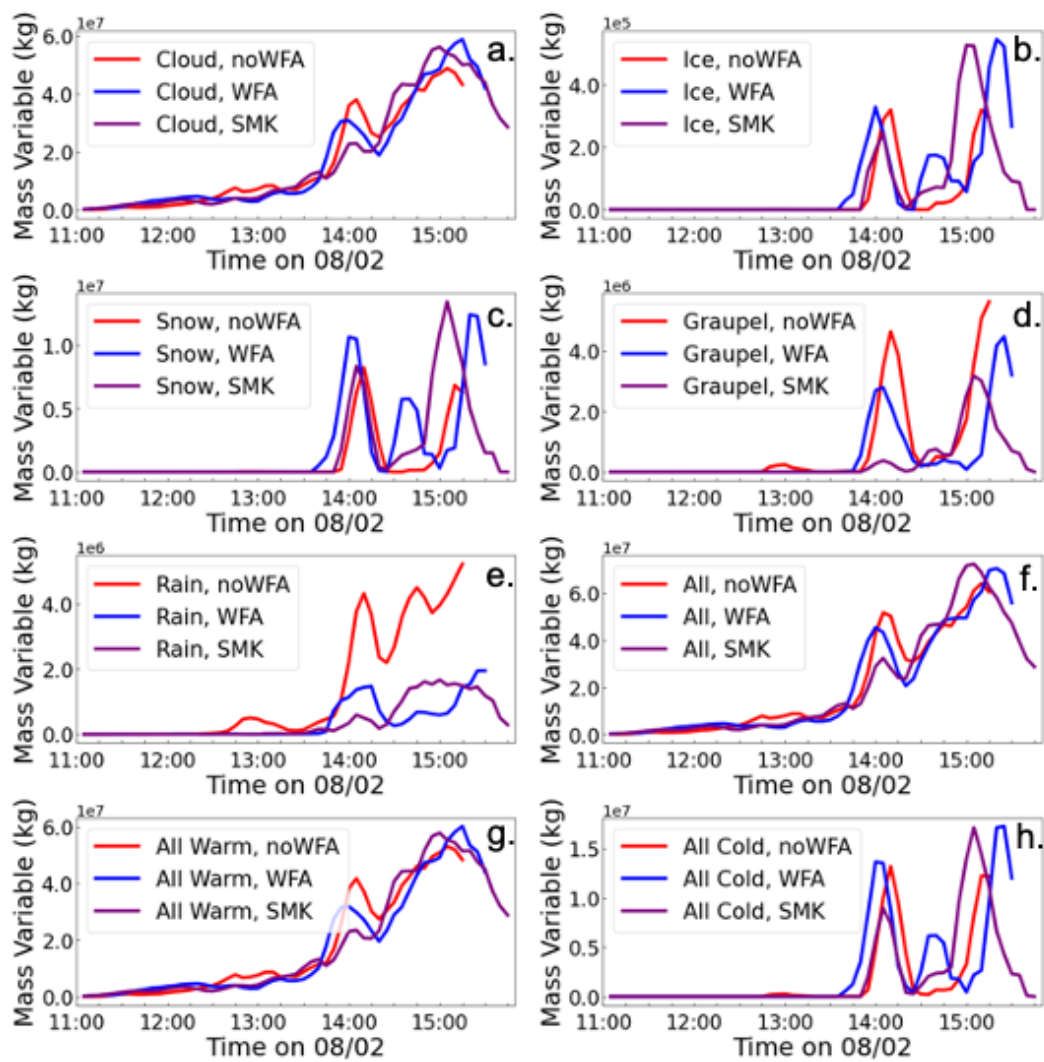


Figure 4.10: Time series of total liquid and solid water mass in the domain, for the last four hours of the simulation, broken out into cloud water (a), ice (b), snow(c), graupel (d), rain (e), and all summed together (f). The time series are plotted with a rolling 15-minute average.

number of CCNs for the SMK simulation.

The water-friendly aerosol simulations, having more CCNs than noWFA, develop an overall greater amount of warm and cold cloud water than noWFA as the surface sensible heat flux strengthens (Fig. 4.10a,b). In particular, they have a notably larger amount of cold cloud mass (Fig. 4.10h), due to stronger convection and/or less precipitation aloft. Snow concentrations are higher in WFA, although graupel is more prevalent in noWFA, where accretion is more efficient



due to decreased convective activity and generally larger cloud droplets. NoWFA also sees more droplets develop into rain than the other two simulations, as there are fewer CCNs present (Fig. 4.10d,e) and cloud drops can more easily grow to precipitable sizes. Similarly, between the two water-friendly aerosol cases, WFA has more graupel development compared with SMK, again indicating a higher rate of particle growth through accretion due to the presence of fewer CCNs and INs (Fig. 4.10d). Looking at particle count instead of mass, the same trend is evident. NoWFA has a greater number of rain droplets, while WFA and SMK have a higher number of ice particles (Fig. 4.11b).

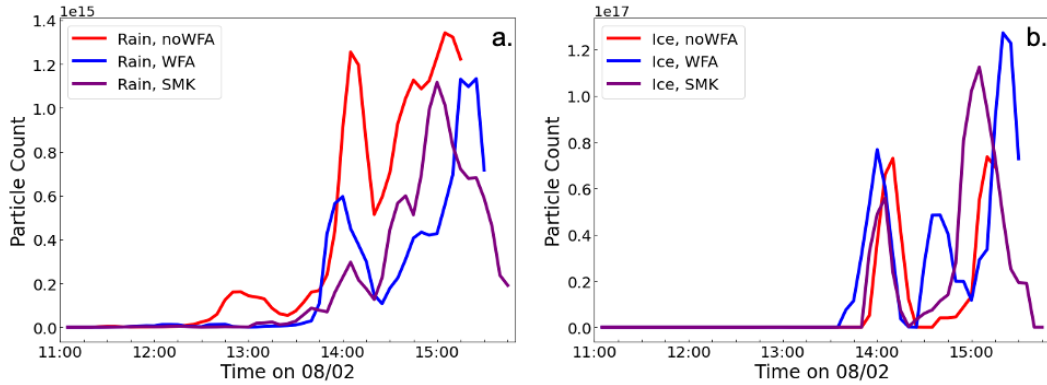


Figure 4.11: Time series of (a) rain and (b) ice particles in the domain, for the last four hours of the simulation. The time series are plotted with a rolling 15-minute average.

Smoke lofting among the three simulations is comparable (Fig. 4.12). The amount of smoke introduced into the domain is a direct result of burn area, so the total smoke and smoke in the boundary layer (below 3 km) follows the fire area trend. However, smoke lofted higher in the atmosphere is no longer an immediate function of the fire area, but instead is also determined by the surface sensible heat flux and the dynamics and microphysics of the free troposphere. Accordingly, WFA and SMK loft more smoke above 6km as their fire spread rates increase. Of the three simulations, SMK has the greatest smoke rising above 6 km at any point in the simulation—which happens just before 15:00. This is also the time when ice and snow are at a maximum for this case.

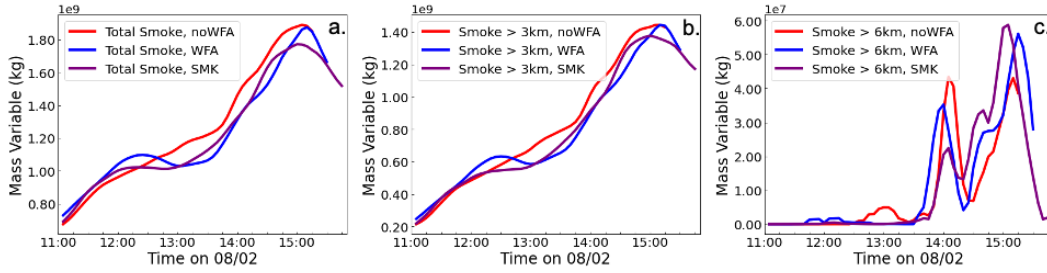


Figure 4.12: Time series of (a) total smoke, (b) smoke lofted above 3km (estimated average boundary layer height), and (c) smoke lofted about 6km, for the last four hours of the simulation. The time series are plotted with a rolling 15-minute average.

## 4.7 Conclusions

In this study, we have used WRF-Fire to simulate a fire that occurred in Northern California during the summer of 2014. PyroCu and pyroCb were observed to have formed above this fire during its second day of burning, when mid-tropospheric moisture advected into the region. We ran three simulations, each with different microphysics, and compared their results. Overall we find that the inclusion of a water-friendly aerosol option (that is, a parameterization that considers the effects of environmental aerosols on cloud development), by introducing more CCNs, results in cloud formation above the fires that has more cold cloud mass and less rain and graupel. We also find that this type of parameterization impacts the atmospheric dynamics—here, such that the fire spread slows compared with the case that does not consider aerosol-atmosphere interactions due to the strength of local circulations and convergence. This effect in turn directly influences the fire’s heat flux and, therefore, the amount of convection that occurs, which impacts cloud development.

Although we do see some deep, cold cloud development in all three simulations, none of them have a persistent pyroCb presence. This outcome may be due to the nature of what we have seen so far with the model—that a faster fire spread generates higher heat flux and, therefore, more convection. What the simulations show is contrary to what has been physically observed to fuel pyroCb: firestorms (Rosenfeld et al., 2007; M. Fromm et al., 2010b). Firestorms are mostly station-

ary blazes that are powerful enough to form their own wind systems by drawing in surrounding air to fuel their combustion. The inflowing winds prevent rapid spread (Carrier, Fendell, & Feldman, 1983). It is unknown whether or not WRF-Fire can sustain stationary burn rates that could generate firestorm behavior, because the Rothermal rate-of-spread algorithm employed in WRF-Fire is designed for wind-driven fires and is therefore uncoupled with the atmosphere.

Our findings further support those of Luderer et al. (2006) and Trentmann et al. (2006). As the sensible heat flux of WFA and SMK increases towards the end of their run times, they both see stronger convection at the surface. This increase in fire intensity coincides with the advection of mid-tropospheric water vapor, at around the 350 mb level, into the region. These two events, together, not only seed pyroCu, they also induce deeper cloud development than that of noWFA, as has been shown. This contrast indicates that despite the elevated moisture flux from vegetation combustion, upper level moisture is still necessary for deeper convection above a wildfire to occur. Consequently, we can conclude that the moisture flux released from vegetation alone is not enough to seed pyroCu and pyroCb development. Additionally, because more convective clouds did not form immediately upon the introduction of moist mid-tropospheric air into the region, but rather developed once the heat flux increased, we can also infer that the higher sensible heat release rate is also necessary for pyroCu to develop.

There remain many open avenues for continued research in this WRF-based case study. First, while all three simulations presented begin to see deeper, stronger convection around 3pm, more robust cloud growth may require additional time to further develop and persist beyond 15:00-16:00 PDT. Consequently, future work should incorporate a larger inner domain that would permit the fires to burn and clouds to form through the rest of the day and into the evening. Further, the introduction of subgrid-scale clouds may also assist with pyroCu development, as they would account for any uncaptured moisture (e.g. relative humidity dropping from an expected 100% to 95-99%) resulting from coarser vertical resolution at higher levels. The rapid spread of the fire on the second day—well beyond what was observed—is indicative of how much the local winds and atmospheric dynamics can influence fire behavior in the model. To best improve the model's

ability to successfully reproduce firestorm behavior, therefore, it should be restructured to include full fire-atmosphere coupling.

## 4.8 Acknowledgements

Many thanks to Dr. Branko Kosović and Dr. Timothy Juliano from the National Center for Atmospheric Research (NCAR) for their guidance and assistance with WRF model setup using the Thompson Aerosol-Aware scheme.

Funding for this study has been provided by the Open Philanthropy Project. This work was authored [in part] by the National Renewable Energy Laboratory, operated by Alliance for Sustainable Energy, LLC, for the U.S. Department of Energy (DOE) under Contract No. DE-AC36-08GO28308. Funding provided by the U.S. Department of Energy Office of Energy Efficiency and Renewable Energy Wind Energy Technologies Office. The views expressed in the article do not necessarily represent the views of the DOE or the U.S. Government. The U.S. Government retains and the publisher, by accepting the article for publication, acknowledges that the U.S. Government retains a nonexclusive, paid-up, irrevocable, worldwide license to publish or reproduce the published form of this work, or allow others to do so, for U.S. Government purposes.

This work utilized resources from the University of Colorado Boulder Research Computing Group, which is supported by the National Science Foundation (awards ACI-1532235 and ACI-1532236), the University of Colorado Boulder, and Colorado State University.

<b>WRF Parameter</b>	<b>d01</b>	<b>d02</b>	<b>d03</b>
Horizontal Resolution	3 km	1 km	100 m
Horizontal Extent (Grid Cells)	240 x 240	241 x 241	501 x 501
Number of Vertical Levels	80		
Model Top	100 mb		
Lowest Vertical Level	60 m		
Time Step	5 s	1.67 s	0.167
Time Integration Scheme	Runge-Kutta 3rd Order		
Planetary Boundary Layer Scheme	MYNN	MYNN	-
Surface Layer Scheme	Revised MM5 Monin-Obukhov Similarity Theory		
Eddy Coefficient Option	Horizontal Smagorinsky 1st order closure		1.5-order SGS TKE
Land Surface Model	Unified Noah Land-Surface Model		
SW & LW Radiation Scheme	RRTMG		
Microphysics Scheme	Thompson or Thompson with Aerosol-awareness		
Damping	Vertical velocity damping & upper-level Rayleigh layer of $0.2 \text{ s}^{-1}$ with a depth of 6 km		
Advection Options	Positive-definite moisture and scalar advection		
Fire Grid Mesh	-	-	4:1
Height of Winds Driving Fire Spread	-	-	2.5 m
Ignition Area	-	-	50 m
Specified Ignition Time	-	-	300 s

Table 4.1: WRF Model Setup

Simulation Name	Microphysics Used
noWFA	Thompson
WFA	Thompson with Water-Friendly Aerosols (TWFA)
SMK	TWFA with additional aerosols from fire combustion

Table 4.2: Simulation reference names and microphysics used in each.

## Chapter 5

### Conclusions

#### 5.1 Summary of Findings

This dissertation has explored several modeling applications relevant to ways we can address climate change. The studies presented here have examined one tool to assist with wind energy forecasting (CO<sub>2</sub> mitigation) and evaluated smoke plume and pyrocumulus behavior to better our understanding of the threats presented by large fires (adaptation to climate change). A summary of the findings is presented below.

##### 5.1.1 Inclusion of the Rotor-Equivalent Wind Speed in the WRF WFP

In Chapter 2, we assessed the addition of a new physics option to the WRF Wind Farm Parameterization. Currently, the parameterization uses the hub height wind speed in the wind power equation to calculate the power output from each turbine being modeled. However, in high wind shear situations, this assumption may not accurately represent the full wind field driving turbine rotation. Instead of presuming the winds at a single height determine projected energy output, the rotor-equivalent wind speed (REWS) option takes a weighted average of the winds across the rotor-swept area, also considering wind direction, and uses that instead.

We ran a series of simulations in an idealized domain to develop an understanding of how this change may affect forecasting results. We found that, for most conditions, the introduction of the REWS does not present significant differences in waking or TKE generation when compared with the WFP using hub height wind speed. Because the change in winds according to the wind profile

law is more or less linear when considered over the vertical extent of current rotor swept areas, a weighted average calculation of the wind speed introduces only minor differences compared with the hub height wind speed. However, the overall impact of this revision on farm production, when calculated in terms of total power output and financial loss or gain, is not negligible. Even a small percentage difference in power output for one turbine, when scaled across an entire installation, can equate to a difference in \$226,000 of forecasted revenue over the course of a year, assuming a levelized cost of energy (LCOE) of 43\$ MWh<sup>-1</sup> and a 10 x 10 farm with 2 MW turbines in operation, each having a capacity factor of 30%.

Although the REWS introduces only slight atmospheric disparities in model forecasts for the most common wind profiles in the boundary layer, there are a few situations that generate non-linear wind shear low enough to intercept the turbine area. In this study, we tested our physics edits using a wind profile based on a cold pool mix-out that occurred in the Columbia River Gorge during the Wind Forecast Improvement Project 2 (WFIP2) observational campaign. As a layer of gusty air begins to erode a calm cold pool below it, moving lower as it mixes in, a large amount of wind speed and directional shear is introduced at heights intersecting the turbine swept area. We found that wind shear of this order can introduce more serious differences into the model. Most importantly, at lower wind speeds, using the REWS instead of the hub height wind speed during an event like this mix-out can make the difference between whether or not the turbines are considered operational in the model. This, in turn, affects both power and atmospheric forecasting.

### **5.1.2 Smoke Lofting Sensitivity to Local Weather Conditions**

Chapter 3 pivoted away from wind farm modeling and began to explore the behavior and consequences of large fires. In this study, we examined how the smoke plume of an areal-lit fire responds to various atmospheric circumstances, using the fire parameterization in WRF (WRF-Fire). Previous observational research has shown that powerful fires can inject smoke into the upper troposphere and lower stratosphere (UTLS), and climate modeling studies have indicated that if enough smoke lofts this high, it could have long residence times (months to years) and



widespread climatic effects. Earlier modeling studies have also shown that UTLS plume injection is sensitive to horizontal winds, thermal stability, fuel source density, and atmospheric humidity. We have verified the majority of these findings with our own, and have also presented an indication of which factor is the most important.

We simulated 20 large fires in an idealized domain. Each case had one variant adjusted—wind speeds, relative humidity (RH), or boundary layer stability—and their resultant vertical smoke profiles, following an areal ignition and a total burn time of 90 minutes each, were compared. We found that moisture has the most substantial effect on lofting, with the amount of smoke reaching the UTLS increasing with higher RH. Wind speeds, too, affect plume rise. Higher wind speeds tend to dampen vertical motion higher in the atmosphere, as the plume is mixed out where the convection column starts to weaken. These findings corroborate work that had been done during the Cold War era.

When compared, the moisture influence on smoke injection height trumps that of winds. Vertical velocities, which correlate with horizontal wind speeds, have a linear relationship with smoke lofted into the UTLS. That relationship is disrupted, however, by moisture presence. Conversely, the relationship between CAPE (a metric influenced by relative humidity) and smoke lofting is not disturbed by strong winds. We can conclude, therefore, that moisture effects are more instrumental to plume rise.

### **5.1.3 PyroCu and PyroCb Development in WRF with and without WFA**

In Chapter 4, we continued to examine atmosphere-fire interactions in models by simulating a fire that had burned in Northern California in the summer of 2014. Other studies have shown that the deep convection that forms via pyroconvulonimbi is often a transport mechanism for wildfire smoke into the UTLS. Being able to effectively model pyroCb, therefore, is a key tool in being able to better understand these events that are still not well-understood.

We ran the simulation three different times, with three different microphysics setups. In the first simulation, we used standard Thompson microphysics. In the second simulation, we ran

with the aerosol-aware Thompson scheme, and in the third simulation, we also considered aerosols generated by combustion alongside the aerosol-aware Thompson scheme. All cases treated smoke as a passive tracer, which was advected by atmospheric dynamics but did not interact with anything.

We found that the addition of the aerosol coupling resulted in more cloud development but less precipitation, as compared with the non-coupled case because of the increase in cloud condensation nuclei (CCNs). Additionally, because of this, more water overall is activated, resulting in a greater amount of latent heat release and more cold cloud content in the form of snow and ice. Because the simulations terminated in the mid-afternoon due to the fire hitting the domain boundary, future work will include extending the size of the domain and running a sensitivity analysis on input parameters for fire spread, so that the fire can run through the end of its second day.

## References

- Abatzoglou, J. T., Williams, A. P., & Barbero, R. (2019). Global Emergence of Anthropogenic Climate Change in Fire Weather Indices. Geophysical Research Letters, 46(1), 326–336. (eprint: <https://agupubs.onlinelibrary.wiley.com/doi/pdf/10.1029/2018GL080959>) doi: <https://doi.org/10.1029/2018GL080959>
- Adger, W. N., Pulhin, J. M., Barnett, J., Dabelko, G. D., Hovelsrud, G. K., Levy, M., ... Leichenko, R. (2014). Human security. Climate Change 2014: Impacts, Adaptation, and Vulnerability. Part A: Global and Sectoral Aspects. Contribution of Working Group II to the Fifth Assessment Report of the Intergovernmental Panel on Climate Change, 37.
- Administration, U. E. I. (2017). Frequently Asked Questions (FAQs) - U.S. Energy Information Administration (EIA). Retrieved from <https://www.eia.gov/tools/faqs/faq.php> (Library Catalog: [www.eia.gov](http://www.eia.gov))
- Allaerts, D., & Meyers, J. (2018, February). Gravity Waves and Wind-Farm Efficiency in Neutral and Stable Conditions. Boundary-Layer Meteorology, 166(2), 269–299. doi: 10.1007/s10546-017-0307-5
- Allen, C. D., Macalady, A. K., Chenchouni, H., Bachelet, D., McDowell, N., Vennetier, M., ... others (2010). A global overview of drought and heat-induced tree mortality reveals emerging climate change risks for forests. Forest ecology and management, 259(4), 660–684.
- American Meteorological Society. (2013). Pyrocumulonimbus - AMS Glossary.
- Anderson, H. E. (1982a). Aids to determining fuel models for estimating fire behavior (Tech. Rep. No. INT-GTR-122). Ogden, UT: U.S. Department of Agriculture, Forest Service, Intermountain Forest and Range Experiment Station. doi: 10.2737/INT-GTR-122
- Anderson, H. E. (1982b). Aids to determining fuel models for estimating fire behavior (Tech. Rep. No. INT-GTR-122). Ogden, UT: U.S. Department of Agriculture, Forest Service, Intermountain Forest and Range Experiment Station. doi: 10.2737/INT-GTR-122
- Arms Control Association. (2019). Nuclear Weapons: Who Has What at a Glance.
- Armstrong, A., Burton, R. R., Lee, S. E., Mobbs, S., Ostle, N., Smith, V., ... Whitaker, J. (2016, April). Ground-level climate at a peatland wind farm in Scotland is affected by wind turbine operation. Environmental Research Letters, 11(4), 044024. doi: 10.1088/1748-9326/11/4/044024

- Ayodele, T. R., Jimoh, A. A., Munda, J. L., & Agee, J. T. (2012). Challenges of Grid Integration of Wind Power on Power System Grid Integrity: A Review. , 9.
- Badlan, R., Sharples, J., Evans, J., & McRae, R. (2017). The role of deep flaming in violent pyroconvection. , 3–8.
- Baek, S. (2017). A revised radiation package of G-packed McICA and two-stream approximation: Performance evaluation in a global weather forecasting model. Journal of Advances in Modeling Earth Systems, 9(3), 1628–1640. doi: 10.1002/2017MS000994
- Baidya Roy, S. (2004). Can large wind farms affect local meteorology? Journal of Geophysical Research, 109(D19). doi: 10.1029/2004JD004763
- Baidya Roy, S. (2011, April). Simulating impacts of wind farms on local hydrometeorology. Journal of Wind Engineering and Industrial Aerodynamics, 99(4), 491–498. doi: 10.1016/j.jweia.2010.12.013
- Baidya Roy, S., & Traiteur, J. J. (2010, October). Impacts of wind farms on surface air temperatures. Proceedings of the National Academy of Sciences, 107(42), 17899–17904. doi: 10.1073/pnas.1000493107
- Banta, R., Newsom, R. K., Lundquist, J. K., Pichugina, Y. L., Coulter, R. L., & Mahrt, L. (2002, November). Nocturnal Low-Level Jet Characteristics Over Kansas During Cases-99. Boundary-Layer Meteorology, 105(2), 221–252. doi: 10.1023/A:1019992330866
- Banta, R. M., Mahrt, L., Vickers, D., Sun, J., Balsley, B. B., Pichugina, Y. L., & Williams, E. J. (2007, September). The Very Stable Boundary Layer on Nights with Weak Low-Level Jets. Journal of the Atmospheric Sciences, 64(9), 3068–3090. doi: 10.1175/JAS4002.1
- Barthelmie, R. J., Pryor, S. C., Wildmann, N., & Menke, R. (2018, June). Wind turbine wake characterization in complex terrain via integrated Doppler lidar data from the Perdigão experiment. Journal of Physics: Conference Series, 1037, 052022. Retrieved 2020-09-28, from <https://doi.org/10.1088/1742-6596/1037/5/052022> (Publisher: IOP Publishing) doi: 10.1088/1742-6596/1037/5/052022
- Beebe, R. G., & Bates, F. C. (1955, January). A MECHANISM FOR ASSISTING IN THE RELEASE OF CONVECTIVE INSTABILITY. Monthly Weather Review, 83(1), 1–10. (Publisher: American Meteorological Society) doi: 10.1175/1520-0493(1955)083<0001:AMFAIT>2.0.CO;2
- Benjamin, S. G., Weygandt, S. S., Brown, J. M., Hu, M., Alexander, C. R., Smirnova, T. G., . . . Manikin, G. S. (2016, April). A North American Hourly Assimilation and Model Forecast Cycle: The Rapid Refresh. Monthly Weather Review, 144(4), 1669–1694. doi: 10.1175/MWR-D-15-0242.1
- Berleemann, M., & Steinhardt, M. F. (2017, December). Climate Change, Natural Disasters, and Migration—a Survey of the Empirical Evidence. CESifo Economic Studies, 63(4), 353–385. (Publisher: Oxford Academic) doi: 10.1093/cesifo/ixf019
- Blaabjerg, F., & Ke Ma. (2013, September). Future on Power Electronics for Wind Turbine Systems. IEEE Journal of Emerging and Selected Topics in Power Electronics, 1(3), 139–152.

doi: 10.1109/JESTPE.2013.2275978

- Blahak, U., GbR, W.-J., & Meis, J. (2010). A Simple Parameterization of Drag Forces Induced by Large Wind Farms for Numerical Weather Prediction Models. , 8.
- Boer, M. M., Resco de Dios, V., & Bradstock, R. A. (2020, March). Unprecedented burn area of Australian mega forest fires. Nature Climate Change, 10(3), 171–172. Retrieved 2020-09-26, from <https://www.nature.com/articles/s41558-020-0716-1> (Number: 3 Publisher: Nature Publishing Group) doi: 10.1038/s41558-020-0716-1
- Bonner, W. D. (1968, December). CLIMATOLOGY OF THE LOW LEVEL JET. Monthly Weather Review, 96(12), 833–850. doi: 10.1175/1520-0493(1968)096<0833:COTLLJ>2.0.CO;2
- Brasseur, G. P., & Solomon, S. (2006). Aeronomy of the Middle Atmosphere: Chemistry and Physics of the Stratosphere and Mesosphere. Springer Science & Business Media.
- Carrier, G., Fendell, F., & Feldman, P. (1983). Criteria for onset of firestorms. In Proceedings, 17th asilomar conference on fire and blast effects of nuclear weapons (pp. 60–65).
- Chen, F., & Dudhia, J. (2001, April). Coupling an Advanced Land Surface-Hydrology Model with the Penn State-NCAR MM5 Modeling System. Part I: Model Implementation and Sensitivity. Monthly Weather Review, 129(4), 569–585. (Publisher: American Meteorological Society) doi: 10.1175/1520-0493(2001)129<0569:CAALSH>2.0.CO;2
- Chen, S.-h., & Dudhia, J. (2000). Annual Report: WRF PHYSICS. , 39.
- Choukulkar, A., Pichugina, Y., Clack, C. T. M., Calhoun, R., Banta, R., Brewer, A., & Hardesty, M. (2016, August). A new formulation for rotor equivalent wind speed for wind resource assessment and wind power forecasting: New formulation for equivalent wind speed. Wind Energy, 19(8), 1439–1452. doi: 10.1002/we.1929
- Churchfield, M., Lee, S., Moriarty, P., Martinez, L., Leonardi, S., Vijayakumar, G., & Brasseur, J. (2012). A Large-Eddy Simulation of Wind-Plant Aerodynamics. In 50th AIAA Aerospace Sciences Meeting including the New Horizons Forum and Aerospace Exposition. American Institute of Aeronautics and Astronautics. Retrieved 2020-09-28, from <https://arc.aiaa.org/doi/abs/10.2514/6.2012-537> doi: 10.2514/6.2012-537
- Clack, C. T. M., Alexander, A., Choukulkar, A., & MacDonald, A. E. (2016, September). Demonstrating the effect of vertical and directional shear for resource mapping of wind power: Demonstrating the effect of vertical and directional shear for resource mapping of wind power. Wind Energy, 19(9), 1687–1697. doi: 10.1002/we.1944
- Clark, T. L., Coen, J., & Latham, D. (2004). Description of a coupled atmosphere - fire model. International Journal of Wildland Fire, 13(1), 49. doi: 10.1071/WF03043
- Clements, C. B., Lareau, N. P., Kingsmill, D. E., Bowers, C. L., Camacho, C. P., Bagley, R., & Davis, B. (2018, June). The Rapid Deployments to Wildfires Experiment (RaDFIRE): Observations from the Fire Zone. Bulletin of the American Meteorological Society, 99(12), 2539–2559. doi: 10.1175/BAMS-D-17-0230.1

- Coen, J. L., Cameron, M., Michalakes, J., Patton, E. G., Riggan, P. J., & Yedinak, K. M. (2013a). WRF-Fire: Coupled Weather-Wildland Fire Modeling with the Weather Research and Forecasting Model. *Journal of Applied Meteorology and Climatology*, *52*(1), 16–38. doi: 10.1175/JAMC-D-12-023.1
- Coen, J. L., Cameron, M., Michalakes, J., Patton, E. G., Riggan, P. J., & Yedinak, K. M. (2013b, January). WRF-Fire: Coupled Weather-Wildland Fire Modeling with the Weather Research and Forecasting Model. *Journal of Applied Meteorology and Climatology*, *52*(1), 16–38. doi: 10.1175/JAMC-D-12-023.1
- Cotton, W. R. (1985). Atmospheric Convection and Nuclear Winter: A new simulation of a large urban firestorm shows how smoke and soot might enter the stratosphere and alter the earth's climate. *American Scientist*, *73*(3), 275–280.
- Countryman, C. M. (1964). *Mass fires and fire behavior* (Tech. Rep. No. RS-RP-19). Berkeley, CA: Pacific Southwest Forest and Range Experiment Station, Forest Service, US Department of Agriculture.
- Coupe, J., Bardeen, C. G., Robock, A., & Toon, O. B. (2019a). Nuclear Winter Responses to Nuclear War Between the United States and Russia in the Whole Atmosphere Community Climate Model Version 4 and the Goddard Institute for Space Studies ModelE. *Journal of Geophysical Research: Atmospheres*, *124*(15), 8522–8543. Retrieved 2020-01-30, from <https://agupubs.onlinelibrary.wiley.com/doi/abs/10.1029/2019JD030509> doi: 10.1029/2019JD030509
- Coupe, J., Bardeen, C. G., Robock, A., & Toon, O. B. (2019b). Nuclear Winter Responses to Nuclear War Between the United States and Russia in the Whole Atmosphere Community Climate Model Version 4 and the Goddard Institute for Space Studies ModelE. *Journal of Geophysical Research: Atmospheres*, *124*(15). doi: 10.1029/2019JD030509
- Covey, C., Schneider, S. H., & Thompson, S. L. (1984). Global atmospheric effects of massive smoke injections from a nuclear war: Results from general circulation model simulations. *Nature*, *308*(5954), 21–25.
- Crutzen, P. J., & Birks, J. W. (1982). The Atmosphere after a Nuclear War: Twilight at Noon. *Ambio*, *11*(2/3), 114–125.
- Cunningham, P., & Reeder, M. J. (2009). Severe convective storms initiated by intense wildfires: Numerical simulations of pyro-convection and pyro-tornadogenesis. *Geophysical Research Letters*, *36*(12). Retrieved 2020-06-03, from <https://agupubs.onlinelibrary.wiley.com/doi/abs/10.1029/2009GL039262> (eprint: <https://agupubs.onlinelibrary.wiley.com/doi/pdf/10.1029/2009GL039262>) doi: 10.1029/2009GL039262
- EIA. (2013). *Few transportation fuels surpass the energy densities of gasoline and diesel - Today in Energy - U.S. Energy Information Administration (EIA)*. Retrieved 2020-09-28, from <https://www.eia.gov/todayinenergy/detail.php?id=9991>
- EIA. (2020a). *Electricity generation from wind - U.S. Energy Information Administration (EIA)*. Retrieved 2020-09-28, from <https://www.eia.gov/energyexplained/wind/electricity>

-generation-from-wind.php

- EIA. (2020b). Frequently Asked Questions (FAQs) - U.S. Energy Information Administration (EIA). Retrieved 2020-09-28, from <https://www.eia.gov/tools/faqs/faq.php?id=73&t=11>
- Ek, M. B., Mitchell, K. E., Lin, Y., Rogers, E., Grunmann, P., Koren, V., ... Tarpley, J. D. (2003). Implementation of Noah land surface model advances in the National Centers for Environmental Prediction operational mesoscale Eta model. Journal of Geophysical Research: Atmospheres, 108(D22). doi: 10.1029/2002JD003296
- Fernando, H. J. S., Mann, J., Palma, J. M. L. M., Lundquist, J. K., Barthelmie, R. J., Belo-Pereira, M., ... Wang, Y. (2019, May). The Perdigo: Peering into Microscale Details of Mountain Winds. Bulletin of the American Meteorological Society, 100(5), 799–819. Retrieved 2020-09-28, from <https://journals.ametsoc.org/bams/article/100/5/799/344800/The-Perdigao-Peering-into-Microscale-Details-of> (Publisher: American Meteorological Society) doi: 10.1175/BAMS-D-17-0227.1
- Fitch, A. C. (2015, August). Climate Impacts of Large-Scale Wind Farms as Parameterized in a Global Climate Model. Journal of Climate, 28(15), 6160–6180. doi: 10.1175/JCLI-D-14-00245.1
- Fitch, A. C. (2016, September). Notes on using the mesoscale wind farm parameterization of Fitch *et al.* (2012) in WRF: Notes on using the mesoscale wind farm parameterization of Fitch *et al.* (2012) in WRF. Wind Energy, 19, 1757–1758. doi: 10.1002/we.1945
- Fitch, A. C., Lundquist, J. K., & Olson, J. B. (2013, July). Mesoscale Influences of Wind Farms throughout a Diurnal Cycle. Monthly Weather Review, 141(7), 2173–2198. doi: 10.1175/MWR-D-12-00185.1
- Fitch, A. C., Olson, J. B., Lundquist, J. K., Dudhia, J., Gupta, A. K., Michalakes, J., & Barstad, I. (2012, September). Local and Mesoscale Impacts of Wind Farms as Parameterized in a Mesoscale NWP Model. Monthly Weather Review, 140(9), 3017–3038. doi: 10.1175/MWR-D-11-00352.1
- Fitch, A. C., Olson, J. B., Lundquist, J. K., Dudhia, J., Gupta, A. K., Michalakes, J., ... Archer, C. L. (2013, April). CORRIGENDUM. Monthly Weather Review, 141(4), 1395–1395. doi: 10.1175/MWR-D-12-00341.1
- Flannigan, M. D., Stocks, B. J., & Wotton, B. M. (2000, November). Climate change and forest fires. Science of The Total Environment, 262(3), 221–229. doi: 10.1016/S0048-9697(00)00524-6
- Frame, D. J., Rosier, S. M., Noy, I., Harrington, L. J., Carey-Smith, T., Sparrow, S. N., ... Dean, S. M. (2020, September). Climate change attribution and the economic costs of extreme weather events: a study on damages from extreme rainfall and drought. Climatic Change, 162(2), 781–797. doi: 10.1007/s10584-020-02729-y
- Freitas, S. R., Longo, K. M., Chatfield, R., Latham, D., Silva Dias, M. a. F., Andreae, M. O., ... Carvalho Jr., J. A. (2007, July). Including the sub-grid scale plume rise of vegetation fires in low resolution atmospheric transport models. Atmospheric Chemistry and Physics, 7(13),

- 3385–3398. (Publisher: Copernicus GmbH) doi: <https://doi.org/10.5194/acp-7-3385-2007>
- Fritsch, J. M., & Chappell, C. F. (1980, August). Numerical Prediction of Convectively Driven Mesoscale Pressure Systems. Part I: Convective Parameterization. Journal of the Atmospheric Sciences, 37(8), 1722–1733. (Publisher: American Meteorological Society) doi: 10.1175/1520-0469(1980)037<1722:NPOCDM>2.0.CO;2
- Fromm, M., Alfred, J., Hoppel, K., Hornstein, J., Bevilacqua, R., Shettle, E., . . . Stocks, B. (2000). Observations of boreal forest fire smoke in the stratosphere by POAM III, SAGE II, and lidar in 1998. Geophysical Research Letters, 27(9). doi: 10.1029/1999GL011200
- Fromm, M., Lindsey, D. T., Servranckx, R., Yue, G., Trickl, T., Sica, R., . . . Godin-Beekmann, S. (2010a). The Untold Story of Pyrocumulonimbus. Bulletin of the American Meteorological Society, 91(9), 1193–1210. doi: 10.1175/2010BAMS3004.1
- Fromm, M., Lindsey, D. T., Servranckx, R., Yue, G., Trickl, T., Sica, R., . . . Godin-Beekmann, S. (2010b, April). The Untold Story of Pyrocumulonimbus. Bulletin of the American Meteorological Society, 91(9), 1193–1210. (Publisher: American Meteorological Society) doi: 10.1175/2010BAMS3004.1
- Fromm, M., Peterson, D., & Girolamo, L. D. (2019). The Primary Convective Pathway for Observed Wildfire Emissions in the Upper Troposphere and Lower Stratosphere: A Targeted Reinterpretation. Journal of Geophysical Research: Atmospheres, 124(23). doi: 10.1029/2019JD031006
- Fromm, M., Shettle, E. P., Fricke, K. H., Ritter, C., Trickl, T., Giehl, H., . . . Deshler, T. (2008). Stratospheric impact of the Chisholm pyrocumulonimbus eruption: 2. Vertical profile perspective. Journal of Geophysical Research: Atmospheres, 113(D8). doi: 10.1029/2007JD009147
- Fromm, M., Torres, O., Diner, D., Lindsey, D., Hull, B. V., Servranckx, R., . . . Li, Z. (2008). Stratospheric impact of the Chisholm pyrocumulonimbus eruption: 1. Earth-viewing satellite perspective. Journal of Geophysical Research: Atmospheres, 113(D8). doi: 10.1029/2007JD009153
- Fromm, M., Tupper, A., Rosenfeld, D., Servranckx, R., & McRae, R. (2006). Violent pyroconvective storm devastates Australia’s capital and pollutes the stratosphere. Geophysical Research Letters, 33(5). Retrieved 2020-06-03, from <https://agupubs.onlinelibrary.wiley.com/doi/abs/10.1029/2005GL025161> doi: 10.1029/2005GL025161
- Fromm, M. D., & Servranckx, R. (2003). Transport of forest fire smoke above the tropopause by supercell convection. Geophysical Research Letters, 30(10). doi: 10.1029/2002GL016820
- Gatebe, C. K., Varnai, T., Poudyal, R., Ichoku, C., & King, M. D. (2012, June). Taking the pulse of pyrocumulus clouds. Atmospheric Environment, 52, 121–130. doi: 10.1016/j.atmosenv.2012.01.045
- Ghan, S. J., MacCracken, M. C., & Walton, J. J. (1988). Climatic response to large atmospheric smoke injections: Sensitivity studies with a tropospheric general circulation model. Journal of Geophysical Research: Atmospheres, 93(D7), 8315–8337.
- Glasstone, S., & Dolan, P. J. (1977). The Effects of Nuclear Weapons. Department of Defense.



(Google-Books-ID: s4NwjdTWqXMC)

- Griffith, D. (2018). GLOBAL WIND STATISTICS 2017. , 4.
- Haines, D. A. (1989). A lower atmosphere severity index for wildlife fires. National Weather Digest, 13, 23–27.
- Harwell, M. A., Hutchinson, T. C., Cropper Jr, W., Harwell, C. C., & Grover, H. D. (1985). Scope 28: Environmental consequences of nuclear war. volume ii. ecological and agricultural effects.
- Haupt, S. E., Kosović, B., Shaw, W., Berg, L. K., Churchfield, M., Cline, J., ... Sever, G. (2019, December). On Bridging A Modeling Scale Gap: Mesoscale to Microscale Coupling for Wind Energy. Bulletin of the American Meteorological Society, 100(12), 2533–2550. Retrieved 2020-09-27, from <https://journals.ametsoc.org/bams/article/100/12/2533/344473/On-Bridging-A-Modeling-Scale-Gap-Mesoscale-to> (Publisher: American Meteorological Society) doi: 10.1175/BAMS-D-18-0033.1
- Hersbach, H., Bell, B., Berrisford, P., Hirahara, S., Horányi, A., Muñoz Sabater, J., ... Thépaut, J.-N. (2020). The ERA5 global reanalysis. Quarterly Journal of the Royal Meteorological Society, 146(730), 1999–2049. doi: 10.1002/qj.3803
- Hoffmann, L., Genthner, G., Li, D., Stein, O., Wu, X., Griessbach, S., ... Wright, J. S. (2019, March). From ERA-Interim to ERA5: the considerable impact of ECMWF’s next-generation reanalysis on Lagrangian transport simulations. Atmospheric Chemistry and Physics, 19(5), 3097–3124. doi: 10.5194/acp-19-3097-2019
- Huggett, C. (1980). Estimation of rate of heat release by means of oxygen consumption measurements. Fire and Materials, 4(2), 61–65.
- Högström, U., Asimakopoulou, D., Kambezidis, H., Helmis, C., & Smedman, A. (1988, January). A field study of the wake behind a 2 MW wind turbine. Atmospheric Environment (1967), 22(4), 803–820. doi: 10.1016/0004-6981(88)90020-0
- Iacono, M. J., Delamere, J. S., Mlawer, E. J., Shephard, M. W., Clough, S. A., & Collins, W. D. (2008). Radiative forcing by long-lived greenhouse gases: Calculations with the AER radiative transfer models. Journal of Geophysical Research: Atmospheres, 113(D13). doi: 10.1029/2008JD009944
- Iungo, G. V., Wu, Y.-T., & Porté-Agel, F. (2013, February). Field Measurements of Wind Turbine Wakes with Lidars. Journal of Atmospheric and Oceanic Technology, 30(2), 274–287. (Publisher: American Meteorological Society) doi: 10.1175/JTECH-D-12-00051.1
- Jägermeyr, J., Robock, A., Elliott, J., Müller, C., Xia, L., Khabarov, N., ... others (2020). A regional nuclear conflict would compromise global food security. Proceedings of the National Academy of Sciences, 117(13), 7071–7081.
- Janháall, S., Andreae, M. O., & Pöschl, U. (2010). Biomass burning aerosol emissions from vegetation: particle number and mass emission factors and size distributions. Atmos. Chem. Phys., 13.
- Jiménez, P. A., Dudhia, J., González-Rouco, J. F., Navarro, J., Montávez, J. P., & García-

- Bustamante, E. (2011). A Revised Scheme for the WRF Surface Layer Formulation. Monthly Weather Review, 140(3), 898–918. doi: 10.1175/MWR-D-11-00056.1
- Jiménez, P. A., Dudhia, J., González-Rouco, J. F., Navarro, J., Montávez, J. P., & García-Bustamante, E. (2012, March). A Revised Scheme for the WRF Surface Layer Formulation. Monthly Weather Review, 140(3), 898–918. (Publisher: American Meteorological Society) doi: 10.1175/MWR-D-11-00056.1
- Jiménez, P. A., Muñoz Esparza, D., & Kosović, B. (2018). A High Resolution Coupled Fire–Atmosphere Forecasting System to Minimize the Impacts of Wildland Fires: Applications to the Chimney Tops II Wildland Event. Atmosphere, 9(5), 197. doi: 10.3390/atmos9050197
- Jiménez, P. A., Navarro, J., Palomares, A. M., & Dudhia, J. (2015, March). Mesoscale modeling of offshore wind turbine wakes at the wind farm resolving scale: a composite-based analysis with the Weather Research and Forecasting model over Horns Rev: Mesoscale modeling at the wind farm resolving scale. Wind Energy, 18(3), 559–566. doi: 10.1002/we.1708
- Jost, H.-J., Drdla, K., Stohl, A., Pfister, L., Loewenstein, M., Lopez, J. P., ... Xueref, I. (2004). In-situ observations of mid-latitude forest fire plumes deep in the stratosphere. Geophysical Research Letters, 31(11). doi: 10.1029/2003GL019253
- Kablick, G. P., Allen, D. R., Fromm, M. D., & Nedoluha, G. E. (2020). Australian PyroCb Smoke Generates Synoptic-Scale Stratospheric Anticyclones. Geophysical Research Letters, 47(13), e2020GL088101. Retrieved 2020-07-07, from <https://agupubs.onlinelibrary.wiley.com/doi/abs/10.1029/2020GL088101> (\_eprint: <https://agupubs.onlinelibrary.wiley.com/doi/pdf/10.1029/2020GL088101>) doi: 10.1029/2020GL088101
- Kahn, R. A., Chen, Y., Nelson, D. L., Leung, F.-Y., Li, Q., Diner, D. J., & Logan, J. A. (2008, February). Wildfire smoke injection heights: Two perspectives from space. Geophysical Research Letters, 35(4). (Publisher: John Wiley & Sons, Ltd) doi: 10.1029/2007GL032165
- Kasischke, E. S., & Turetsky, M. R. (2006). Correction to Recent changes in the fire regime across the North American boreal region-Spatial and temporal patterns of burning across Canada and Alaska. Geophysical Research Letters, 33(13). doi: 10.1029/2006GL026946
- Keeley, S. (2013, December). Climate reanalysis [Text].
- Klemp, J. B., Dudhia, J., & Hassiotis, A. D. (2008, October). An Upper Gravity-Wave Absorbing Layer for NWP Applications. Monthly Weather Review, 136(10), 3987–4004. doi: 10.1175/2008MWR2596.1
- Knievel, J. C., Bryan, G. H., & Hacker, J. P. (2007, November). Explicit Numerical Diffusion in the WRF Model. Monthly Weather Review, 135(11), 3808–3824. (Publisher: American Meteorological Society) doi: 10.1175/2007MWR2100.1
- Koo, E., Pagni, P. J., Weise, D. R., & Woycheese, J. P. (2010, November). Firebrands and spotting ignition in large-scale fires. International Journal of Wildland Fire, 19(7), 818–843. (Publisher: CSIRO PUBLISHING) doi: 10.1071/WF07119
- Kristensen, H. M. (2019). Chapter 1 - Global Nuclear Arsenals, 1990–2018. In J. E. Doyle (Ed.),

- Nuclear Safeguards, Security, and Nonproliferation (Second Edition) (pp. 3–35). Boston: Butterworth-Heinemann. doi: 10.1016/B978-0-12-803271-8.00001-1
- Lareau, N. P., & Clements, C. B. (2016, March). Environmental controls on pyrocumulus and pyrocumulonimbus initiation and development. *Atmospheric Chemistry and Physics*, *16*(6), 4005–4022. doi: 10.5194/acp-16-4005-2016
- Lee, J. C. Y., & Lundquist, J. K. (2017a). Evaluation of the wind farm parameterization in the Weather Research and Forecasting model with meteorological and turbine power data. , 31.
- Lee, J. C. Y., & Lundquist, J. K. (2017b, September). Observing and Simulating Wind-Turbine Wakes During the Evening Transition. *Boundary-Layer Meteorology*, *164*(3), 449–474. doi: 10.1007/s10546-017-0257-y
- Lilly, D. K. (1966). On the application of the eddy viscosity concept in the inertial sub-range of turbulence. *NCAR manuscript*, *123*.
- Lindsey, D. T., & Fromm, M. (2008). Evidence of the cloud lifetime effect from wildfire-induced thunderstorms. *Geophysical Research Letters*, *35*(22). doi: 10.1029/2008GL035680
- Lindsey, R., & Dahlman, L. (n.d.). *Climate Change: Global Temperature | NOAA Climate.gov*. Retrieved 2020-09-28, from <https://www.climate.gov/news-features/understanding-climate/climate-change-global-temperature>
- Livesey, N. J., Fromm, M. D., Waters, J. W., Manney, G. L., Santee, M. L., & Read, W. G. (2004). Enhancements in lower stratospheric CH<sub>3</sub>CN observed by the Upper Atmosphere Research Satellite Microwave Limb Sounder following boreal forest fires. *Journal of Geophysical Research: Atmospheres*, *109*(D6). doi: 10.1029/2003JD004055
- Luderer, G., Trentmann, J., & Andreae, M. O. (2009, September). A new look at the role of fire-released moisture on the dynamics of atmospheric pyro-convection. *International Journal of Wildland Fire*, *18*(5), 554–562. (Publisher: CSIRO PUBLISHING) doi: 10.1071/WF07035
- Luderer, G., Trentmann, J., Winterrath, T., Textor, C., Herzog, M., Graf, H. F., & Andreae, M. O. (2006, July). Modeling of biomass smoke injection into the lower stratosphere by a large forest fire (Part II): Sensitivity studies. *Atmospheric Chemistry and Physics Discussions*, *6*(4), 6081–6124. (Publisher: European Geosciences Union)
- Mandel, J., Beezley, J. D., & Kochanski, A. K. (2011a). Coupled atmosphere-wildland fire modeling with WRF-Fire. *Geoscientific Model Development*, *4*(3), 591–610. (arXiv: 1102.1343) doi: 10.5194/gmd-4-591-2011
- Mandel, J., Beezley, J. D., & Kochanski, A. K. (2011b, July). Coupled atmosphere-wildland fire modeling with WRF-Fire. *Geoscientific Model Development*, *4*(3), 591–610. (arXiv: 1102.1343) doi: 10.5194/gmd-4-591-2011
- Mann, M. E., Rahmstorf, S., Kornhuber, K., Steinman, B. A., Miller, S. K., & Coumou, D. (2017, March). Influence of Anthropogenic Climate Change on Planetary Wave Resonance and Extreme Weather Events. *Scientific Reports*, *7*(1), 45242. (Number: 1 Publisher: Nature Publishing Group) doi: 10.1038/srep45242

- Mazzaro, L. J., Koo, E., Muñoz Esparza, D., Lundquist, J. K., & Linn, R. R. (2019). Random Force Perturbations: A New Extension of the Cell Perturbation Method for Turbulence Generation in Multiscale Atmospheric Boundary Layer Simulations. Journal of Advances in Modeling Earth Systems, 11(7), 2311–2329. doi: 10.1029/2019MS001608
- Mazzaro, L. J., Muñoz Esparza, D., Lundquist, J. K., & Linn, R. R. (2017, August). Nested mesoscale-to-LES modeling of the atmospheric boundary layer in the presence of under-resolved convective structures. Journal of Advances in Modeling Earth Systems, 9(4), 1795–1810. Retrieved 2018-10-04, from <https://agupubs.onlinelibrary.wiley.com/doi/abs/10.1002/2017MS000912> doi: 10.1002/2017MS000912
- Melillo, J. M., Richmond, T. T., & Yohe, G. W. (2014). Climate change impacts in the united states: The third national climate assessment. Retrieved 2020-09-28, from <https://data.globalchange.gov/report/nca3> doi: 10.7930/J0Z31WJ2
- Mellor, G. L., & Yamada, T. (1982). Development of a turbulence closure model for geophysical fluid problems. Reviews of Geophysics, 20(4), 851. doi: 10.1029/RG020i004p00851
- Mills, M. J., Toon, O. B., Lee-Taylor, J., & Robock, A. (2014). Multidecadal global cooling and unprecedented ozone loss following a regional nuclear conflict. Earth's Future, 2(4), 161–176. Retrieved 2019-01-08, from <https://agupubs.onlinelibrary.wiley.com/doi/abs/10.1002/2013EF000205> doi: 10.1002/2013EF000205
- Mills, M. J., Toon, O. B., Turco, R. P., Kinnison, D. E., & Garcia, R. R. (2008). Massive global ozone loss predicted following regional nuclear conflict. Proceedings of the National Academy of Sciences, 105(14), 5307–5312. doi: 10.1073/pnas.0710058105
- Moisseeva, N., & Stull, R. (2019, October). Capturing Plume Rise and Dispersion with a Coupled Large-Eddy Simulation: Case Study of a Prescribed Burn. Atmosphere, 10(10). doi: 10.3390/atmos10100579
- Moncrieff, M. W., & Miller, M. J. (1976). The dynamics and simulation of tropical cumulonimbus and squall lines. Quarterly Journal of the Royal Meteorological Society, 102(432), 373–394. (eprint: <https://rmets.onlinelibrary.wiley.com/doi/pdf/10.1002/qj.49710243208>) doi: 10.1002/qj.49710243208
- Morton, B. R. (1964). Fire and wind. Science Progress (1933- ), 52(206), 249–258.
- Muñoz Esparza, D., & Kosović, B. (2018, June). Generation of Inflow Turbulence in Large-Eddy Simulations of Nonneutral Atmospheric Boundary Layers with the Cell Perturbation Method. Monthly Weather Review, 146(6), 1889–1909. doi: 10.1175/MWR-D-18-0077.1
- Muñoz Esparza, D., Kosović, B., García-Sánchez, C., & van Beeck, J. (2014, June). Nesting Turbulence in an Offshore Convective Boundary Layer Using Large-Eddy Simulations. Boundary-Layer Meteorology, 151(3), 453–478. doi: 10.1007/s10546-014-9911-9
- Muñoz Esparza, D., Kosović, B., Jiménez, P. A., & Coen, J. L. (2018). An Accurate Fire-Spread Algorithm in the Weather Research and Forecasting Model Using the Level-Set Method. Journal of Advances in Modeling Earth Systems, 10(4), 908–926. doi: 10.1002/2017MS001108
- Muñoz Esparza, D., Kosović, B., Jiménez, P. A., & Coen, J. L. (2018). An Accurate Fire-Spread Al-

- gorithm in the Weather Research and Forecasting Model Using the Level-Set Method. Journal of Advances in Modeling Earth Systems, 10(4), 908–926. doi: 10.1002/2017MS001108
- Muñoz Esparza, D., Kosović, B., Mirocha, J., & van Beeck, J. (2014, December). Bridging the Transition from Mesoscale to Microscale Turbulence in Numerical Weather Prediction Models. Boundary-Layer Meteorology, 153(3), 409–440. doi: 10.1007/s10546-014-9956-9
- Muñoz Esparza, D., Kosović, B., van Beeck, J., & Mirocha, J. (2015, March). A stochastic perturbation method to generate inflow turbulence in large-eddy simulation models: Application to neutrally stratified atmospheric boundary layers. Physics of Fluids, 27(3), 035102. (Publisher: American Institute of Physics) doi: 10.1063/1.4913572
- Nakanishi, M., & Niino, H. (2009a). Development of an Improved Turbulence Closure Model for the Atmospheric Boundary Layer. Journal of the Meteorological Society of Japan, 87(5), 895–912. doi: 10.2151/jmsj.87.895
- Nakanishi, M., & Niino, H. (2009b). Development of an Improved Turbulence Closure Model for the Atmospheric Boundary Layer. Journal of the Meteorological Society of Japan, 87(5), 895–912. doi: 10.2151/jmsj.87.895
- Nauslar, N., Kaplan, M., Wallmann, J., & Brown, T. (2013, November). A forecast procedure for dry thunderstorms. Journal of Operational Meteorology, 1(17), 200–214. doi: 10.15191/nwajom.2013.0117
- Olson, J. B., Kenyon, J. S., Djalalova, I., Bianco, L., Turner, D. D., Pichugina, Y., ... Cline, J. (2019, November). Improving Wind Energy Forecasting through Numerical Weather Prediction Model Development. Bulletin of the American Meteorological Society, 100(11), 2201–2220. Retrieved 2020-09-27, from <https://journals.ametsoc.org/bams/article/100/11/2201/343771/Improving-Wind-Energy-Forecasting-through> (Publisher: American Meteorological Society) doi: 10.1175/BAMS-D-18-0040.1
- Osher, S., & Sethian, J. A. (1988). Fronts propagating with curvature-dependent speed: Algorithms based on Hamilton-Jacobi formulations. Journal of Computational Physics, 79(1), 12 – 49. doi: [https://doi.org/10.1016/0021-9991\(88\)90002-2](https://doi.org/10.1016/0021-9991(88)90002-2)
- Pachauri, R. K., Mayer, L. and Intergovernmental Panel on Climate Change (Ed.). (2015). Climate change 2014: synthesis report. Geneva, Switzerland: Intergovernmental Panel on Climate Change. (OCLC: 914851124)
- Pahlow, M., Kleissl, J., & Parlange, M. B. (2005, January). Atmospheric boundary-layer structure observed during a haze event due to forest-fire smoke. Boundary-Layer Meteorology, 114(1), 53–70. doi: 10.1007/s10546-004-6350-z
- Patton, E. G., & Coen, J. L. (2004a). WRF-Fire: A Coupled Atmosphere-Fire Module for WRF. , 3.
- Patton, E. G., & Coen, J. L. (2004b). Wrf-fire: A coupled atmosphere-fire module for wrf. , 22–25.
- Pearce, J. M., & Denkenberger, D. C. (2018). A National Pragmatic Safety Limit for Nuclear Weapon Quantities. Safety, 4(2), 25. doi: 10.3390/safety4020025

- Penner, J. E., Haselman, L. C., & Edwards, L. L. (1986). Smoke-Plume Distributions above Large-Scale Fires: Implications for Simulations of Nuclear Winter. Journal of Climate and Applied Meteorology, 25(10), 1434–1444. doi: 10.1175/1520-0450(1986)025<1434:SPDALS>2.0.CO;2
- Peterson, D. A., Campbell, J. R., Hyer, E. J., Fromm, M. D., Kablick, G. P., Cossuth, J. H., & DeLand, M. T. (2018a). Wildfire-driven thunderstorms cause a volcano-like stratospheric injection of smoke. npj Climate and Atmospheric Science, 1(1). doi: 10.1038/s41612-018-0039-3
- Peterson, D. A., Campbell, J. R., Hyer, E. J., Fromm, M. D., Kablick, G. P., Cossuth, J. H., & DeLand, M. T. (2018b, August). Wildfire-driven thunderstorms cause a volcano-like stratospheric injection of smoke. npj Climate and Atmospheric Science, 1(1), 1–8. Retrieved 2020-01-29, from <https://www.nature.com/articles/s41612-018-0039-3> doi: 10.1038/s41612-018-0039-3
- Peterson, D. A., Fromm, M. D., Solbrig, J. E., Hyer, E. J., Surratt, M. L., & Campbell, J. R. (2016, November). Detection and Inventory of Intense Pyroconvection in Western North America using GOES-15 Daytime Infrared Data. Journal of Applied Meteorology and Climatology, 56(2), 471–493. (Publisher: American Meteorological Society) doi: 10.1175/JAMC-D-16-0226.1
- Peterson, D. A., Hyer, E. J., Campbell, J. R., Fromm, M. D., Hair, J. W., Butler, C. F., & Fenn, M. A. (2014, November). The 2013 Rim Fire: Implications for Predicting Extreme Fire Spread, Pyroconvection, and Smoke Emissions. Bulletin of the American Meteorological Society, 96(2), 229–247. Retrieved 2020-06-03, from <https://journals.ametsoc.org/doi/full/10.1175/BAMS-D-14-00060.1> (Publisher: American Meteorological Society) doi: 10.1175/BAMS-D-14-00060.1
- Peterson, D. A., Hyer, E. J., Campbell, J. R., Solbrig, J. E., & Fromm, M. D. (2016). A Conceptual Model for Development of Intense Pyrocumulonimbus in Western North America. Monthly Weather Review, 145(6), 2235–2255. doi: 10.1175/MWR-D-16-0232.1
- Peterson, D. A., Hyer, E. J., & Wang, J. (2014). Quantifying the potential for high-altitude smoke injection in the North American boreal forest using the standard MODIS fire products and subpixel-based methods. Journal of Geophysical Research: Atmospheres, 119(6), 3401–3419. doi: 10.1002/2013JD021067
- Pifer, S. (2016). The Future of U.S.-Russian Arms Control. The Brookings Institution, 6.
- Porter, J., et al. (2014). Food Security and Food Production Systems. Climate Change 2014: Impacts, Adaptation, and Vulnerability. Part A: Global and Sectoral Aspects. Contribution of Working Group II to the Fifth Assessment Report of the Intergovernmental Panel on Climate Change, 49.
- Pörtner, H., et al. (2019). Summary for policymakers.
- Potter, B. E. (2005, April). The role of released moisture in the atmospheric dynamics associated with wildland fires. International Journal of Wildland Fire, 14(1), 77–84. (Publisher: CSIRO PUBLISHING) doi: 10.1071/WF04045

- Poulida, O., Dickerson, R. R., & Heymsfield, A. (1996). Stratosphere-troposphere exchange in a midlatitude mesoscale convective complex: 1. Observations. Journal of Geophysical Research: Atmospheres, 101(D3). doi: 10.1029/95JD03523
- Powers, J. G., Klemp, J. B., Skamarock, W. C., Davis, C. A., Dudhia, J., Gill, D. O., ... Duda, M. G. (2017). The Weather Research and Forecasting Model: Overview, System Efforts, and Future Directions. Bulletin of the American Meteorological Society, 98(8), 1717–1737. doi: 10.1175/BAMS-D-15-00308.1
- Rajewski, D. A., Takle, E. S., Lundquist, J. K., Oncley, S., Prueger, J. H., Horst, T. W., ... Doorenbos, R. K. (2013, May). Crop Wind Energy Experiment (CWEX): Observations of Surface-Layer, Boundary Layer, and Mesoscale Interactions with a Wind Farm. Bulletin of the American Meteorological Society, 94(5), 655–672. doi: 10.1175/BAMS-D-11-00240.1
- Rajewski, D. A., Takle, E. S., Prueger, J. H., & Doorenbos, R. K. (2016, November). Toward understanding the physical link between turbines and microclimate impacts from in situ measurements in a large wind farm: MICROCLIMATE WITH TURBINES ON VERSUS OFF. Journal of Geophysical Research: Atmospheres, 121(22), 13,392–13,414. doi: 10.1002/2016JD025297
- Rasmussen, R. M., Geresdi, I., Thompson, G., Manning, K., & Karplus, E. (2002, February). Freezing Drizzle Formation in Stably Stratified Layer Clouds: The Role of Radiative Cooling of Cloud Droplets, Cloud Condensation Nuclei, and Ice Initiation. Journal of the Atmospheric Sciences, 59(4), 837–860. (Publisher: American Meteorological Society) doi: 10.1175/1520-0469(2002)059<0837:FDFISS>2.0.CO;2
- Redfern, S., Olson, J. B., Lundquist, J. K., & Clack, C. T. M. (2019, March). Incorporation of the Rotor-Equivalent Wind Speed into the Weather Research and Forecasting Model's Wind Farm Parameterization. Monthly Weather Review, 147(3), 1029–1046. Retrieved 2020-09-28, from <https://journals.ametsoc.org/mwr/article/147/3/1029/107084/Incorporation-of-the-Rotor-Equivalent-Wind-Speed> (Publisher: American Meteorological Society) doi: 10.1175/MWR-D-18-0194.1
- Reisner, J., D'Angelo, G., Koo, E., Even, W., Hecht, M., Hunke, E., ... Cooley, J. (2018). Climate Impact of a Regional Nuclear Weapons Exchange: An Improved Assessment Based On Detailed Source Calculations. Journal of Geophysical Research: Atmospheres, 123(5), 2752–2772. doi: 10.1002/2017JD027331
- Reisner, J., Rasmussen, R. M., & Bruintjes, R. T. (1998). Explicit forecasting of supercooled liquid water in winter storms using the MM5 mesoscale model. Quarterly Journal of the Royal Meteorological Society, 124(548). doi: 10.1002/qj.49712454804
- Reutter, P., Trentmann, J., Seifert, A., Neis, P., Su, H., Chang, D., ... Pöschl, U. (2014, July). 3-D model simulations of dynamical and microphysical interactions in pyroconvective clouds under idealized conditions. Atmospheric Chemistry and Physics, 14(14), 7573–7583. doi: 10.5194/acp-14-7573-2014
- Robock, A., Oman, L., & Stenchikov, G. L. (2007). Nuclear winter revisited with a modern climate model and current nuclear arsenals: Still catastrophic consequences. Journal of Geophysical Research: Atmospheres, 112(D13). Retrieved 2019-08-21, from <https://>

agupubs.onlinelibrary.wiley.com/doi/abs/10.1029/2006JD008235 doi: 10.1029/2006JD008235

- Robock, A., Oman, L., Stenchikov, G. L., Toon, O. B., Bardeen, C., & Turco, R. P. (2007). Climatic consequences of regional nuclear conflicts. *Atmos. Chem. Phys.*, 65.
- Robock, A., & Toon, O. B. (2012a). Self-assured destruction: The climate impacts of nuclear war. *Bulletin of the Atomic Scientists*, 68(5), 66–74. doi: 10.1177/0096340212459127
- Robock, A., & Toon, O. B. (2012b, March). Self-assured destruction: The climate impacts of nuclear war. *Bulletin of the Atomic Scientists*, 68(5), 66–74. Retrieved 2019-01-08, from <http://www.tandfonline.com/doi/full/10.1177/0096340212459127> doi: 10.1177/0096340212459127
- Robock, A., Toon, O. B., & Bardeen, C. G. (2019). Comment on Climate Impact of a Regional Nuclear Weapon Exchange: An Improved Assessment Based on Detailed Source Calculations by Reisner et al. *Journal of Geophysical Research: Atmospheres*, 124(23), 12953–12958. doi: 10.1029/2019JD030777
- Robock, A., Toon, O. B., Bardeen, C. G., Xia, L., Kristensen, H. M., McKinzie, M., ... Turco, R. P. (2019, November). How an India-Pakistan nuclear war could start and have global consequences. *Bulletin of the Atomic Scientists*, 75(6), 273–279. Retrieved 2020-02-06, from <https://doi.org/10.1080/00963402.2019.1680049> doi: 10.1080/00963402.2019.1680049
- Rodden, R. M., John, F. I., & Laurino, R. (1965). *Exploratory Analysis of Fire Storms* (Tech. Rep.). STANFORD RESEARCH INST MENLO PARK CA.
- Rosenfeld, D., Fromm, M., Trentmann, J., Luderer, G., Andreae, M. O., & Servranckx, R. (2007, February). The Chisholm firestorm: observed microstructure, precipitation and lightning activity of a pyro-cumulonimbus. *Atmospheric Chemistry and Physics*, 7(3), 645–659. (Publisher: European Geosciences Union)
- Rothermel, R. C. (1972). *A mathematical model for predicting fire spread in wildland fuels*. (Tech. Rep.). USDA Forest Service. Retrieved from [https://www.fs.fed.us/rm/pubs\\_int/int\\_rp115.pdf](https://www.fs.fed.us/rm/pubs_int/int_rp115.pdf)
- Ryan, K. C., & Opperman, T. S. (2013). Landfire—a national vegetation/fuels data base for use in fuels treatment, restoration, and suppression planning. *Forest Ecology and Management*, 294, 208–216.
- Sagan, C. (1983). Nuclear War and Climatic Catastrophe: Some Policy Implications. *Foreign Affairs*, 62(2), 257–292. Retrieved from <https://www.jstor.org/stable/20041818> doi: 10.2307/20041818
- Schmitz, S. (2011). Wind Turbine Aerodynamics. , 49.
- Services, A. D. (2017). *U.s. wind industry fourth quarter 2017 market report*. Retrieved from [https://www.faa.gov/data\\_research/aviation/aerospace\\_forecasts/media/FY2017-37\\_FAA\\_Aerospace\\_Forecast.pdf](https://www.faa.gov/data_research/aviation/aerospace_forecasts/media/FY2017-37_FAA_Aerospace_Forecast.pdf) doi: 10.1002/ejoc.201200111.
- Services, A. D. (2020). *U.s. wind industry second quarter 2020 market report*. Re-



- trieved from [https://www.awea.org/Awea/media/Resources/Publications%20and%20Reports/Market%20Reports/2Q-2020-WPA-Report\\_Public-Version.pdf](https://www.awea.org/Awea/media/Resources/Publications%20and%20Reports/Market%20Reports/2Q-2020-WPA-Report_Public-Version.pdf) doi: 10.1002/ejoc.201200111.
- Shaw, W. J., Berg, L. K., Cline, J., Draxl, C., Djalalova, I., Grimit, E. P., ... Wilczak, J. M. (2019, September). The Second Wind Forecast Improvement Project (WFIP2): General Overview. Bulletin of the American Meteorological Society, 100(9), 1687–1699. (Publisher: American Meteorological Society) doi: 10.1175/BAMS-D-18-0036.1
- SIPRI. (2019). World nuclear forces. Retrieved from <https://sipri.org/yearbook/2019/06/>
- Skamarock, C., Klemp, B., Dudhia, J., Gill, O., Liu, Z., Berner, J., ... Huang, X.-y. (2019). A Description of the Advanced Research WRF Model Version 4. doi: 10.5065/1dfh-6p97
- Skamarock, W. C., & Klemp, J. B. (2008, March). A time-split nonhydrostatic atmospheric model for weather research and forecasting applications. Journal of Computational Physics, 227(7), 3465–3485. doi: 10.1016/j.jcp.2007.01.037
- Skamarock, W. C., Klemp, J. B., Dudhia, J., Gill, D. O., Barker, D. M., Duda, M. G., ... Powers, J. G. (2008). A Description of the Advanced Research WRF Version 3. , 125.
- S. Lissaman, P. B. (1979, November). Energy Effectiveness of Arbitrary Arrays of Wind Turbines. Journal of Energy, 3(6), 323–328. doi: 10.2514/3.62441
- Small, R. D., & Heikes, K. E. (1988, May). Early Cloud Formation by Large Area Fires. Journal of Applied Meteorology, 27(5), 654–663. doi: 10.1175/1520-0450(1988)027<0654:ECFBLA>2.0.CO;2
- Smith, C. M., Barthelmie, R. J., & Pryor, S. C. (2013, September). *In situ* observations of the influence of a large onshore wind farm on near-surface temperature, turbulence intensity and wind speed profiles. Environmental Research Letters, 8(3), 034006. doi: 10.1088/1748-9326/8/3/034006
- Smith, K., et al. (2014). Human Health: Impacts, Adaptation, and Co-Benefits. Climate Change 2014: Impacts, Adaptation, and Vulnerability. Part A: Global and Sectoral Aspects. Contribution of Working Group II to the Fifth Assessment Report of the Intergovernmental Panel on Climate Change, 46.
- Stenchikov, G., Dickerson, R., Pickering, K., Ellis, W., Doddridge, B., Kondragunta, S., ... Tao, W.-K. (1996). Stratosphere-troposphere exchange in a midlatitude mesoscale convective complex: 2. Numerical simulations. Journal of Geophysical Research: Atmospheres, 101(D3). doi: 10.1029/95JD02468
- Stocks, B. J., Fosberg, M. A., Lynham, T. J., Mearns, L., Wotton, B. M., Yang, Q., ... McKENNEY, D. W. (1998, January). Climate Change and Forest Fire Potential in Russian and Canadian Boreal Forests. Climatic Change, 38(1), 1–13. doi: 10.1023/A:1005306001055
- Stott, P. (2016, June). How climate change affects extreme weather events. Science, 352(6293), 1517–1518. doi: 10.1126/science.aaf7271

- Tarifa, C. S., Notario, P. P. d., & Moreno, F. G. (1965, January). On the flight paths and lifetimes of burning particles of wood. Symposium (International) on Combustion, 10(1), 1021–1037. doi: 10.1016/S0082-0784(65)80244-2
- Tewari, M., Chen, F., Wang, W., Dudhia, J., LeMone, M., Mitchell, K., ... others (2004). Implementation and verification of the unified noah land surface model in the wrf model. In 20th conference on weather analysis and forecasting/16th conference on numerical weather prediction (Vol. 1115).
- Thompson, G., & Eidhammer, T. (2014, October). A Study of Aerosol Impacts on Clouds and Precipitation Development in a Large Winter Cyclone. Journal of the Atmospheric Sciences, 71(10), 3636–3658. doi: 10.1175/JAS-D-13-0305.1
- Thompson, G., Field, P. R., Rasmussen, R. M., & Hall, W. D. (2008). Explicit Forecasts of Winter Precipitation Using an Improved Bulk Microphysics Scheme. Part II: Implementation of a New Snow Parameterization. Monthly Weather Review, 136(12), 5095–5115. doi: 10.1175/2008MWR2387.1
- Thompson, G., Rasmussen, R. M., & Manning, K. (2004a). Explicit Forecasts of Winter Precipitation Using an Improved Bulk Microphysics Scheme. Part I: Description and Sensitivity Analysis. Monthly Weather Review, 132(2), 519–542. doi: 10.1175/1520-0493(2004)132<0519:EFOWPU>2.0.CO;2
- Thompson, G., Rasmussen, R. M., & Manning, K. (2004b, February). Explicit Forecasts of Winter Precipitation Using an Improved Bulk Microphysics Scheme. Part I: Description and Sensitivity Analysis. Monthly Weather Review, 132(2), 519–542. (Publisher: American Meteorological Society) doi: 10.1175/1520-0493(2004)132<0519:EFOWPU>2.0.CO;2
- Thornton, W. (1917). Xv. the relation of oxygen to the heat of combustion of organic compounds. The London, Edinburgh, and Dublin Philosophical Magazine and Journal of Science, 33(194), 196–203.
- Toon, O. B., Bardeen, C. G., Robock, A., Xia, L., Kristensen, H., McKinzie, M., ... Turco, R. P. (2019). Rapidly expanding nuclear arsenals in Pakistan and India portend regional and global catastrophe. Science Advances, 5(10), eaay5478. doi: 10.1126/sciadv.aay5478
- Toon, O. B., Robock, A., & Turco, R. P. (2008, December). Environmental consequences of nuclear war. Physics Today, 61(12), 37–42. doi: 10.1063/1.3047679
- Toon, O. B., Robock, A., Turco, R. P., Bardeen, C., Oman, L., & Stenchikov, G. L. (2007). Consequences of Regional-Scale Nuclear Conflicts. Science, 315(5816), 1224–1225. doi: 10.1126/science.1137747
- Tory, K., & Thurston, W. (2015). Pyrocumulonimbus: A literature review. Bushfire and Natural Hazards CRC: East Melbourne, VIC, Australia.
- Tory, K. J., Thurston, W., & Kepert, J. D. (2018, June). Thermodynamics of Pyrocumulus: A Conceptual Study. Monthly Weather Review, 146(8), 2579–2598. (Publisher: American Meteorological Society) doi: 10.1175/MWR-D-17-0377.1
- Trentmann, J., Luderer, G., Winterrath, T., Fromm, M. D., Servranckx, R., Textor, C., ... An-

- dreae, M. O. (2006, July). Modeling of biomass smoke injection into the lower stratosphere by a large forest fire (Part I): reference simulation. Atmospheric Chemistry and Physics Discussions, 6(4), 6041–6080. (Publisher: European Geosciences Union)
- Turco, R. P., Toon, O. B., Ackerman, T. P., Pollack, J. B., & Sagan, C. (1983a). Nuclear Winter: Global Consequences of Multiple Nuclear Explosions. Science, 222(4630), 1283–1292. doi: 10.1126/science.222.4630.1283
- Turco, R. P., Toon, O. B., Ackerman, T. P., Pollack, J. B., & Sagan, C. (1983b, December). Nuclear Winter: Global Consequences of Multiple Nuclear Explosions. Science, 222(4630), 1283–1292. Retrieved 2019-01-07, from <http://science.sciencemag.org/content/222/4630/1283> doi: 10.1126/science.222.4630.1283
- Turco, R. P., Toon, O. B., Ackerman, T. P., Pollack, J. B., & Sagan, C. (1990). Climate and smoke: An appraisal of nuclear winter. Science, 247(4939), 166–176.
- Vanderwende, B. J., Kosović, B., Lundquist, J. K., & Mirocha, J. D. (2016). Simulating effects of a wind-turbine array using LES and RANS: Simulating turbines using LES and RANS. Journal of Advances in Modeling Earth Systems, 8(3), 1376–1390. doi: 10.1002/2016MS000652
- Vasiljević, N., L. M. Palma, J. M., Angelou, N., Carlos Matos, J., Menke, R., Lea, G., ... M. G. C. Gomes, V. M. (2017, September). Perdigo 2015: methodology for atmospheric multi-Doppler lidar experiments. Atmospheric Measurement Techniques, 10(9), 3463–3483. Retrieved 2020-09-28, from <https://amt.copernicus.org/articles/10/3463/2017/> (Publisher: Copernicus GmbH) doi: <https://doi.org/10.5194/amt-10-3463-2017>
- Vautard, R., Thais, F., Tobin, I., Bréon, F.-M., de Lavergne, J.-G. D., Colette, A., ... Ruti, P. M. (2014, December). Regional climate model simulations indicate limited climatic impacts by operational and planned European wind farms. Nature Communications, 5(1). doi: 10.1038/ncomms4196
- Veers, P., Dykes, K., Lantz, E., Barth, S., Bottasso, C. L., Carlson, O., ... Wiser, R. (2019, October). Grand challenges in the science of wind energy. Science, 366(6464). Retrieved 2020-09-27, from <https://science.sciencemag.org/content/366/6464/eaau2027> (Publisher: American Association for the Advancement of Science Section: Review) doi: 10.1126/science.aau2027
- Volker, P. J. H., Badger, J., Hahmann, A. N., & Ott, S. (2015, November). The Explicit Wake Parametrisation V1.0: a wind farm parametrisation in the mesoscale model WRF. Geoscientific Model Development, 8(11), 3715–3731. doi: 10.5194/gmd-8-3715-2015
- Wagner, R., Antoniou, I., Pedersen, S. M., Courtney, M. S., & Jørgensen, H. E. (2009, May). The influence of the wind speed profile on wind turbine performance measurements. Wind Energy, 12(4), 348–362. doi: 10.1002/we.297
- Wagner, R., Jahn, M., & Schepanski, K. (2018, August). Wildfires as a source of airborne mineral dust—revisiting a conceptual model using large-eddy simulation (LES). Atmospheric Chemistry and Physics, 18(16), 11863–11884. doi: 10.5194/acp-18-11863-2018
- Waibel, A. E., Fischer, H., Wienhold, F. G., Siegmund, P. C., Lee, B., Ström, J., ... Crutzen, P. J.

- (1999, August). Highly elevated carbon monoxide concentrations in the upper troposphere and lowermost stratosphere at northern midlatitudes during the STREAM II summer campaign in 1994. Chemosphere - Global Change Science, 1(1), 233–248. doi: 10.1016/S1465-9972(99)00027-6
- Wakimoto, R. M. (1985, July). Forecasting Dry Microburst Activity over the High Plains. Monthly Weather Review, 113(7), 1131–1143. (Publisher: American Meteorological Society)
- Wang, C., & Prinn, R. G. (2010). Potential climatic impacts and reliability of very large-scale wind farms. Atmos. Chem. Phys., 9.
- Wellerstein, A. (2012). Nukemap. Retrieved from <https://nuclearsecrecy.com/nukemap/>
- Whiteman, C. D., Zhong, S., Shaw, W. J., Hubbe, J. M., Bian, X., & Mittelstadt, J. (2001, August). Cold Pools in the Columbia Basin. Weather and Forecasting, 16(4), 432–447. doi: 10.1175/1520-0434(2001)016<0432:CPITCB>2.0.CO;2
- Wilcox, L. J., Hoskins, B. J., & Shine, K. P. (2012). A global blended tropopause based on ERA data. Part I: Climatology. Quarterly Journal of the Royal Meteorological Society, 138(664), 561–575. doi: 10.1002/qj.951
- Wilczak, J. M., Stoelinga, M., Berg, L. K., Sharp, J., Draxl, C., McCaffrey, K., ... White, A. B. (2019, September). The Second Wind Forecast Improvement Project (WFIP2): Observational Field Campaign. Bulletin of the American Meteorological Society, 100(9), 1701–1723. Retrieved 2020-06-16, from <https://journals.ametsoc.org/bams/article/100/9/1701/344833/The-Second-Wind-Forecast-Improvement-Project-WFIP2> (Publisher: American Meteorological Society) doi: 10.1175/BAMS-D-18-0035.1
- Williams, A. P., Abatzoglou, J. T., Gershunov, A., Guzman-Morales, J., Bishop, D. A., Balch, J. K., & Lettenmaier, D. P. (2019). Observed Impacts of Anthropogenic Climate Change on Wildfire in California. Earth's Future, 7(8), 892–910. Retrieved 2020-09-26, from <https://agupubs.onlinelibrary.wiley.com/doi/abs/10.1029/2019EF001210> (\_eprint: <https://agupubs.onlinelibrary.wiley.com/doi/pdf/10.1029/2019EF001210>) doi: 10.1029/2019EF001210
- Williams, E., Hittinger, E., Carvalho, R., & Williams, R. (2017, July). Wind power costs expected to decrease due to technological progress. Energy Policy, 106, 427–435. doi: 10.1016/j.enpol.2017.03.032
- Wiser, R., Hand, M., Seel, J., & Paulos, B. (2016). Reducing Wind Energy Costs through Increased Turbine Size: Is the Sky the Limit? , 7.
- World Wind Energy Association. (2020). World wind capacity at 650,8 GW, Corona crisis will slow down markets in 2020, renewables to be core of economic stimulus programmes. Retrieved 2020-09-28, from <https://wwindea.org/blog/2020/04/16/world-wind-capacity-at-650-gw/>
- Wyngaard, J. C. (2004, July). Toward Numerical Modeling in the Terra Incognita. Journal of the Atmospheric Sciences, 61(14), 1816–1826. Retrieved 2020-09-28, from <https://journals.ametsoc.org/jas/article/61/14/1816/25586/Toward>

~~-Numerical-Modeling-in-the-Terra-Incognita~~ (Publisher: American Meteorological Society) doi: 10.1175/1520-0469(2004)061<1816:TNMITT>2.0.CO;2

- Xia, G., Cervarich, M. C., Roy, S. B., Zhou, L., Minder, J. R., Jimenez, P. A., & Freedman, J. M. (2017, December). Simulating Impacts of Real-World Wind Farms on Land Surface Temperature Using the WRF Model: Validation with Observations. Monthly Weather Review, 145(12), 4813–4836. (Publisher: American Meteorological Society) doi: 10.1175/MWR-D-16-0401.1
- Xia, L., Robock, A., Mills, M., Stenke, A., & Helfand, I. (2015). Decadal reduction of chinese agriculture after a regional nuclear war. Earth's Future, 3(2), 37–48.
- Yu, P., Toon, O. B., Bardeen, C. G., Zhu, Y., Rosenlof, K. H., Portmann, R. W., ... Robock, A. (2019). Black carbon lofts wildfire smoke high into the stratosphere to form a persistent plume. Science, 365(6453), 587–590. doi: 10.1126/science.aax1748
- Zhou, L., Tian, Y., Baidya Roy, S., Thorncroft, C., Bosart, L. F., & Hu, Y. (2012, July). Impacts of wind farms on land surface temperature. Nature Climate Change, 2(7), 539–543. doi: 10.1038/nclimate1505
- Zou, C., Zhao, Q., Zhang, G., & Xiong, B. (2016, January). Energy revolution: From a fossil energy era to a new energy era. Natural Gas Industry B, 3(1), 1–11. Retrieved 2020-09-28, from <http://www.sciencedirect.com/science/article/pii/S2352854016300109> doi: 10.1016/j.ngib.2016.02.001

## Appendix A

### Supplementary Information for Chapter 2

A second set of simulations was run with TKE advection turned off, in order to evaluate the new WFP physics in a modeling environment consistent with that used in the National Oceanic and Atmospheric Administration (NOAA)’s operational Rapid Refresh forecast system (Benjamin et al. 2016). The lack of TKE advection had some significant impacts on the results.

#### A.1 Neutral Case

The TKE generation in the neutral stability simulation was stronger than with TKE advection turned off. The TKE increase within the wind farm reaches a maximum of  $0.4 \text{ m}^2 \text{ s}^{-2}$  — about 7 times greater than a simulation run without the WFP. It also remains constrained within the farm area, instead of being advected downwind. The TKE spreads directly upwards from the farm to the base of the inversion, slightly perturbing the boundary layer, as seen in the LES of Allaerts and Meyers (2017), as well as in F2012. The most prominent difference between these results and those of F2012 is the extension of TKE downwind peaking at around 200 m above ground and rapidly decaying in the horizontal at higher altitudes. This phenomenon may be directly attributed to this lack of TKE advection.

#### A.2 Stable, Linear Wind Shear Case

Although the magnitude of the impacts from the new WFP physics remains nominal for the linearly stable simulations, without TKE advection enabled some clear spatial patterns emerge—

primarily in the wake development and power production. As wind speeds increase across the rotor plane, the RWFP moves from weakening the wake to strengthening it (Figure A.1). The greatest instance of wake weakening occurs in the SR\_60 and the SB\_60 cases, with a maximum reduction as compared with the WFP wake of  $0.018 \text{ m s}^{-1}$ . With higher wind speeds, the RWFP wake begins to intensify within the farm and spread around its flanks downstream. This widening and fortification likely emerges due to the lateral entrainment of momentum via horizontal diffusion, which mixes higher wind speeds into the farm along its north and south edges. The SR\_10 case sees the greatest wake strengthening with a maximum increase of  $0.011 \text{ m s}^{-1}$ .

Power output varies only slightly between the RWFP and WFP schemes and these variations correspond with the differences in wakening (Figure A.2). Front-row turbines using the REWS see an increase in their power output and downstream turbines experience a decrease for all SR and SB cases. The largest difference in total wind farm average power output arises at smaller wind speeds. SB\_06 sees a 3.29%, or about 27.6 kW, reduction in average power compared with SF\_06. As wind speeds increase, this mean difference becomes positive. Compared with SB\_06, SB\_10 sees a 1.25% increase in total average power. The greatest increase in maximum power output for a single turbine occurs in SR\_10, with a 3.49% increase over SF\_10. The largest reduction in minimum power output for a single turbine is seen in SB\_06, with a 16.27% decrease.

### A.3 Stable, Nonlinear Wind Shear Case

Without TKE advection turned on, the cold pool mix-out simulations highlight two new impacts from the RWFP physics. First, the REWS and veer-awareness appear to interact in a non-linear fashion. When both options are enabled, their combined influence has a much greater impact on the wakes and power generated by the turbines than either option alone. Second, unlike with the TKE advection-enabled simulations, the REWS can be stronger than the hub height wind speed. For wind speeds near the cut-in value, the REWS-only turbines can turn on when they remain off for simulations using the other physics schemes (including REWS and veer-awareness together), as in MR\_80 (Figure A.3).

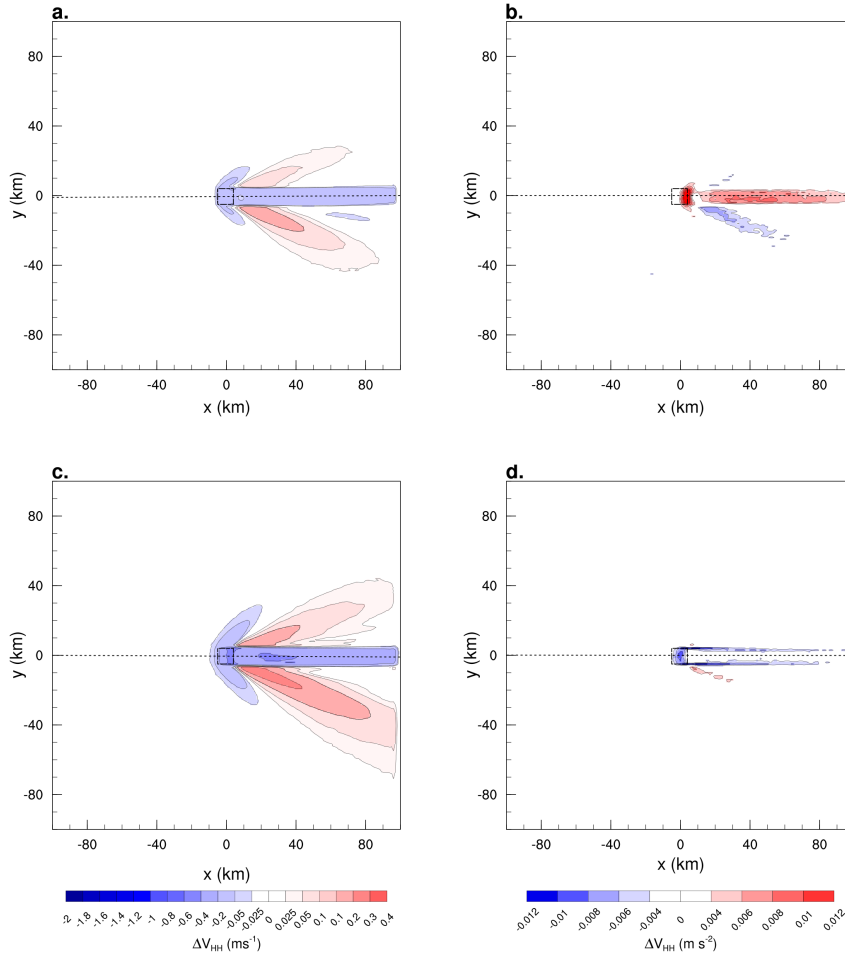


Figure A.1: Hub height wind (80 m) speed differences between the RWFP (REWS only) and the WFP in a stable environment. The plots on the left hand side depict the wakes seen with the WFP in SR\_06 (a) and SR\_10 (c). The right hand side plots show the differences in waking between the REWS RWFP and the WFP in SR\_06 (b) and SR\_10 (d).

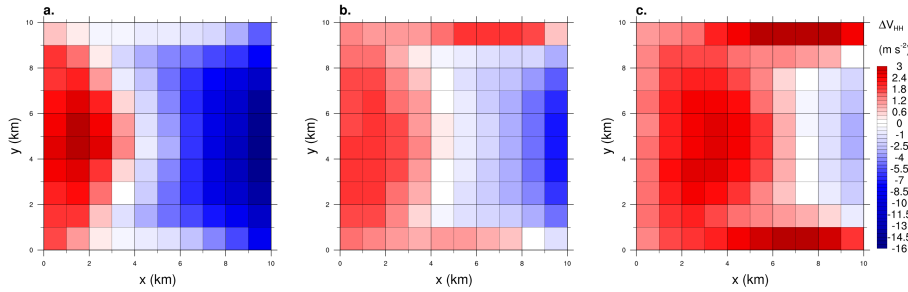


Figure A.2: Percentage differences in average power output between the WFP and the RWFP (REWS only) in a stable environment for SR\_06 (a), SR\_08 (b), and SR\_10 (c).



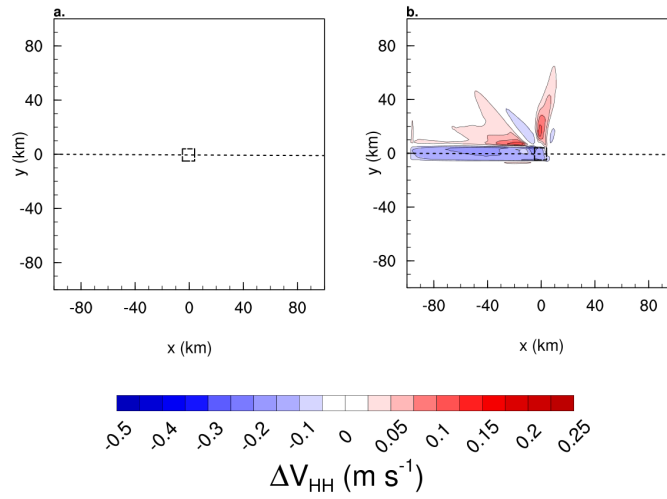


Figure A.3: The left plot (a) depicts the wakes that develop at hub height (80 m) when the WFP is activated for the cold pool mix-out simulation with the inversion level at 80 m (M\_80). The wind speed at hub height is below the cut-in speed for the turbines, so they do not produce power. The right plot (b) depicts the difference in wakening between the REWS and WFP simulations with the 80 m inversion level. The REWS enables the turbines to see a wind speed above the cut-in velocity, and the turbines produce power and generate wakes.